E-397

UR-679

INCLUSIVE CHARGED-PARTICLE PRODUCTION IN NEUTRON-NUCLEUS COLLISIONS AT HIGH ENERGY

by

David Hall Chaney

Submitted in Partial Fulfillment

of the

Requirements for the Degree

DOCTOR OF PHILOSOPHY

Department of Physics and Astronomy

The University of Rochester

Rochester, New York

1978

VITAE

The author was born in Columbus Ohio.

He attended the University of Rochester as an undergraduate, where in June of 1973 he received a Bachelor of Arts degree in Mathematics and a Bachelor of Science degree in Physics. Continuing at the University of Rochester, the author then undertook graduate study in the field of High Energy Physics, working as a Research Assistant and Teaching Assistant under his subsequent thesis advisor, Professor Thomas Ferbel. The author participated in the ongoing University of Rochester collaboration with Northwestern University and Fermilab, which performed a series of experiments at Fermilab in Batavia, Ill.

ACKNOWLEDGEMENTS

This thesis is based on an experiment which involved the efforts of a great many individuals. This is a consequence of the scope and scale of present-day high-energy physics experimentation.

First and foremost, I wish to thank Professor Thomas Ferbel for his leadership, advice, and counsel during my time at the University of Rochester. He has served as an unending source of enthusiasm as a teacher, thesis advisor, and collaborator. I also wish to thank Professor Paul Slattery, also a collaborator, for many helpful discussions along the way.

This work is the culmination of an experiment that was one in a long line of experiments carried out by a collaboration of scientists from the University of Rochester, Northwestern University, and Fermilab. I would like to acknowledge the contributions of my fellow collaborators on the experiment; Edward Bleser, Thomas Ferbel, Bruno Gobbi, David Johnson, Joseph Keren, Ronald Lipton, William Mollet, Jerome Rosen, Randal Ruchti, Paul Slattery, Daniel Spelbring, and David Underwood. Valuable assistance was also provided by David Berg, Terrence Jensen, Roger Lord, Thomas Phillips, and Brian Wormington. I would like to thank the staff of Fermilab, its director Robert Wilson, and Charles Brown, head of the Meson Laboratory during the

execution of this experiment, for providing resources and support for our experimental effort. The research was sponsored by the Department of Energy, and computing time was provided by the University of Rochester's Medical Center Computing Facility.

I was assisted in the preparation of this thesis by Lesia Gudzowaty who typed the manuscript, and by Albert Covert and Ray Soosaar who helped with the figures. I also wish to thank Boyce Grier and Vijay Murgai for assistance in proofreading the manuscript.

ABSTRACT

We have measured charged-particle production in neutron-nucleus collisions at high energy. Data on positive and negative particles produced in nuclei (ranging in atomic number (A) from beryllium to lead) are presented for essentially the full forward hemisphere of the center-of-mass system. A rough pion-proton separation is achieved for the positive spectra. Fits of the form A^{α} to the cross sections are presented as functions of transverse momentum, longitudinal momentum, rapidity, and pseudo-rapidity. It is found that α changes from $\sim$0.85 to $\sim$0.60 for laboratory rapidities ranging from 4 to 8. Differences in the data at large rapidity and large pseudo-rapidity are shown. The major features of our data can be understood in terms of current particle-production models.

TABLE OF CONTENTS

		Page
VITAE		ii
ACKNOWLEDGEMENTS		iii
ABSTRACT		v
LIST OF TABLES		viii
LIST OF FIGURES		ix
CHAPTER		
I	INTRODUCTION	1
II	THE EXPERIMENT	4
	A. The Beam	4
	B. The Target	9
	C. The Spectrometer	9
	1. The Scintillation Counters	12
	2. The Spark Chambers	13
	3. The Magnet	16
	4. The Trigger	16
	D. The Calorimeter	17
	E. Data Acquisition	18
III	DATA ANALYSIS	19
	A. Beam-line Monitoring and Neutron Counting	19
	1. Monitoring of the Beam	21
	2. Measurement of Neutron Flux	23

CHAPTER		Page
	B. Corrections to the Data	26
	1. Empty-Target Data	27
	2. Electrons	27
	a. The vertical aperture of the L-counter	28
	b. Signals in the L-counter	31
	c. Attenuation length in the L-counter	33
	d. Identification of electrons	37
	3. Protons	41
	C. Weighting of Events	45
	1. Geometric Losses	46
	2. Efficiency of the Spectrometer	50
	3. Experimental Sensitivity	55
	D. Conversion of Data to Cross Sections	58
IV	RESULTS	61
	A. Dependence on Transverse Momentum	62
	B. Dependence on Longitudinal Momentum and Rapidity	65
	C. Correlations Between y and p_T	68
	D. Comparison of Dependence on Rapidity and Pseudo-Rapidity	71
	E. Systematic Errors	76
	F. Conclusions	78
REFERENCES		99
APPENDIX		102

LIST OF TABLES

TABLE		Page
II.1	Properties of the nuclear targets.	10
III.1	Data Summary	20
III.2	Material in the beam-line, downstream of the target.	24
IV.1	Table of differential multiplicities and fitted atomic-weight dependence as functions of the square of the transverse momentum.	81
IV.2	Table of differential multiplicities and fitted atomic-weight dependence as functions of longitudinal momentum.	83
IV.3	Table of differential multiplicities and fitted atomic-weight dependence as functions of rapidity.	84
IV.4	Table of differential multiplicities and fitted atomic-weight dependence as functions of the square of the transverse momentum versus rapidity.	86
IV.5	Table of differential multiplicities and fitted atomic-weight dependence as functions of the square of the transverse momentum. versus longitudinal momentum.	90
IV.6	Table of differential multiplicities and fitted atomic-weight dependence as functions of pseudo-rapidity.	92
IV.7	Table of differential multiplicities and fitted atomic-weight dependence as functions of rapidity versus longitudinal momentum.	94
IV.8	Table of differential multiplicities and fitted atomic-weight dependence as functions of pseudo-rapidity versus longitudinal momentum.	96

LIST OF FIGURES

Figure		Page
II.1	Schematic of the M-3 beam-line.	5
II.2	Particle composition of the M-3 beam-line.	7
II.3	Momentum spectrum of the M-3 beam-line.	8
II.4	Elements of the experimental spectrometer.	11
II.5	Schematic of a typical wire spark chamber.	14
III.1	Variations in monitor rates during part of a typical data run.	22
III.2	The liquid scintillation counter (L).	29
III.3	One-track outline of L-counter.	30
III.4	Signal-size distributions from the L-counter.	34
III.5	Ratio of pulse heights from the L-counter.	36
III.6	Comparison of signals in the L-counter for photon-beam and neutron-beam.	39
III.7	Electron to pion ratio for different targets.	42
III.8	Longitudinal momentum distributions for positive and negative tracks.	44
III.9	Schematic of a track passing through the acceptence.	47
III.10	Limits of the acceptence, y and p_ℓ versus p_T.	49
III.11	Overall reconstruction efficiency.	54
III.12	Total spectrometer sensitivity.	57
III.13	Transverse momentum of tracks exiting through the gap in the lead radiator.	59
IV.1	Multiplicity versus the square of the transverse momentum	63
IV.2	α versus the square of the transverse momentum.	64

Figure		Page
IV.3	α versus longitudinal momentum.	66
IV.4	Multiplicity versus rapidity.	67
IV.5	α versus rapidity.	69
IV.6	α versus the square of the transverse momentum for different regions of rapidity.	70
IV.7	Negative-particle multiplicity from beryllium, as a function of rapidity and pseudo-rapidity	73
IV.8	Contours of equal rapidity and pseudo-rapidity for varying p_T and p_ℓ.	74
IV.9	α versus pseudo-rapidity.	75
IV.10	α versus rapidity and pseudo-rapidity for different regions of longitudinal momentum.	77

CHAPTER I

INTRODUCTION

In this thesis we study the inclusive production of hadrons in neutron-nucleus collisions for incident neutron energies up to 400 GeV. The purpose of the experiment is to measure the dependence of the cross section on the atomic weight of the target. The reason for doing this is that nuclear-target information can provide a more complete description of the strong interaction.

At present, our knowledge of the strong interaction is based essentially on studies of hadron-hadron scattering. In any such experiment we only measure the asymptotic states, and we therefore have very little insight into the nature of hadronic matter at the time of its creation. However, it is possible to affect the early stages of an interaction and learn about hadronic matter at nascency by using nuclear targets. When a high energy projectile collides with a nucleus and interacts with one of the nucleons, the remaining nucleons serve as secondary targets for the re-interaction of the states produced in the initial collision. By varying the atomic number of the targets, one should observe differences in production which should be attributable to the intimate details of the strong

interaction over short space-time intervals. One of the simplest effects to study would be the change with atomic weight (A) in the multiplicity (the number of particles produced per interaction). If, in a hadron-nucleon interaction, the final-state hadrons were completely formed within a distance approximately the size of a nucleon, the products of an initial strong interaction would interact (independently of one another) with the remaining nucleons and would produce a cascading effect leading to a strong dependence of the multiplicity on A. If, on the other hand, particles produced in the initial collision require much time to separate and resolve into their final states, then the multiplicity need not change radically with A. The latter situation could be realized, for example, in a primary interaction producing a correlated or resonant-like system of hadrons which acts as a single object in traversing nuclear matter.

Early observations in cosmic-ray studies[1] have shown evidence for a lack of cascading in nuclei at high energies, and recent measurements at Fermilab[2] have confirmed these findings. In our experiment we provide the first detailed measurements of particle production for essentially the full forward hemisphere of the center of mass, with information on charge, transverse momentum, and longitudinal momentum of hadrons.

Current models of particle production have had substantial success in treating the properties of hadron-production in hadron-nucleus collisions. Multiperipheral models,[3] energy-cascade models,[4] parton models,[5] and other phenomenological ideas[6] have made qualitatively similar predictions concerning the A-dependence of the multiplicity. Our new data should provide a great challenge for these models and point to those most likely to provide a greater understanding of strong interactions.

In this thesis we will describe the experimental apparatus and data taking in Chapter II. Chapter III will involve discussion of the analysis and corrections applied to the data. In Chapter IV we will present the results and conclusions of this experiment.

CHAPTER II

THE EXPERIMENT

A. THE BEAM

The experiment to be described was performed at the Fermi National Accelerator Laboratory (Fermilab) in the M-3 beam-line.[7] The production angle for this neutral secondary beam was 1 mr relative to the incident primary 400 GeV proton beam. The target used to produce the secondary beams at the Meson Laboratory was a 20 cm long bar of Beryllium, which measured .16 cm by .16 cm in the plane perpendicular to the beam.

The elements which comprised the beam-line are shown in Fig. II.1. The beam was limited in the transverse direction by several sets of collimators, while the particle composition was controlled by magnets and filters placed along the beam-line. The first set of collimators (labeled C1) coarsely defined a beam from which the magnet string (BB) extracted the charged particles to form a charged beam-line (M-2). A lead filter (F) was used to convert photons in the remaining beam into charged e^+e^- pairs; this beam was collimated, and the charged component, arising from the lead filter and from collisions of beam particles with the edges of collimators, was removed by the sweeping

The Beam Line

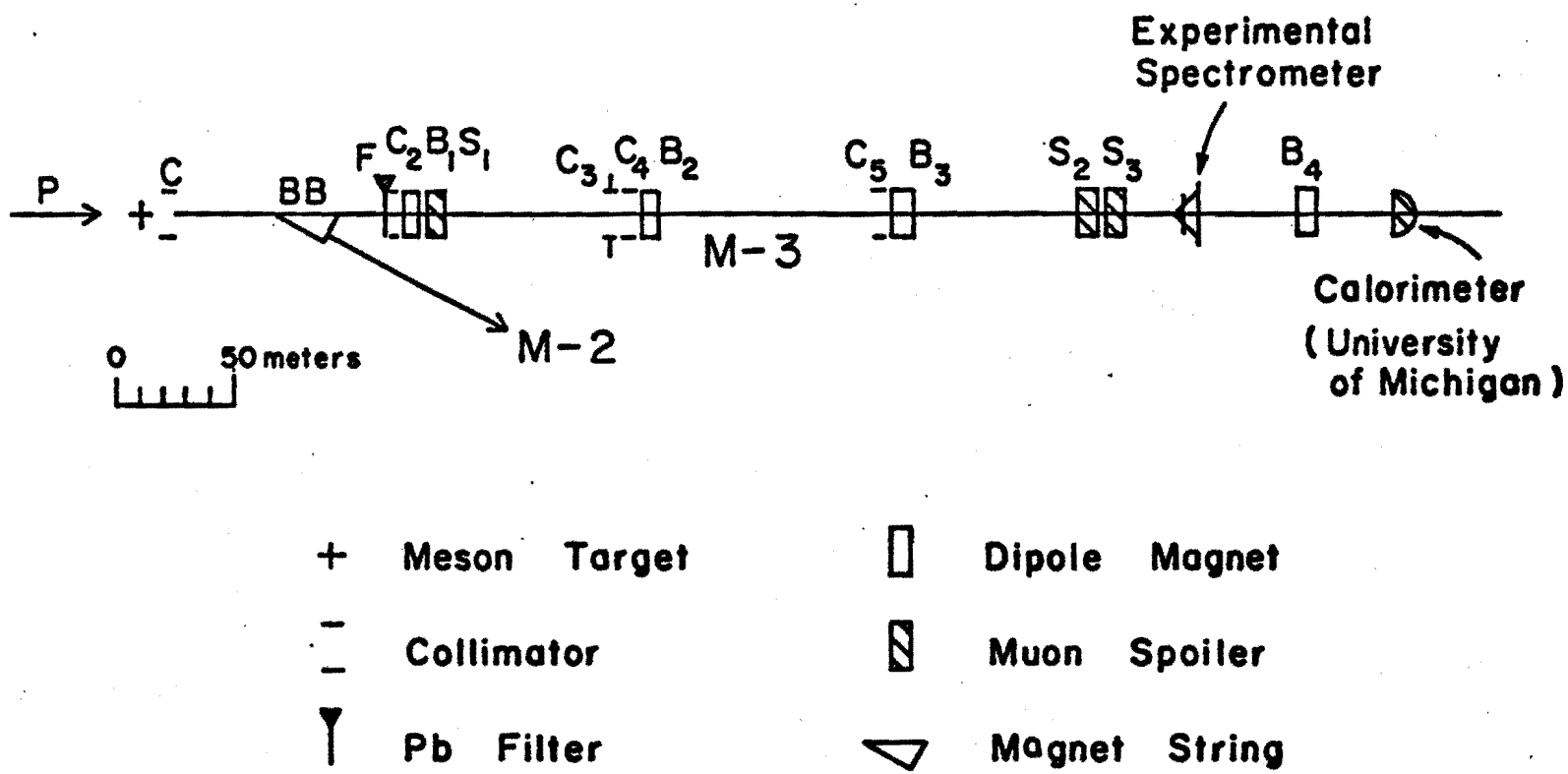

Figure II.1 - Schematic of the M-3 Beam-line

magnet (B1). Stray particles and halo about the beam were further reduced by the magnetized iron of the muon spoiler (S1).

The configuration of beam-line elements, consisting of a set of collimators and a sweeping magnet, was repeated to ensure a well defined neutral beam. A fixed-aperture tubular collimator of variable orientation (C3) was used to further align the beam relative to our experimental spectrometer. A final sweeping magnet (B4) was located behind our spectrometer to ensure that the calorimeter monitored only neutral particles.

For 300 GeV primary proton energy, the neutral-particle composition of the M-3 beam at the production target is shown in Fig. II.2.[8] During normal running, essentially all of the γ-rays were removed from the beam with the aid of the lead filter. This filter was 5 cm thick, which corresponds to approximately 9 radiation-lengths of material, so only 0.01% of the γ-rays remained after the lead filter, as compared to 76% of the neutrons. A large fraction of the K_2^o mesons originating in the target decayed in flight, leaving approximately 1% overall beam contamination from photons and kaons, mainly restricted to energies below 100 GeV. The energy spectrum of neutrons for 400 GeV primary protons is shown in Fig. II.3.[9]

Figure II.2 - Particle composition of the M-3 beam-line with incident proton beam at 300 GeV and no γ filters.

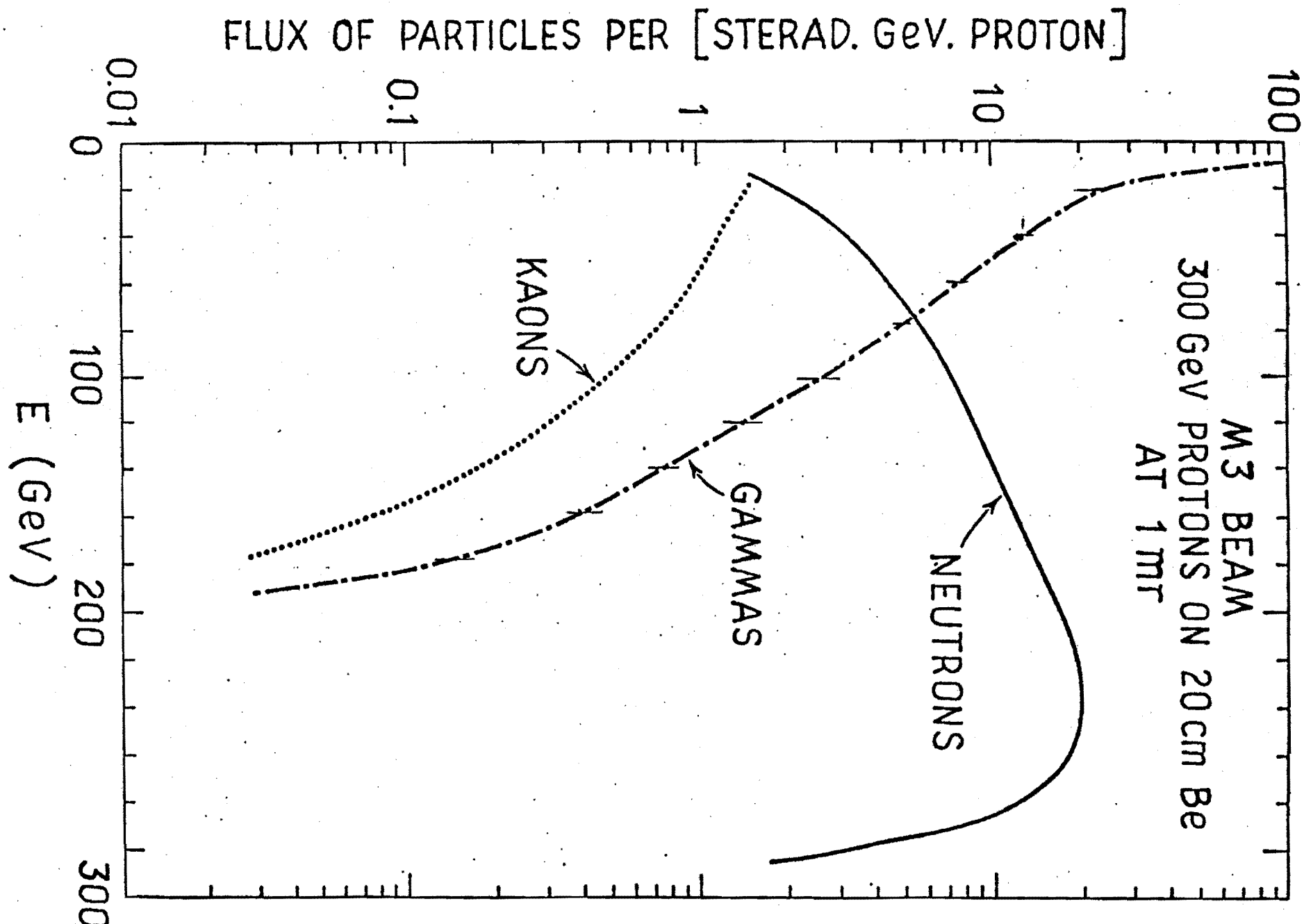

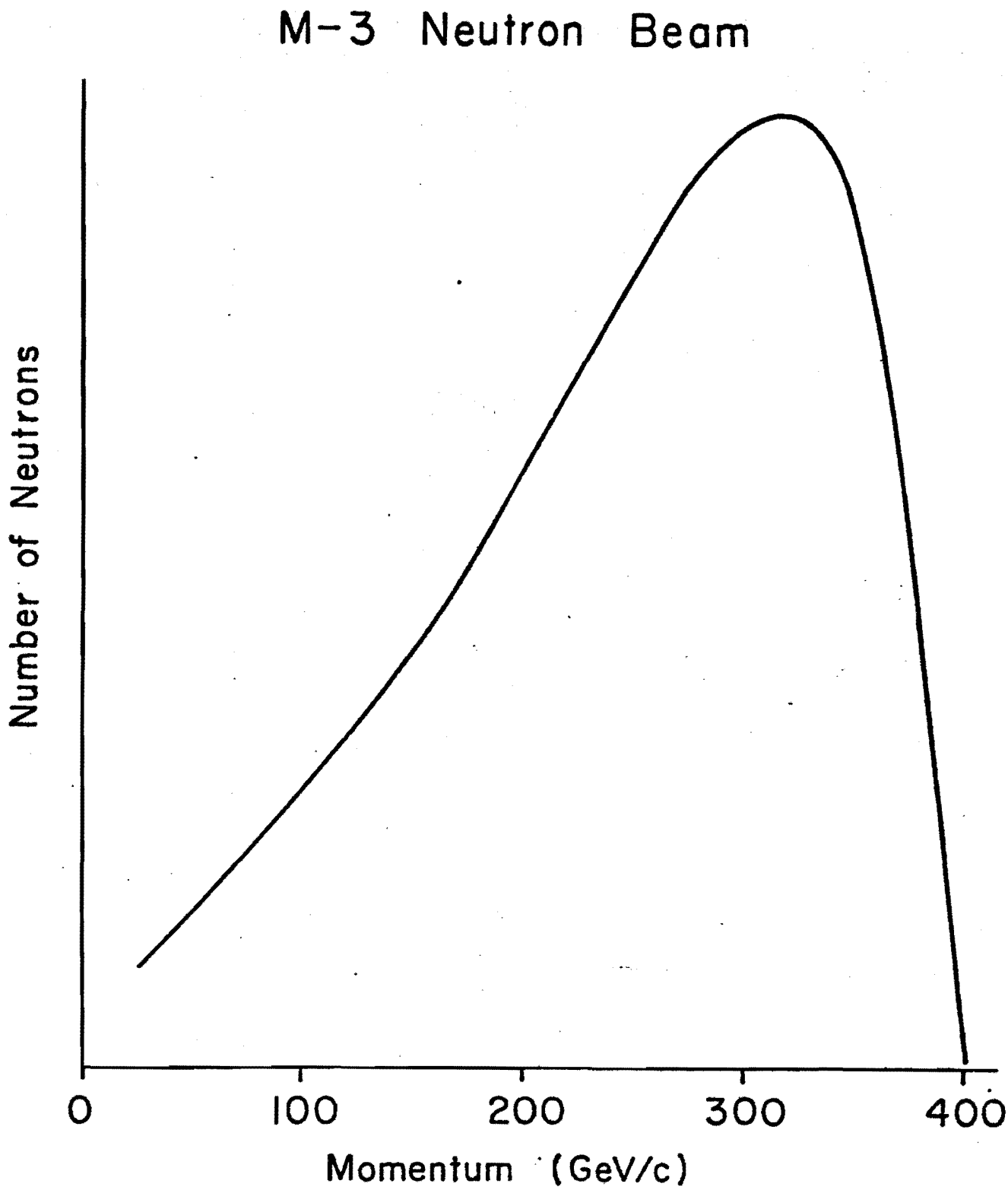

Figure II.3 - Momentum spectrum of the M-3 beam-line with 2 inches of γ-filters in place.

During typical running conditions, there were 5×10^4 neutrons incident on the experimental target, during a beam-spill time which lasted 2 seconds. The transverse size of the beam was about 1 mm x 1 mm.

B. THE TARGET

The targets used in the experiment corresponded to approximately 1% to 5% absorption lengths of material (See Table II.1). In addition to obtaining data using five different nuclei, we also had runs using two different thicknesses of lead (as well as runs with no target in place) to gauge the effects of background and multiple scattering.

C. THE SPECTROMETER

The spectrometer, shown in Fig. II.4, was used to detect interactions in a nuclear target and to measure and record the properties of the charged particles produced in those interactions. Scintillation counters (A,S, and L) were used to detect a suitable event. Fast electronic logic was then used to fire two modules of wire spark chambers (WSC 1 and WSC 2) which measured tracks left by the event. The analysis magnet (BM 109) provided for the determination of the momentum of particles which left tracks which were detected in the spark chamber.

TABLE II.1

PROPERTIES OF THE TARGETS

Element	Atomic Weight (A)	Thickness (ℓ) (cm)	Thickness (ℓ) (gm/cm^2)	ℓ/ℓ_{abs} + (%)	ℓ/ℓ_{rad} ++ (%)
Beryllium	9.01	2.078	3.84	5.66	5.91
Aluminum	26.98	1.798	4.85	4.83	20.2
Copper	63.54	0.645	5.78	4.36	45.1
Tin	118.7	0.632	4.62	2.77	52.2
Lead	207.2	.318	3.61	1.72	56.8
Lead	207.2	.170	1.93	0.919	30.4

+ ℓ_{abs} is the nucleon absorption length for the material.

++ ℓ_{rad} is the radiation length for the material.

Values of the parameters for the nuclei obtained from "Review of Particle Properties", Reviews of Modern Physics, Vol. 48, No. 2, Part II, April 1976.

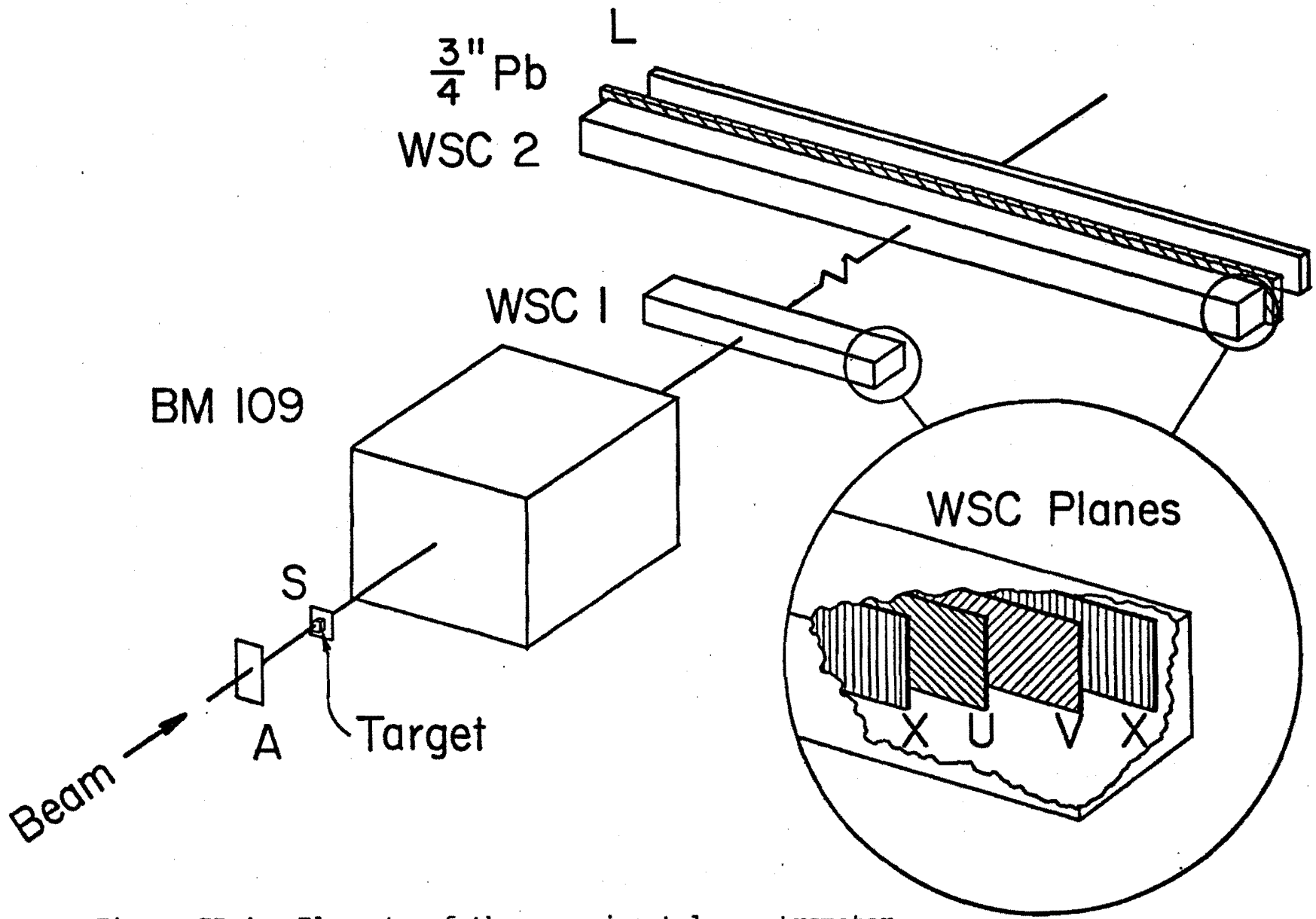

Figure II.4 - Elements of the experimental spectrometer.

1. The Scintillation Counters

The liquid scintillation counter (L) was constructed of 0.125 inch thick aluminum channel, with approximate inside dimensions 4.6 cm along the beam direction, 3.2 cm vertically, and 2.2 m horizontally (perpendicular to the beam). The active part of the counter consisted of scintillator disolved in a mineral-oil base. The channel was closed at both ends by transparent lucite spacers which permitted the transmission of light from the liquid scintillator to photomultiplier tubes attached to the lucite material. The signals from the photomultiplier tubes were used as part of the trigger and were also recorded for use in the off-line analysis.

The L-counter was located at the back end of the spectrometer and a little over 10 meters from the target. Two strips of lead, each 0.75 inches thick, 1.75 inches high, and 45 inches long, were placed end to end with a 2 inch wide separation between them, in front of the counter. This lead was used to generate electromagnetic cascades which could be detected in the L-counter.

Two plastic scintillation counters, A and S, were placed in front of and behind the target. The one in front, A, was 0.125 inches thick, 4 inches high, and 4 inches wide; it was placed about 9 inches in front of the target. The S-counter was located immediately behind the target, and its active portion was a 0.25 inches

diameter disk that was approximately 0.0625 inches thick.

2. The Spark Chambers

Charged particles were detected using two modules of magnetostrictive-readout wire spark chambers (WSC). Each module consisted of four gaps, and each gap was defined by a pair of 40 wire/inch parallel-wire planes. The wire planes were oriented perpendicular to the beam axis; two gaps in each module had vertical wires (X) while the other two gaps had wires inclined at ±15° to the vertical (U,V). The two modules were situated approximately 5 and 10 meters downstream of the target. The spark chamber module located closer to the magnet was 3 cm in the vertical dimension and 1 m in the horizontal; the downstream chamber's aperture was 5 cm by 2.3 m. The narrow slit design provided for relatively simple track reconstruction.

In addition to registering in the scintillation counters, charged particles left trails of ionized molecules and atoms along their trajectories through the spark chambers. Once the fast trigger logic was satisfied (see later, the section on the trigger), a large voltage difference was pulsed between the two planes of wires defining each spark gap (See Fig. II.5). As a result of this pulse, sparks formed between the planes and current flowed in those wires closest to the trajectory of a charged particle. Also, every time

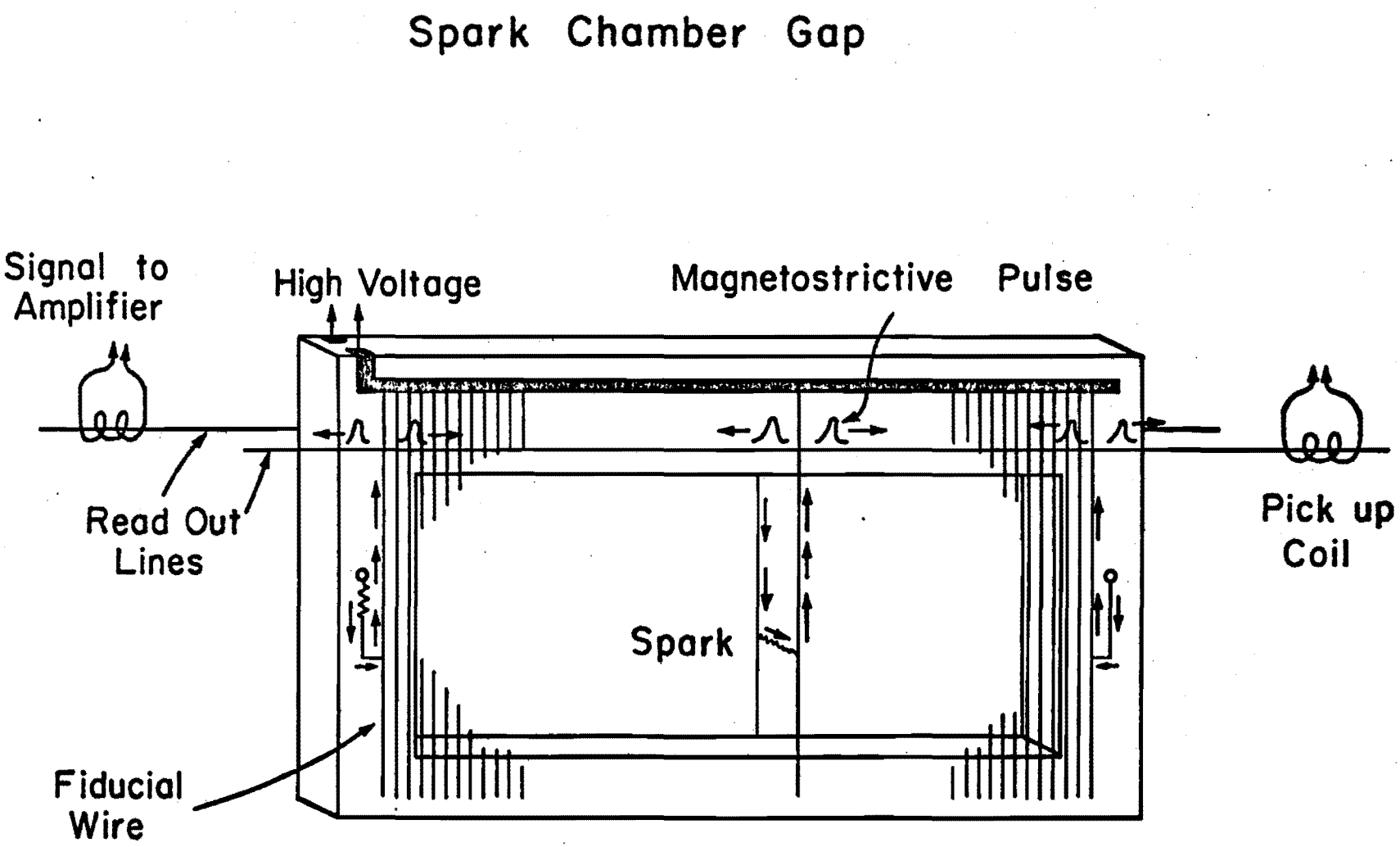

Figure II.5 - Schematic of a typical wire spark chamber.

the high voltage was applied, reference pulses were generated between fiducial-wire pairs located outside the active portion of each of the planes.

An electrically insulated magnetostrictive read-out line was located near the edge of each chamber plane (See Fig. II.5). Any current pulse that appeared on the chamber wires interacted with the static magnetic field of the read-out line and caused a physical contraction of the line at the intersection of the line and the current-carrying wire. These induced contractions generated pulses which propagated along the read-out line in wave trains traveling at the speed of sound. The small longitudinal vibrations along the magnetized read-out line, caused by these wave trains, induced electric pulses in the pick-up coil located at the end of the read-out line.

The signals from each of the pick-up coils were amplified, and then the time intervals separating the first fiducial pulse from successive pulses (caused by sparks and the other fiducial) were digitized into 14-bit scalars using a 40 KHz timing clock. Some measure of redundancy was provided in the system by having read-out lines on both of the wire planes defining a gap, placing the pick-up coils on opposite ends of the read-out lines.

3. The Magnet

Momentum analysis of a track was accomplished through the use of a BM 109 dipole magnet. The aperture through which particles passed measured 8 inches vertically, 24 inches horizontally, and 72 inches along the beam axis. For the range of particle-momenta of interest ($\geq$ 2 GeV/c), the effect of the magnet on particle trajectories could be approximated to good accuracy by a uniform magnetic field in the vertical direction, with a field strength of 9 kG. This field imparted about 0.51 GeV/c of transverse momentum to each charged particle traversing the magnet gap, bending tracks right or left in the horizontal plane depending upon the sign of the charge of the particle.

4. The Trigger

The basic idea of the trigger was, simply, to select those events which had a charged particle. To be acceptable, the charged particles had to pass through the spark chambers and leave tracks which could yield information concerning the momenta of the particles. Because the three scintillation counters (A,S, and L) were sensitive to charged particles that passed through them, an event of interest (i.e., one which would be measured) was required to satisfy all of the following criteria:

i) No charged particle was to be incident on the target (no signal in A).

ii) At least one charged particle had to exit from the target (a signal in S).

iii) At least one charged particle had to exit from the back of the spark chambers (a signal in L).

Consequently, the trigger requirements can be summarized as:

$$\text{Trigger} = \overline{A} \cdot S \cdot L$$

This trigger was very efficient in eliminating interactions initiated by charged particles; however, it was less effective in assuring that triggers originated from interactions in the target (as opposed to those originating in the S counter, say) and that there were good tracks in the spark chambers. These latter two problems will be addressed in the analysis section of this thesis.

D. THE CALORIMETER

The University of Michigan provided us the use of their total-absorption calorimeter,[10] which we used to count the neutrons in the beam. The active area of the calorimeter was 24 inches square, perpendicular to and centered on the beam; the device was situated about 100 meters downstream from our target. This calorimeter was the same one which was used to determine the particle-

composition of the neutral beam.[8,9]

E. DATA ACQUISITION

Every time an acceptable event was detected and the spark chambers fired, several pieces of information were gathered and stored for later analysis. Basically, the method was to convert all the information into digital data, process it in a computer, and then put it on magnetic tape. The counters, such as the trigger counters, the calorimeter, etc, were connected to scalers which recorded the number of times each counter fired during a beam spill. The spark-chamber outputs were put through time-to-digital converters which stored the relevant numbers of clock counts for the time intervals between fiducial and track sparks. The photomultiplier signals from the L-counter were integrated using analog-to-digital converters, yielding numbers proportional to the amounts of light detected at each end of the L-counter. All these digital numbers were collected using CAMAC modules and an interface controlled by a DEC PDP-15 computer. The computer was programmed to monitor the performance of the experimental apparatus and to transfer the digital information for each event to a magnetic tape for subsequent off-line analysis.

CHAPTER III

DATA ANALYSIS

The data for this experiment was obtained in about three days of running time. Approximately 100,000 triggers were collected during this time interval, with the data divided among five target nuclei. Table III.1 summarizes the results of the data gathering stage of the experiment. In the rest of this chapter we will discuss the techniques used in the analysis of the data.

Preliminary track reconstruction and data reduction were performed on the tandem CDC-6600 computers at Fermilab. Reconstructed track information, pulse height values, and counter information for each event were extracted and then recorded on a summary tape. The summary tape was then processed on the University of Rochester's PDP-10 computer.

A. BEAM-LINE MONITORING AND NEUTRON COUNTING

The University of Michigan's calorimeter was used primarily to measure the number of neutrons incident on our target; but it was also used, with the aid of other monitoring counters, to judge the quality of performance of the spectrometer system. In the following three subsections we will discuss the monitors used during the execution of this experiment.

TABLE III.1

DATA SUMMARY

Target	Calorimeter Counts	Triggers	Tracks Observed
Beryllium	432,232	19,716	19,404
Aluminum	460,418	21,069	21,227
Copper	659,466	29,239	29,990
Tin	930,771	27,323	28,200
Lead (1/16")	659,470	8,594	8,572
Lead (1/8")	910,537	16,810	17,363
Empty	2,891,541	10,620	9,954

1. Monitoring of the Beam

There were several methods available to monitor the stability of the beam. In the target hall of the Meson Laboratory there was a Secondary Emissions Monitor (SEM) which registered particles produced at a fixed angle relative to the primary proton beam. When the ratio of SEM to calorimeter counts changed during a run, it was usually because the 'targeting' angle of the primary protons had changed. This kind of change could alter the energy spectrum of the secondary neutrons in the M-3 beam, and therefore the ratio of SEM to calorimeter counts was a valuable gauge of the stability of the beam characteristics. Additional counters, for monitoring background levels near our target, for counting the total number of interactions during the beam pulse, and for measuring the time elapsed between interactions, were available for performing diagnostics.

To measure the stability of the data-taking process, all monitors were summed off-line for groups of 150 events at a time. A sample of this kind of monitoring, for a typical run, is displayed in chronological event-number order in Fig. III.1. The figure shows:

a) The number of $\bar{A}\cdot S\cdot H$ counts, where H was a six-element hodoscope covering the exit aperture of the BM109 magnet; this is proportional to the number of interactions in the target.

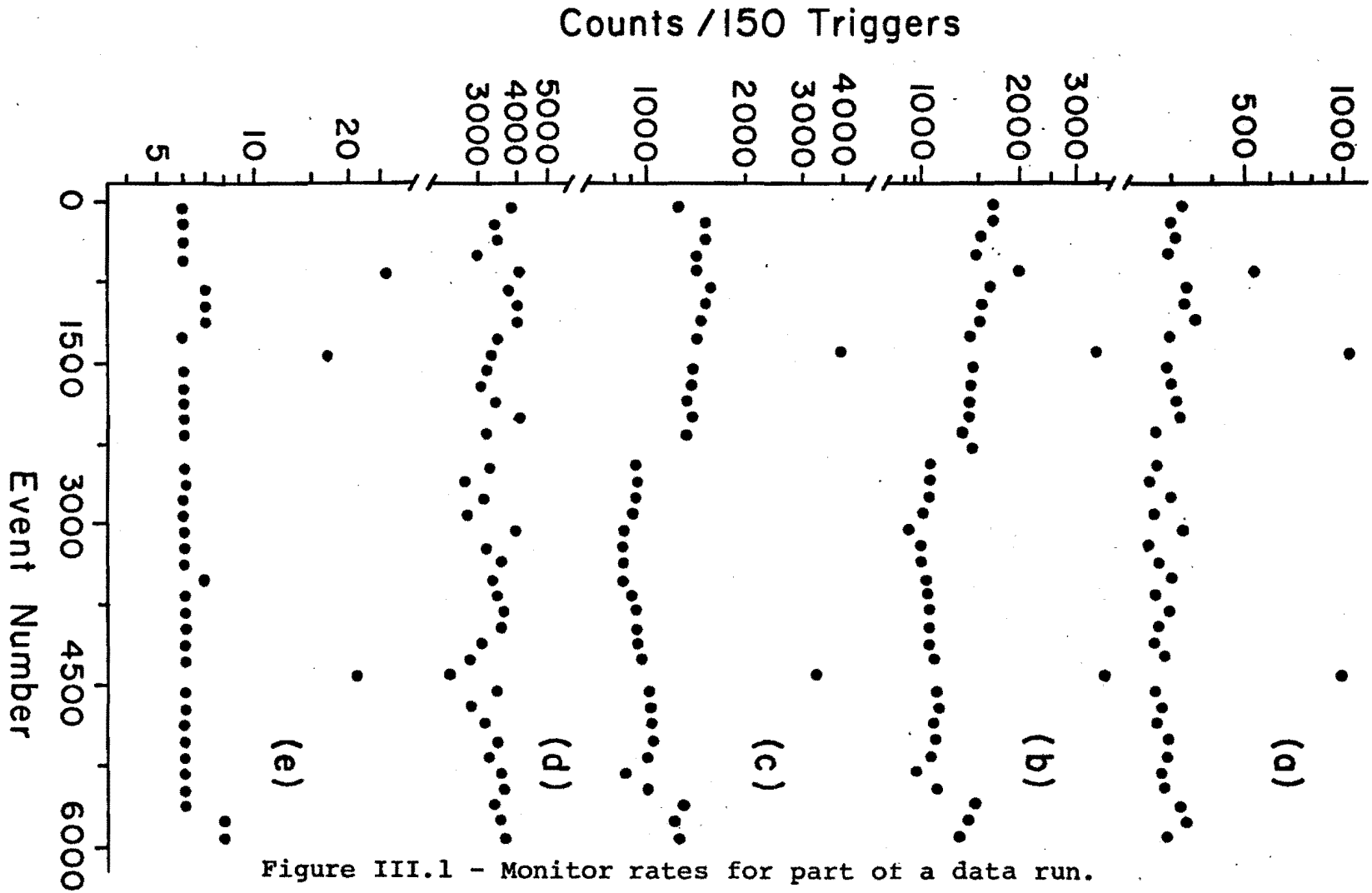

Figure III.1 - Monitor rates for part of a data run. Parts (a), (b), (c), (d), and (e) represent the counts per 150 triggers for $\bar{A}\cdot S\cdot H$ (i.e., interactions), A, SEM, calorimeter, and spills respectively.

b) The number of counts in the A counter (background)

c) The number of SEM counts

d) The uncorrected number of counts in the calorimeter

e) The number of beam pulses (each was two seconds long)

all for intervals of 150 events. For the sample shown, the ratio of counts in the calorimeter to the number of events was unusual only for one group of events (near 2250); indeed, that group of events was so unusual that all the monitors, except for the A counter, were off-scale and are not plotted in the figure. Because of the departure from the norm, that group of events was removed from the data sample. The other deviations were consistent with stemming from reduced flux in the main accelerator beam, and so no other adjustment to this data sample was made.

2. Measurement of Neutron Flux

The flux of neutrons incident on our target was measured using the Michigan group's total-absorption calorimeter. Since the calorimeter was located about 100 meters downstream of our apparatus, the amount of material through which the beam had to pass after impinging on our target was substantial. This intervening material could scatter the beam and reduce the number of neutrons detected in the calorimeter. Table III.2 shows details about the items in the beam line which were located between our target and the calorimeter. (One nucleon-

TABLE III.2

MATERIAL IN BEAM BETWEEN TARGET AND CALORIMETER

Object	Thickness (ℓ)	Nucleon Absorbtion Length (ℓ_{abs})+	ℓ/ℓ_{abs} (%)
L-Counter			
Scintillator	4.64 cm	70 cm*	6.58 ± 1.0
Aluminum	.635 cm	37.2 cm	1.71 ± .03
S-Scintillator	.159 cm	68.5 cm	.22 ± .01
H-Hodoscope	.318 cm	68.5 cm	.44 ± .02
D-Telescope			
Lucite	.95 cm	65.0 cm	1.47 ± .05
Scintillator	.635 cm	68.5 cm	.88 ± .05
WSC 1 and 2			
planes	8 gaps	.03%/gap	.24 ± .2
misc.			.24 ± .2
Other WSC in beam	26 gaps	.03%/gap	.78 ± .6
Air	28 m	675 m	4.15 ± .03
E-248 H_2 Target	30.5 cm	790 cm	3.86 ± .02
Air/Vacuum	82.m	1250 m**	6.56 ± 6.
misc. (Vac. windows, counters)			2.0 ± 1.
	TOTAL:		28.68 ± 8.%

+"Review of Particle Properties", Rev. Mod. Phys. Vol. 48, No. 2, part II, April 1976.

*Estimated as being average of scintillator and H_2O.

**Assumed to be half air and half vacuum.

absorption length represents the thickness of material through which the neutrons would have to pass to reduce the number of non-interacted neutrons to 1/e of the original value.) The largest uncertainty in this evaluation arises from the fact that we could not later determine if there was air or vacuum downstream of our apparatus. Independent checks (using a crude 'Interaction' trigger) indicate that the calorimeter might have been counting 5-10% lower than can be accounted for (see Appendix).

The limiting aperture preventing beam particles from reaching the calorimeter was the 6-inch diameter beam pipe located between the last sweeping magnet (downstream of our equipment) and the calorimeter (see Fig. II.1). When an inelastic collision between a neutron and material in the beam-line produced a neutron of sufficiently high momentum ($P \geqslant 50$ GeV/c) and small enough angle relative to the beam axis ($\theta \lesssim 2$ mr), the produced neutron could register in the calorimeter as a beam particle. Thus, not all inelastic collisions downstream of our target led to the loss of incident-neutron counts. From data on inclusive proton production in pp collisions,[11] we estimate that $\geqslant 95\%$ of the inelastic collisions between beam neutrons and material in the beam-line (including our target) were not counted in the beam flux. In the estimate we assume charge independence and that there is very little dependence of production on atomic number in the forward direction of the center of mass.[12]

In addition to inelastic scattering, elastic scattering of the beam neutrons must also be considered in the calculation of the beam flux. The shape of the elastic scattering distribution for neutrons can be approximated as follows:[13]

$$\frac{d\sigma}{dt} \alpha \exp[10tA^{2/3}]$$

where t is the square of the momentum transfer ($\approx -p^2 \sin^2 \theta$), p the momentum (in GeV/c) of the elastically scattered neutron, θ the polar production angle in the laboratory, and A the atomic weight of the scattering nucleus. For an atomic weight A = 20 (typical of the material in the beam), and for the mean momentum of $\sim$300 GeV/c, less than 1% of the elastic collisions escaped detection in the calorimeter. These losses are somewhat momentum dependent, but we use an average value in the small corrections to the neutron flux.

B. CORRECTIONS TO THE DATA

Three main corrections were applied to the data so as to obtain the hadron production spectrum. First, from data accumulated with no target in place, we performed a background subtraction from data taken with nuclear targets in the beam. Next, electron and positron contamination was studied and mostly removed from the data sample through the use of the L-counter (see Chapter II). Finally,

using cuts on the momentum of outgoing secondaries, we were able to assess the effect of the proton component of the (pion-dominated) production data.

1. Empty-Target Data

Most of the triggers in this experiment originated from interactions in the sundry nuclear targets. However, there were also events from interactions which occured in the counters positioned in front of and behind these targets. This kind of event, along with the rare category of events arising from random coincidences of stray background radiation, could be studied in the absence of the nuclear targets. Qualitatively, the size of this background component in the data can be gauged from the entries in Table III.1. The number of reconstructed tracks per calorimeter count indicates that the size of this background component ranged from 8% for beryllium to 28% for the thinner lead target.

Once the neutron-flux corrections were made and each separate data run properly normalized, distributions of physical interest (for the target-empty run) were subtracted, bin by bin, from the corresponding distributions from nuclear-target data to obtain cross sections.

2. Electrons

A source of background to charged-pion production in the data was due to the conversion of π° mesons. Electrons

and positrons from these π° conversions could be separated, on a statistical basis, from other detected particles by examining the pulse height observed in the L-Counter. The following subsections discuss the properties of the L-counter and the methods we used to separate electrons from hadrons.

2a. The vertical aperture of the L-counter

The liquid scintillation counter (L-counter), located at the downstream end of the spectrometer, was used both in the triggering and in electron identification. The vertical size of the L-counter was less than that of the active area of the spark chambers (see Fig. III.2b), and hence the counter formed the limiting aperture for the spectrometer. Indeed, the region of acceptance for the L-counter was well away vertically from the edge regions of the spark chambers where track efficiency might have been poor.

To locate the vertical position of the L-counter relative to the beam, we plotted the number of reconstructed tracks (from events having only one track) as a function of position. The results shown in Fig. III.3 indicate that a number of the supposedly single-track events had no track traversing the counter (the spark-chamber resolution, from wire spacings, should have been 0.5 mm). This can be attributed to two sources. First, the somewhat oversized electron radiator (0.75-inch thick lead strips

L - Counter

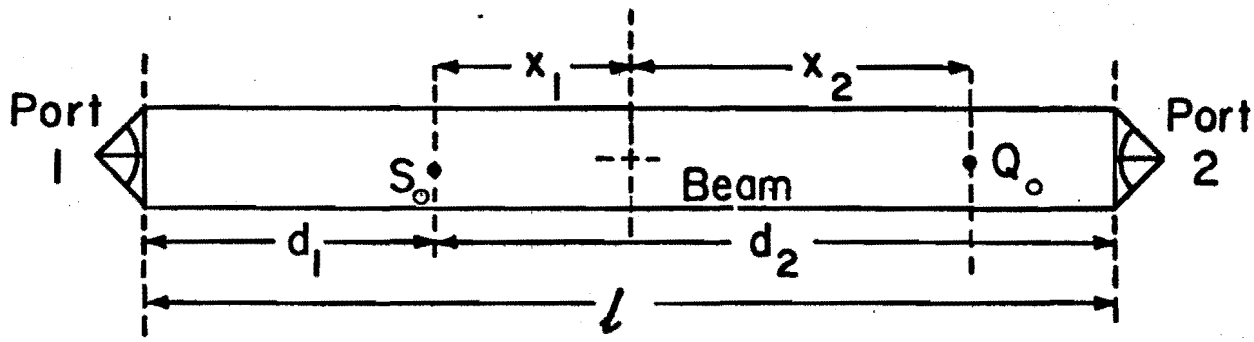

a) Front View

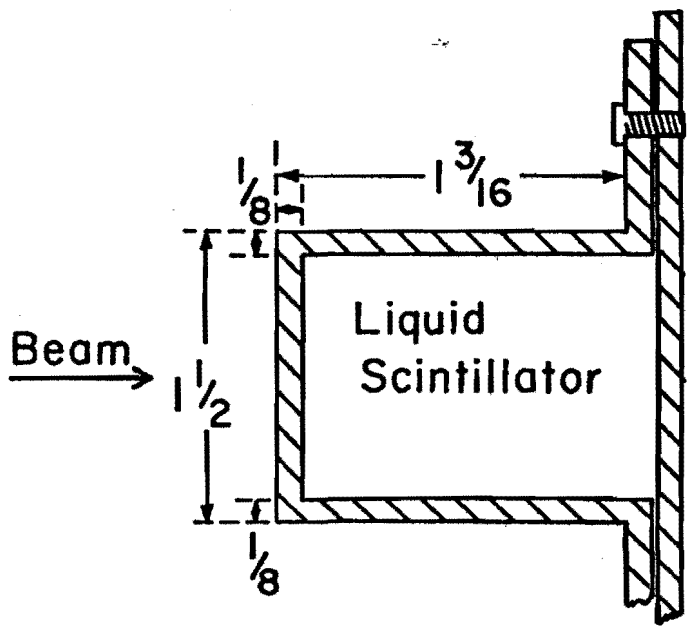

b) End View

Figure III.2 - The L-counter. (a) Front view, showing the definitions of distances describing two tracks giving signals S_o and Q_o. (b) Side view, showing aluminum housing.

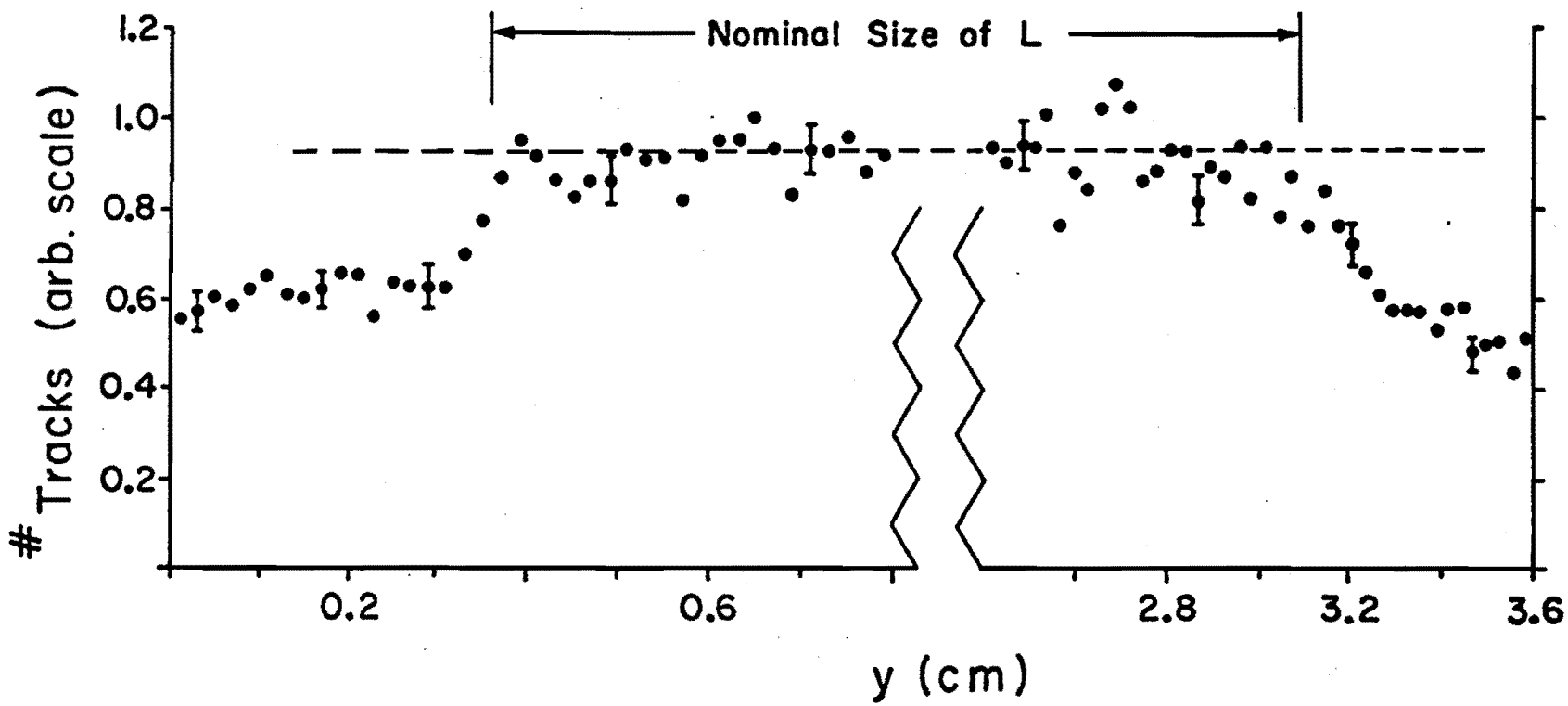

Figure III.3 - Single-track events displayed versus the vertical dimension. The length of the plateau corresponds to the nominal size of the L-counter.

positioned ∿2" in front of the counter) provided material for hadronic reactions that produced secondary particles which then traversed the counter (even though the incident particle could not). Second, tracks which miss the L-counter could have been accompanied by photons which converted in the lead to produce the trigger signal in L. The estimated magnitudes of these two sources account for the 30% of the tracks which miss the L-counter.

The known physical dimensions of the L-counter and its reconstructed vertical size agree quite well. From this agreement we deduce that the resolution of the spectrometer in the vertical dimension is at least ±1.0 mm, and may be as good as ±0.5 mm (the value calculated from the wire spacings of the spark chambers).

2b. Signals in the L-counter

After a charged particle traversed the L-counter, the scintillation light so produced was transmitted in both directions along the length of the counter to the photomultipliers. The transmission properties of the counter are governed by internal reflection at the surfaces and attenuation in the medium. The light observed at either end of the counter depends directly on the amount of light produced at the source and on the distance to the source. Using the definitions given in Fig. III.2a and defining

the initial intensity as S_o, the pulse-heights obtained at the photomultipliers for a single-track event are:

$$P_1 = A_1 S_0 \exp(-d_1/\lambda)$$

$$P_2 = A_2 S_0 \exp(-d_2/\lambda)$$

where λ represents an effective attenuation length, d_1 and d_2 the distances from the source to the photomultipliers, and A_1 and A_2 the amplifications of the respective photon-detection systems. The value of λ is a function of the geometry of the counter and of the natural attenuation length and surface characteristics of the liquid scintillator. The amplification factors, A_1 and A_2, vary slightly over the range of light intensity reaching the photomultipliers (i.e., the amplification is somewhat non-linear).

If all of the tracks traversing the L-counter are detected, then for one- and two-track events we can calculate quantities proportional to the original signals. For a single track in the counter, the signal size (C) can be calculated from:

$$C^2 \equiv P_1 P_2 = A_1 A_2 \exp(-\ell/\lambda) S_0^2 ,$$

assuming that λ, A_1, and A_2 are constants. For events with two tracks reconstructed as striking the L-counter at distances x_1 and x_2 from the center point of the L-counter,

the above relation becomes:

$$C^2 = A_1A_2\exp(-\ell/\lambda)[(S_0+Q_0)^2 + 2S_0Q_0(\cosh((x_1-x_2)/\lambda) - 1)].$$

The distributions of C for events with one and two tracks are shown in Fig. III.4. As expected, the distribution for two-track events is wider, and it has a peak at approximately twice the signal size as that of the one-track events. The long tails on both distributions arise from fluctuations in S_0 (above that for one minimum-ionizing particle), variations in the counter's photon-collection system, and from stray (unreconstructed) particles also striking the counter.

2c. Attenuation length in the L-counter

The simplest method for determining the attenuation length of the L-counter is to examine the detected pulse height in a photomultiplier versus the distance of the source from that photomultiplier. The variation in signal sizes and the non-linearity of the photomultipliers, however, introduce factors which make λ appear to depend on position when λ is measured using only one photomultiplier. But, using both of the observed pulse heights together, we can extract the attenuation length from data on one- and two-track events.

If the two pulse heights at either end of the L-counter are written as in the previous section, then their ratio is:

Figure III.4 - Signal size ($\sqrt{P_1 P_2}$) distributions (in ADC counts), for events with one and two tracks observed. The rightmost bin includes the overflows (above 1023 counts).

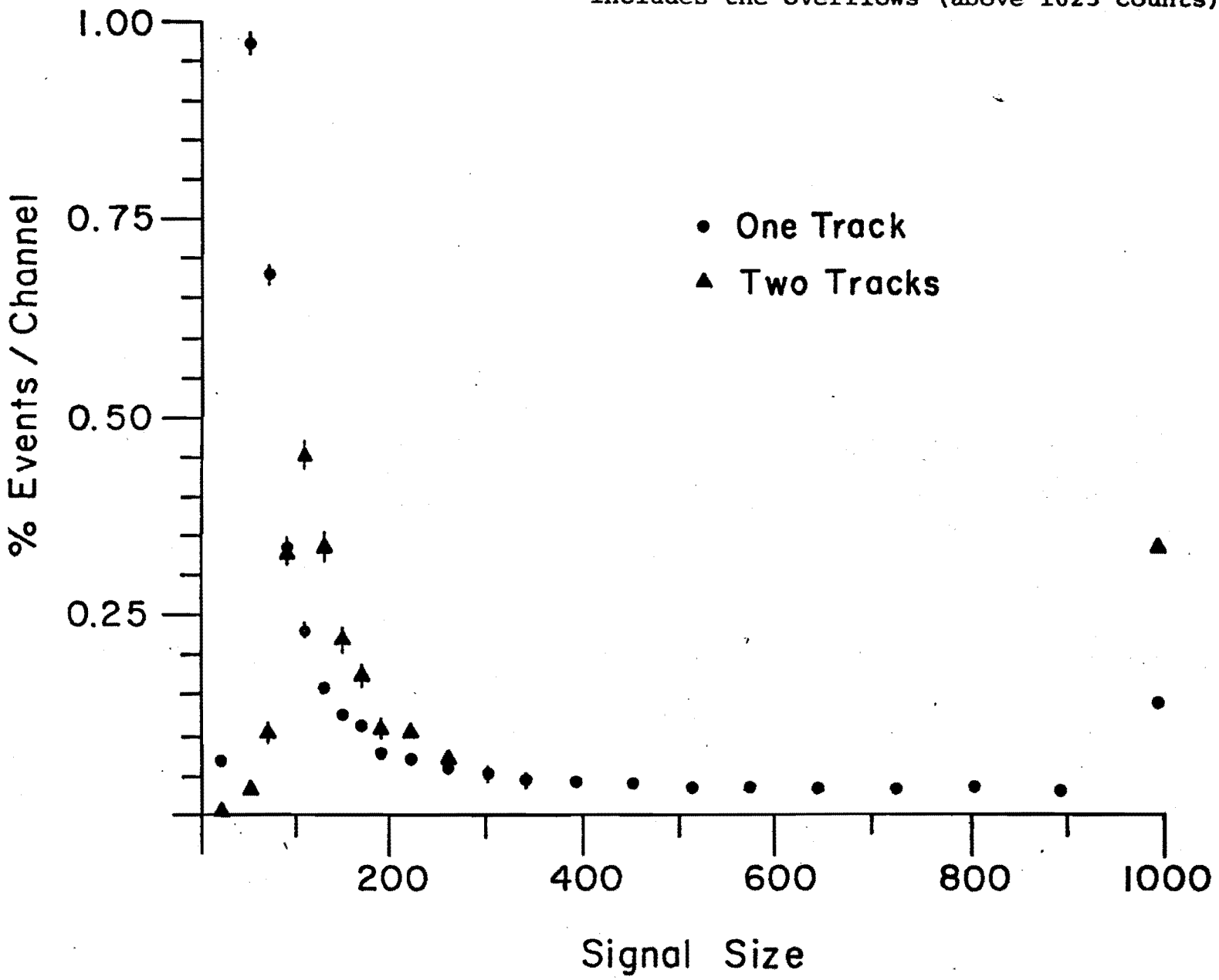

$$P_1/P_2 = (A_1/A_2)\exp[(d_2-d_1)/\lambda].$$

The difference $(d_2 - d_1)$ can be expressed in terms of the distance of the track from the center point of the L-counter as $2x_1$. Thus, the above ratio can be written as:

$$P_1/P_2 = (A_1/A_2)\exp\ (2x_1/\lambda).$$

The above is valid for single-track events. For two tracks in an event, with the second track having a signal Q_0 at some position x_2, the observed pulse heights become:

$$P_1 = A_1[S_0\exp(-\ell/2\lambda + x_1/\lambda) + Q_0\exp(-\ell/2\lambda + x_2/\lambda)]$$

$$P_2 = A_2[S_0\exp(-\ell/2\lambda - x_1/\lambda) + Q_0\exp(-\ell/2\lambda - x_2/\lambda)].$$

Assuming $S_0 = Q_0$ (which is true on the average), then the ratio becomes:

$$P_1/P_2 = (A_1/A_2)\exp[(x_1 + x_2)/\lambda]$$

In Fig. III.5 we show the ratio of P_1/P_2 (for signals $C = \sqrt{P_1P_2} \leqslant 150$ counts) for one-track events as a function of position along the counter (x_1) in part a), and for the two-track events as a function of (x_1+x_2) in part b).

Figure III.5 - Ratio of pulse heights from the L-counter. (a) Single-track events versus the position x_1; (b) Two-track events versus $x_1 + x_2$. The straight lines represent fits for the attenuation length. Error bars are smaller than the size of the points.

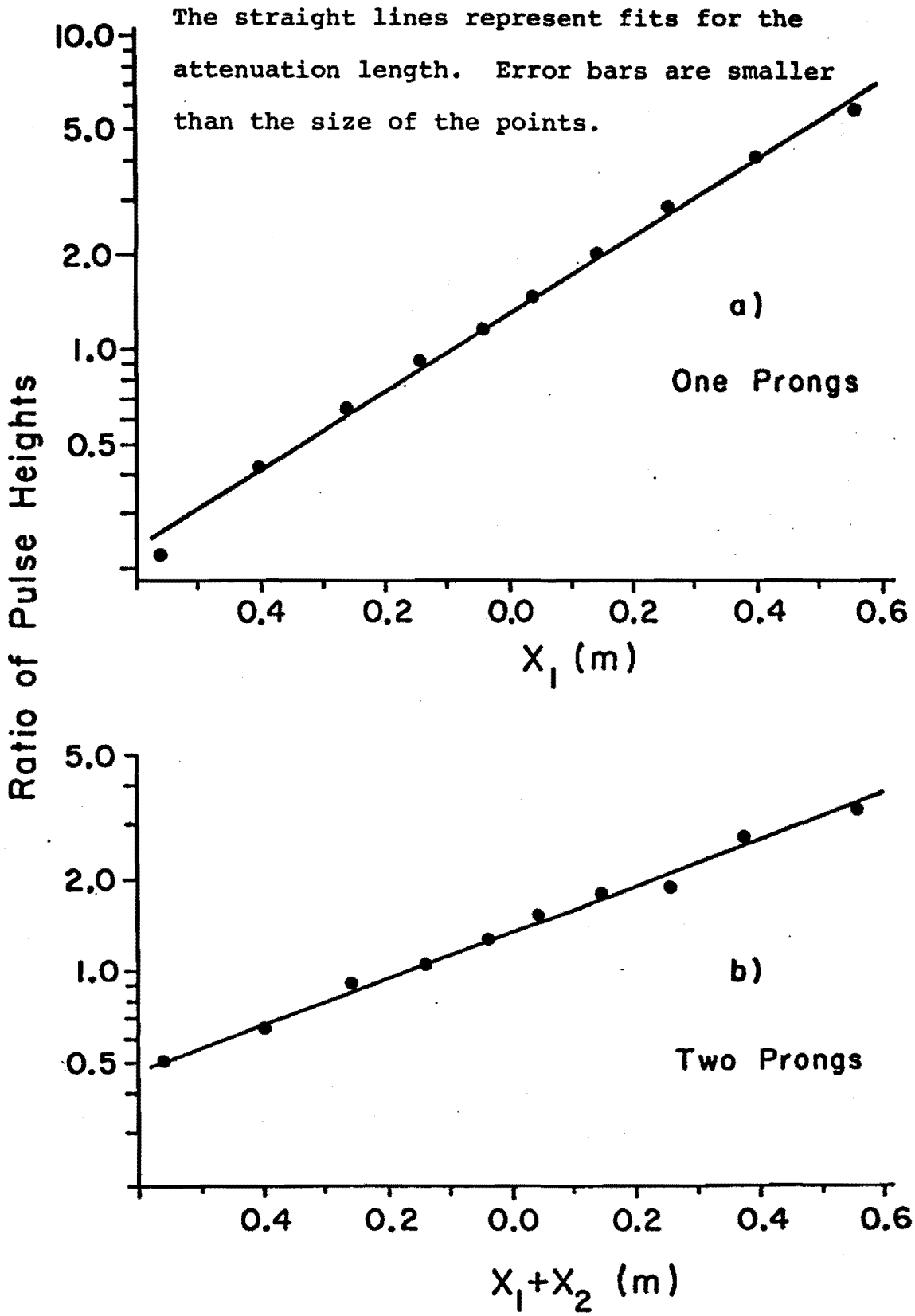

The straight lines are fits to the data points in the figure. The resulting values of λ calculated from part a) is $0.71 \pm .01$ meters, and that from part b) is $0.58 \pm .02$ meters. These somewhat different values obtained for λ reflect the non-linearities in the light collection and amplification systems. The smaller value of λ from Fig. III.5b could be the result of the inequality of the two signal sizes (S_0 and Q_0) for two-track events and the bias introduced by the requirement that the signal size be greater than 150 counts.

2d. Identification of electrons

Having determined that the L-counter detects single and multiple tracks in a reliable manner, we next discuss its use in our identification of electrons (positrons). The lead strips located in front of the counter served as a radiator for electrons and photons which traversed the spark chambers. The electromagnetic showers so produced in the lead were characterized by large amounts of energy deposited in the L-counter.

To determine the kind of pulse heights to expect from electron showers produced in the lead, we ran for a short time with a photon-enriched beam; this was achieved by removing the γ filters which were located about 116 meters from the Meson Laboratory's production target (see Chapter II). The distribution of signals ($\sqrt{P_1 \cdot P_2}$) from the

L-counter for this run is compared in Fig. III.6 to the distribution obtained during normal running conditions. (In both cases a 0.125 - inch thick lead target was used.) The sample of tracks from the "photon" run should be enriched in electron content; and, in fact, this sample does show a preponderance of pulse heights above the maximum value that could be digitized. (The maximum pulse height was set by the 10-bit accuracy of the analog-to-digital converters used to measure the output signals from the photomultipliers on the L-counter.) For signals below the value of 500 counts, the photon-run distribution is consistent in size and shape with being produced by the neutron component of the beam interacting in the target.

Charged hadrons produced in neutron-nucleus interactions can also interact inelastically in the lead radiator and sometimes yield large pulse-height signals in the L-counter. Photons (and electrons), which essentially always ($\sim$99% of the time) produce electromagnetic showers in the radiator, originate mainly from π^o and η^o decays (and their conversions). In contrast to photons, electrons leave observable tracks in the spark chambers which we confuse with charged hadrons; the fact that electrons shower, and tend to always provide large signals in the L-counter (while hadrons do not), can be used to reduce electron contamination in our data.

To estimate the electron background we will assume

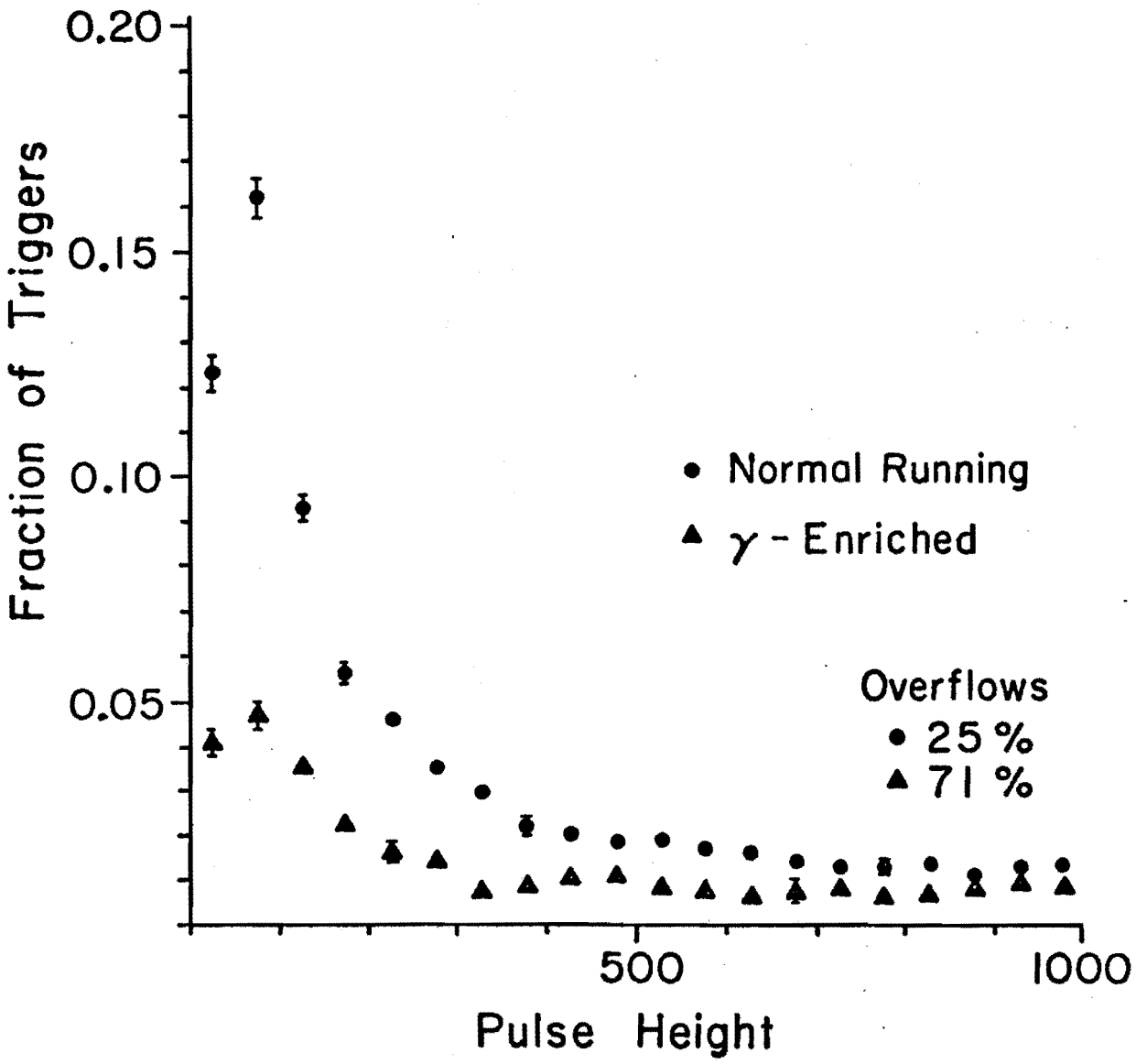

Figure III.6 - Comparison of the pulse height (P_1) distributions for the 1/8-inch lead target, using neutron and photon enriched beams.

that all electrons stem from the conversions of π^0 mesons in the target, and we will make the additional approximations that, on the average, the two photons from the decay of the π° have equal momenta and that the e^+e^- pair from the photon conversion also split the momentum of each photon. Assuming statistical production of pions, the π° momentum distribution should be similar to the average of the π^+ and π^- spectra. Consequently, to first order, the electrons would be expected to have the same angular distribution as the pions but only a quarter of the momentum. We estimate that the integrated e/π ratio for produced particles (ignoring the momentum acceptance of the spectrometer) would range from 6% for the beryllium target to about 50% for the thicker lead target. Most of these electrons, however, would have relatively low momenta.

To discriminate between true electron showers and hadronic interactions simulating such showers (we estimate that approximately 14% of the pions interacted in the lead and gave large signals in the L-counter), we took advantage of the fact that the pion momentum spectrum cuts off essentially at $\sim$100 GeV/c, and so the electron momenta are $\lesssim$ 25 GeV/c. We eliminated from consideration particles with momenta below 25 GeV/c if either: (1) both pulse heights from the L-counter were overflows, or (2) the track in question passed through the gap in the lead radiator (i.e., no electron discrimination was available). Those tracks with momenta below 25 GeV/c, that did

not satisfy either (1) or (2) above, were accepted as hadrons and corrected to account for losses due to the cut at 25 GeV/c.

Using the above criteria to define electron candidates, the ratio of electrons to pions was estimated separately for each target sample and plotted as a function of the number of radiation lengths of material (ℓ/ℓ_{rad}) present in the target (see Fig. III.7). If our criteria were correct, we would expect the extrapolation to no material (ℓ=0) to provide us with the fraction of hadrons that simulate electron-like signals in the L-counter. (The target-empty result, which corresponds essentially to $\ell = 0$, is plotted at a value of zero radiation lengths.) The straight line in Fig. III.7 is a least-squares fit to the data points (excluding the one at $\ell = 0$) which yields the estimated e/π ratio of $.122\pm.006+(.083\pm.015)\ell/\ell_{rad}$. The extrapolation to $\ell = 0$ is consistent with the results from the target-empty run and also consistent with the $\sim$14% estimate for the fraction of pions which interact in the radiator and are mistaken for electrons. Thus it appears that the electron background is reasonably understood in this experiment.

3. Protons

In the kinematic region of projectile fragmentation in neutron-nucleus collisions, the ratio of negative to

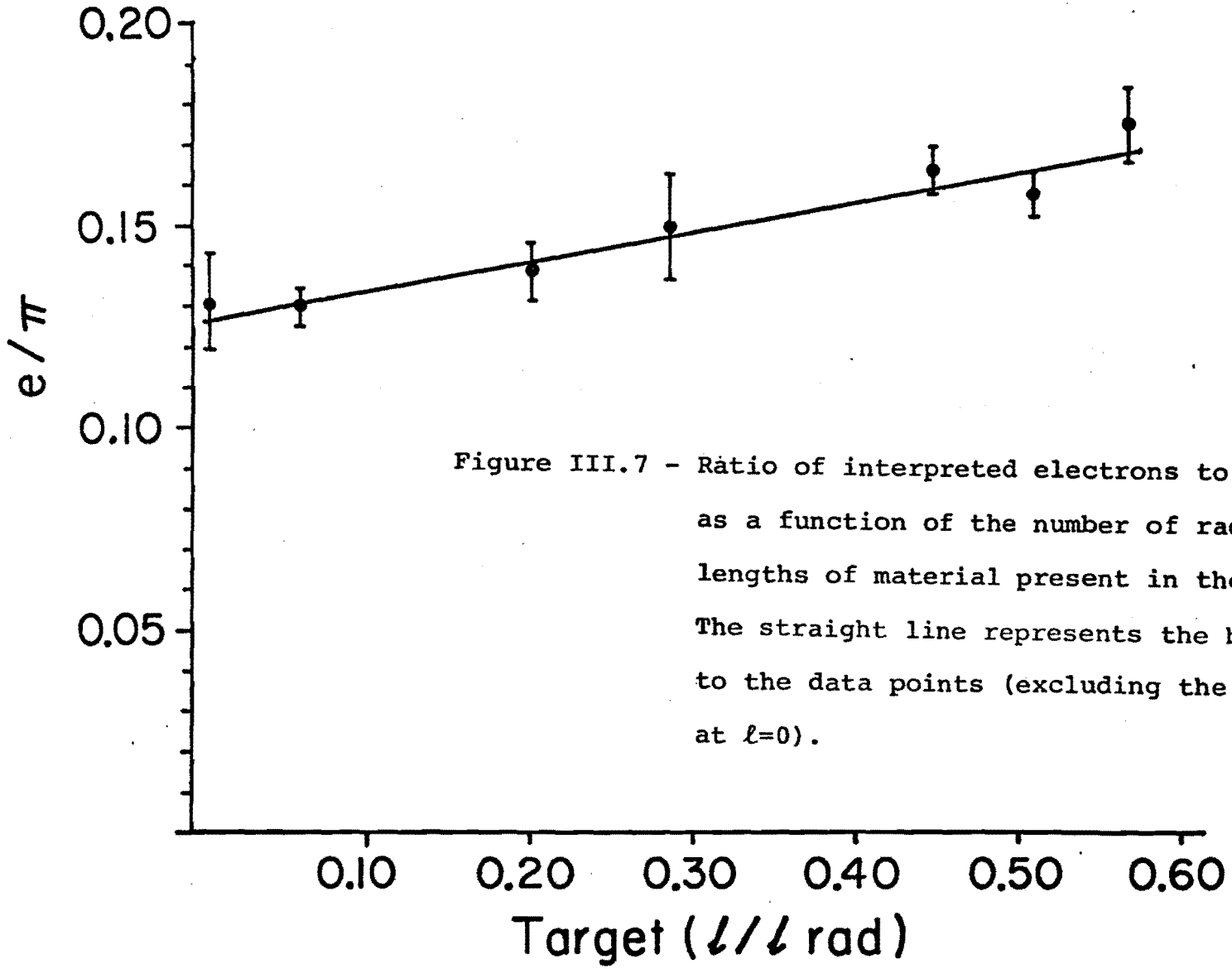

Figure III.7 - Ratio of interpreted electrons to pions as a function of the number of radiation-lengths of material present in the target. The straight line represents the best fit to the data points (excluding the point at $\ell=0$).

positive-pion production should be about 3:1. This ratio can be estimated from results of experiments on inclusive pion production in pp reactions,[14] assuming charge symmetry and factorization; the latter means that the projectile fragmentation process is essentially independent of the kind of target used in the scattering.[15] Thus we might naively expect far more negative particle production than positive particle production at large longitudinal momenta. However, the contribution in this region from the fragmentation of the neutrons into protons becomes substantial relative to the pion contribution. In fact, it is expected that, at the very largest longitudinal momenta, the positively-charged hadron spectrum will be dominated by protons. Since there is very little antiproton production expected in this experiment, it would not be surprising if, instead of observing an excess of negative hadrons at large momenta, the opposite were true. (There are K^- and K^+ components in the hadron spectra, in addition to the p and $\bar{p}$ fractions present; however, kaons do not appear to dominate over pion production in any region of phase space).

In Fig. III.8 we plot the positive and negative-hadron momentum spectra, corrected only for geometric losses (all targets). Positive particles are more copious than negative, and the difference is more pronounced at the larger momenta. Consequently, as indicated above, this result can be interpreted as being caused by the presence of protons in the

Figure III.8 - Longitudinal momentum distributions for reconstructed tracks, corrected for geometric losses.

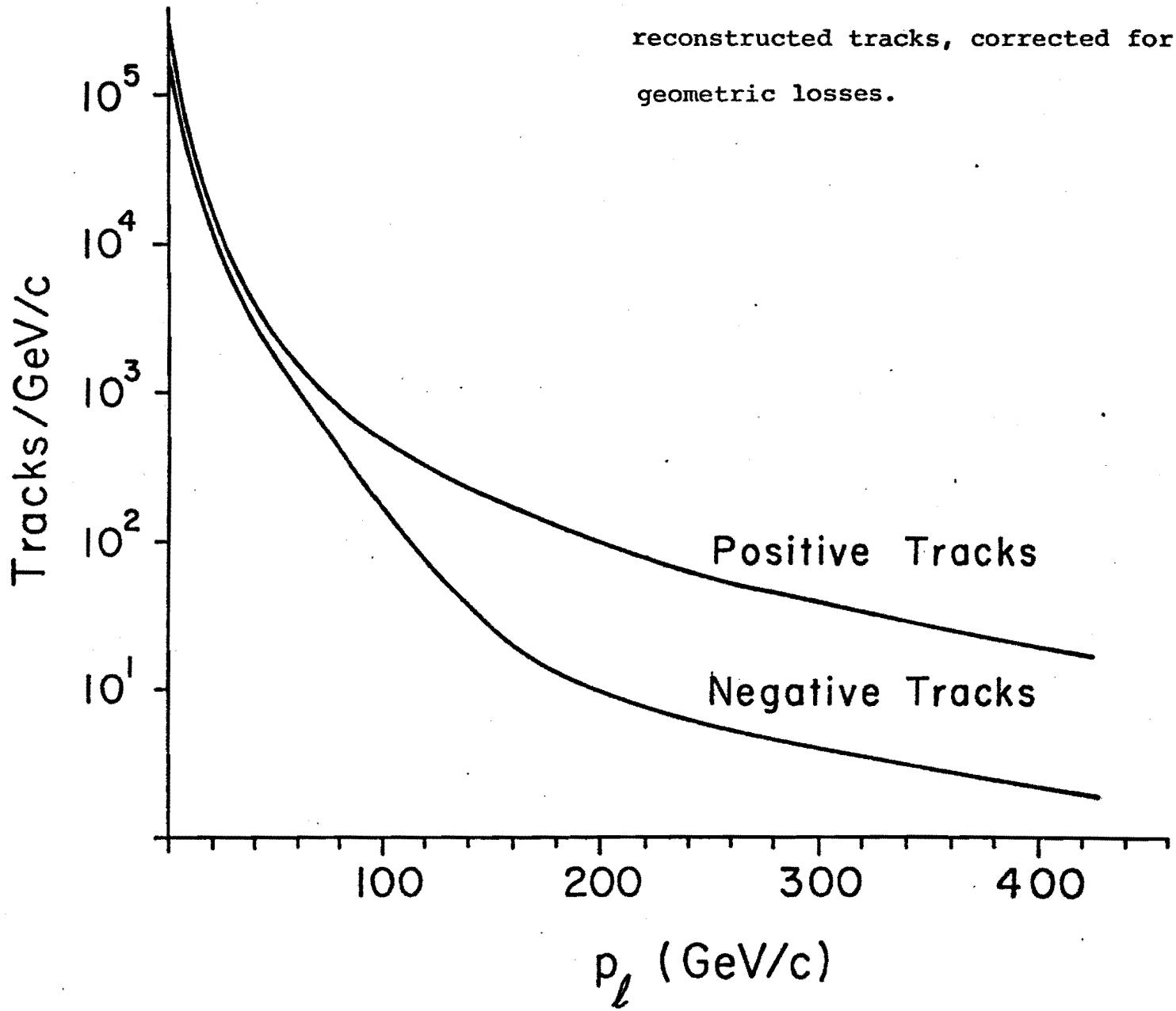

data. Taking advantage of this, we defined a proton sample in the data as being comprised of positive tracks with momenta in excess of 80 GeV/c. Because some of the kinematic variables we will examine are affected by the mass interpretation given to the observed track (e.g. the rapidity), we will study the consequence of changing the mass interpretation when we present the data.

C. WEIGHTING OF EVENTS

The goemetrical arrangement of the apparatus and inefficiency in the operation of the spark chambers precluded our detecting every produced charged particle. In fact, the spark chambers were specifically designed to have a narrow aperture so as to avoid difficulties in reconstructing tracks from multipronged events. (At 300 GeV/c, the topological charged-particle multiplicity in neutron-nucleus collisions is about 15 particles per event.) Inefficiencies and losses in acceptance of events were compensated for by calculating the probability of observing any given event and using the inverse of that probability as a weight in obtaining the production cross sections. Our weighting procedures are described below.

1. Geometric Losses

The active portion of each of the spark chambers was shaped in the form of a narrow slot and centered on the beam axis. On the average, 1-2 charged tracks per event traversed the chambers. Consequently, there was little ambiguity in correlating tracks from different views (X, U, and V coordinates) for reconstructing their trajectories in three dimensions.

To correct for geometric losses of tracks which did not pass through the spark chambers, we proceeded as follows. Assuming that neither the beam nor the target was polarized (a very good approximation), the produced-particle spectrum could not have been a function of the azimuth angle (ϕ) about the beam axis. Therefore, any track observed within our (restricted) azimuthal acceptance represented a class of events with that particle's specific values of transverse momentum (p_T) and longitudinal momentum (p_ℓ), and a uniform distribution in ϕ (including those values not in our acceptance). A typical track from target to L-counter, is shown in Fig. III.9. Its corresponding class of events would intersect the plane of the counter on the circle. The probability of detecting events of this particular class is defined by the ratio of the observed part of the circumference (the solid arcs) to the full circumference. The situation was actually somewhat more complicated than illustrated in the figure, because of the

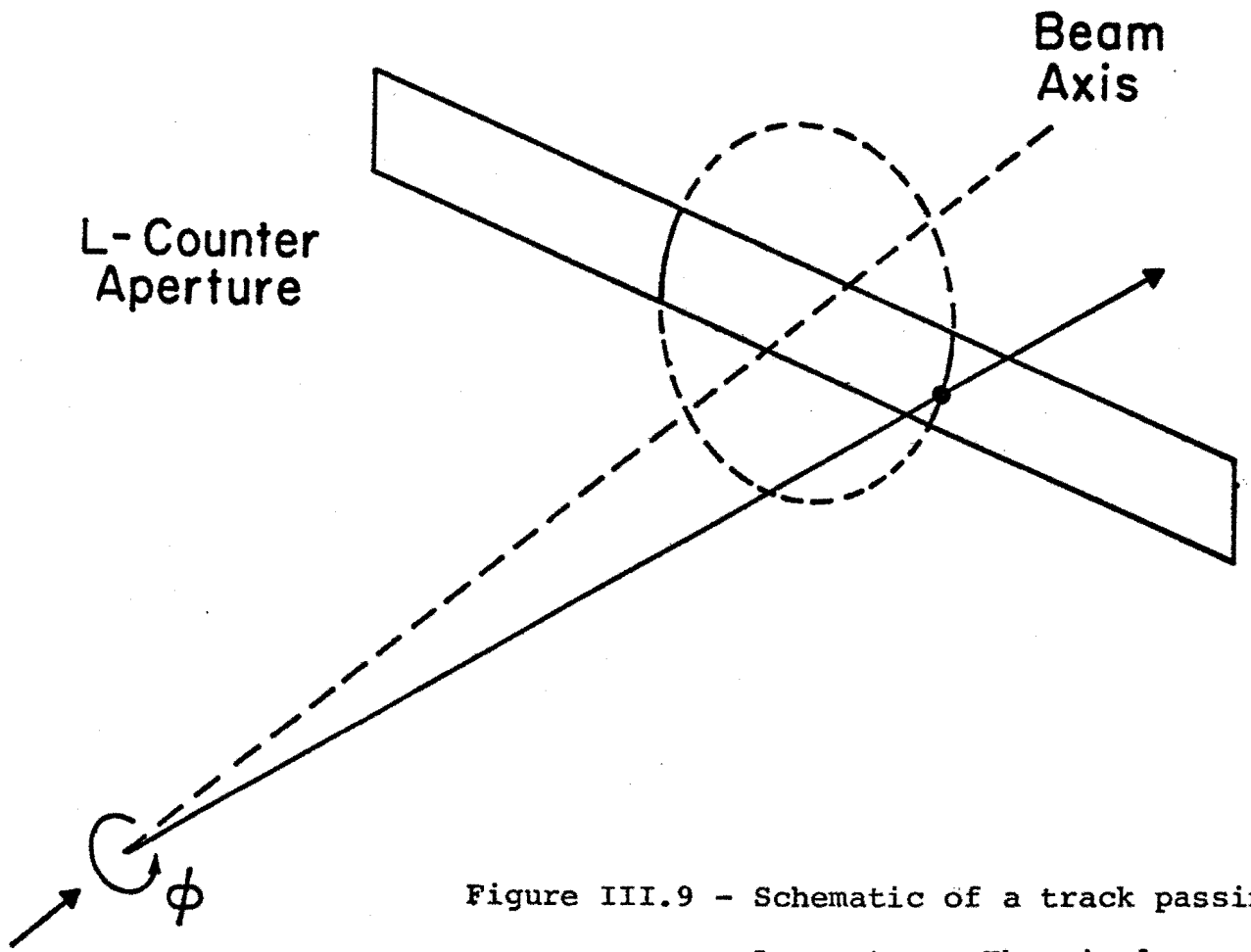

Figure III.9 - Schematic of a track passing through the L-counter. The circle represents the family of intersection points when the track is rotated about the beam axis.

presence of the analyzing magnet. In reality, the charged tracks are bent within the magnet, and consequently the circle defining any particular class of events was displaced horizontally relative to the beam axis. The amount of this displacement was related to the values of p_T and p_ℓ for that particular class of tracks. If the displacement was large enough, tracks in that class of events could be observed for production on only one side of beam center and not on the other (true for particles having small momenta and therefore large bends in the magnet). These events posed no difficulty, except that they had a larger weight (a factor of two more).

There were, of course, events for which our acceptance was zero; these were particles produced at large angles or at very low momenta. Such events are lost and cannot be corrected for in our experiment. In Fig. III.10 we show the lower limits of the acceptance of the apparatus in p_ℓ and y as functions of p_T. (The rapidity is defined as:

$$y = \frac{1}{2} \ln[(E + p_\ell)/(E - p_\ell)],$$

where E is the energy of the particle and p_ℓ its longitudinal momentum.) The two curves in the figure represent, for each value of p_T, the minimum values of p_ℓ and y for

Figure III.10 - Minimum values of longitudinal momentum (part a) and rapidity (part b) for which tracks can be accepted by the spectrometer, as a function of transverse momentum. A pion mass was assumed in the calculations for part b.

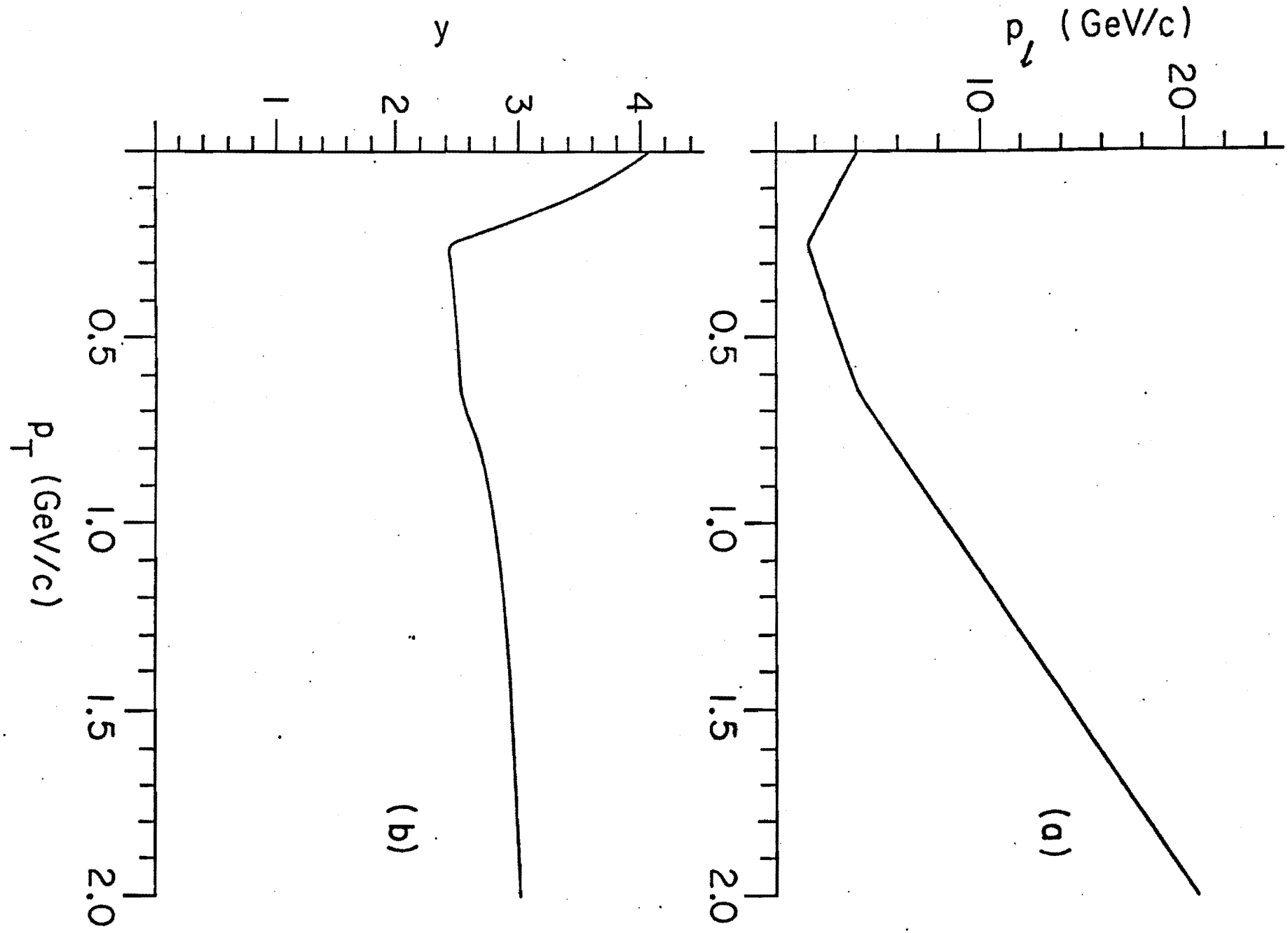

tracks which are inside the acceptance (i.e., tracks with values above either curve were accepted). We see that for a typical incident momentum of 300 GeV/c, our acceptance encompasses essentially the full range of the forward part of the center of mass. (A pion at rest in the center of mass should have a value of $y = 3.23$ for such an incident momentum)

2. Efficiency of the Spectrometer

Momentum vectors characterizing the observed final state of each event were reconstructed from the spark coordinates in the spark chambers. The accuracy of these momentum vectors and the efficiency of the spectrometer were limited both by characteristics of the spark chambers and by the methodology in reconstructing the track from available information.

Track reconstruction was accomplished by finding all sets of three or four colinear sparks in the four X (horizontal) wire planes, and then requiring that colinear points in Y (vertical) be obtained from at least three of the rotated planes (U and V) when matched with the line found in the X planes. The colinearity requirement allowed ±1 mm spark deviations from a straight line in the X planes (±3 mm for V and U). The resulting distribution of sparks around the fitted tracks had a half

width at half maximum of about .2 mm (.8 mm for the rotated planes).

We determined the efficiency of the spectrometer by taking advantage of the expected azimuthal symmetry of particle production about the beam direction (or Z axis). Referring to Fig. III.9, the circle of rotation traced by the intersection of the track with the plane of the L-counter has two arcs which are within the acceptance of the spectrometer. Except for statistical fluctuations, the number of produced tracks, having any specific configuration of p_T, p_ℓ and charge, must be identical for both of the arcs. Thus, comparing the numbers of tracks actually observed provides an estimate of the spectrometer's relative track detection efficiency in the regions of the two arcs. Because the radius of the circle of rotation depends on the polar production angle ($\tan\theta = p_T/p_\ell$), and since the position of the center of the circle varies with the momentum of the particle (the bend of the trajectory in the magnet is, for simplicity, not shown in Fig. III.9), relative detection efficiencies were, in fact, able to be obtained for any two arbitrary points along L counter. Average efficiencies as a function of X were determined from these two-point comparisons, as described below.

Defining N = 110 intervals of position along the

L-counter (X), we formed a two dimensional array A_{ij} of the number of observed tracks which traversed the ith interval along the L-counter and which would have traversed the jth interval if the production vector were rotated 180° in azimuth. (Tracks having p_T and p_ℓ combination which, when rotated, lied outside the acceptance were not used in this analysis.) Defining ε_i as the inverse of the efficiency for the ith interval (i.e., n_i of the $n_i \cdot \varepsilon_i$ tracks were observed to traverse that interval of the L counter) we set up the following system of N linear equations in N unknowns, equating the sum of all tracks which intersected the ith interval to the sum of all tracks which could intersect the ith interval after a 180° rotation:

$$\sum_{j=1}^{N} A_{ji}\varepsilon_j = \sum_{j=1}^{N} A_{ij}\varepsilon_i = \varepsilon_i \sum_{j=1}^{N} A_{ij} \qquad (i = 1,N).$$

Because the overall normalization cannot be obtained from just relative efficiencies, the above corresponds to only N-1 independent equations. We solved the set of equations for the ε_i and smoothed the results because of statistical fluctuations between neighboring bins.

The absolute normalization of the ε_i was fixed using a second independent spectrometer, which consisted of large-acceptance wire spark chambers placed in front of,

between, and behind the narrow chambers.[16] Only a small sample of events were reconstructed using both spectrometers, consequently the acceptance was determined to adequate statistical accuracy only at the center of the spectrometers; this, however, was sufficient to fix the normalization of the narrow chambers. Through examining tracks found in the large spectrometer, we found that the upstream module of narrow spark chambers was uniformly efficient across its entire aperture, and that the efficiency of the downstream module did not vary in the vertical dimension. This confirmed that our characterization of the spectrometer efficiency by a function of a single variable, namely X, was adequate.

The overall results of the efficiency analysis are shown in Fig. III.11. The relative accuracy of the fitted values ranges from 10% near the edges of the chamber and in the central dip region, to about 3% just outside the central dip. The unusual shape of the efficiency function can be partially understood by examining the construction of the two modules of spark chambers. The upstream module had lucite frames with only thin mylar windows to inhibit the passage of particles through it. Because of its large size (and materials available), the downstream chamber had styrofoam-lucite sandwiches for both frames and windows. While this did not appreciably

Figure III.11 - Overall reconstruction efficiency as a function of position at the L-counter, as determined by a comparison of symmetric tracks.

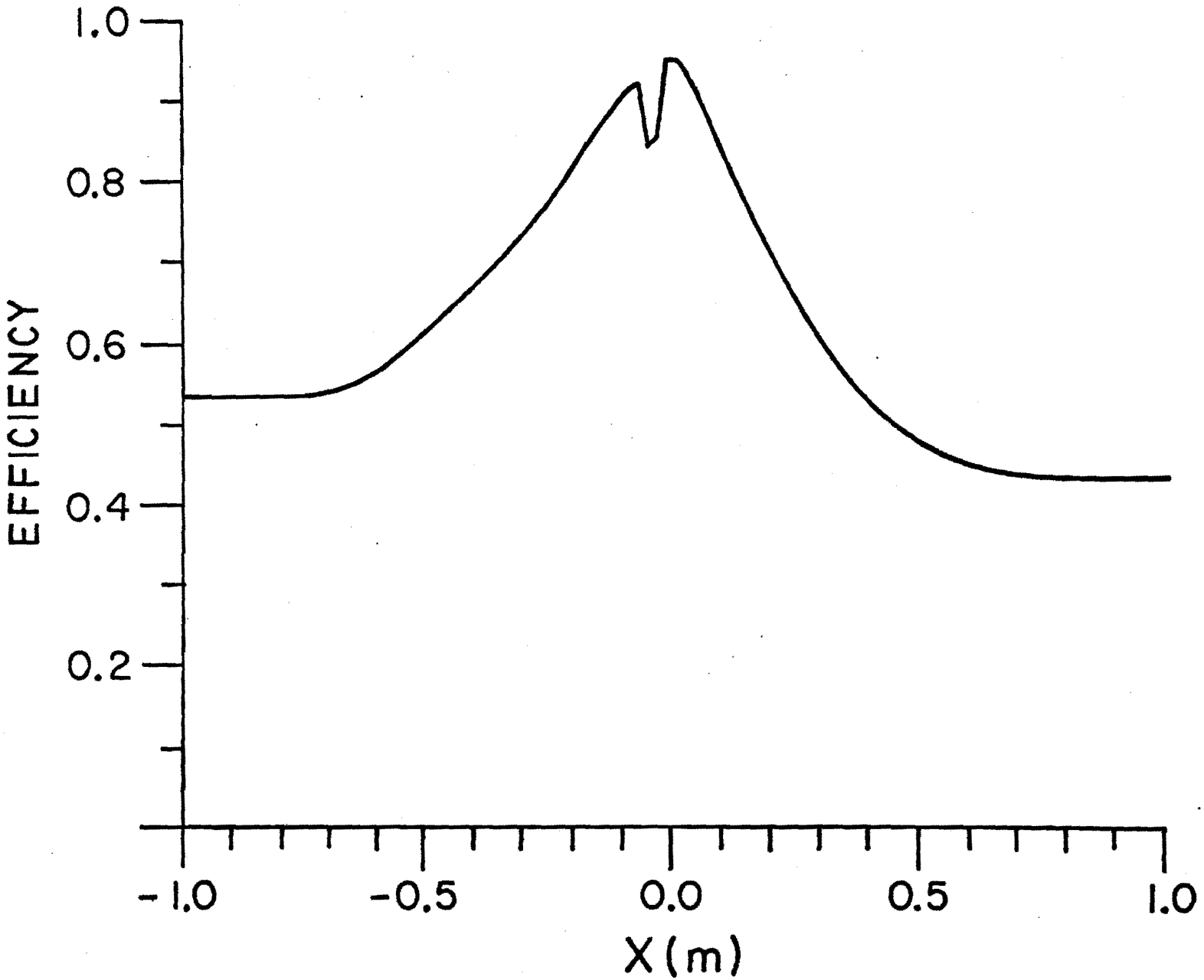

affect the passage of particles through the chambers, it was nevertheless desirable to further reduce the amount of material in the path of the neutron beam; we therefore removed 2-inch diameter pieces of the styrofoam-lucite windows in the downstream module and replaced them with thin mylar. This difference in the kind of material and in the chamber construction could affect the field structure and possibly explain the deterioration in sensitivity in the center of the chamber. It is less clear what caused the inefficiency at the outer edges of the acceptance. It is possible that propagation of the high voltage pulse to those extreme points was not effective; this is because the pulse was carried along a conductive epoxy and copper tape sandwich. Also, the downstream module was less gas-tight, so the gaps between wire planes may have been contaminated by oxygen and therefore less efficient (leaks could have occurred at the edges).

3. Experimental Sensitivity

The two preceding subsections dealt with the event-weighting criteria. In addition to corrections for geometry and reconstruction efficiency, we imposed several cuts on the data which we also took into account in the extraction of cross sections. The electron cuts (Chapter III.B.2) required that we eliminate those tracks with $p_\ell \leq 25$ GeV/c which either traversed the gap in the

lead radiator or produced a large signal in the L-counter. To correct for the loss of hadrons resulting from the imposition of these criteria, the weights for accepted tracks with $p_\ell \lesssim 25$ were increased by an additional multiplicative factor of 1.12 ($\sim 1/(1-.11)$, to account for $\sim$11% losses); also, when an azimuthally rotated track fell in the gap between the lead radiators, the weight for the track was increases by a factor of 2.

In Fig. III.12 we show the inverse of the weights assigned to tracks, averaged over all observed tracks and plotted as a function of p_T, p_ℓ, and y. Part a) shows the efficiency versus transverse momentum for four regions of longitudinal momentum. The dips near $p_T \simeq 0.4$ GeV/c arise from the elimination of tracks with momenta below 25 GeV/c that traverse the gap in the lead radiator. Part b) of the figure displays the average efficiency plotted against p_ℓ for four regions in p_T. In part c) we show the average inverse weight as a function of rapidity. The rapidity is closely related to the polar production angle θ in the laboratory:

$$y_{lab} \simeq -\ln[\tan \theta/2].$$

The miniscule efficiency at small rapidity arises from the fact that such tracks are produced typically at large angles and hence are not readily detected in the apparatus.

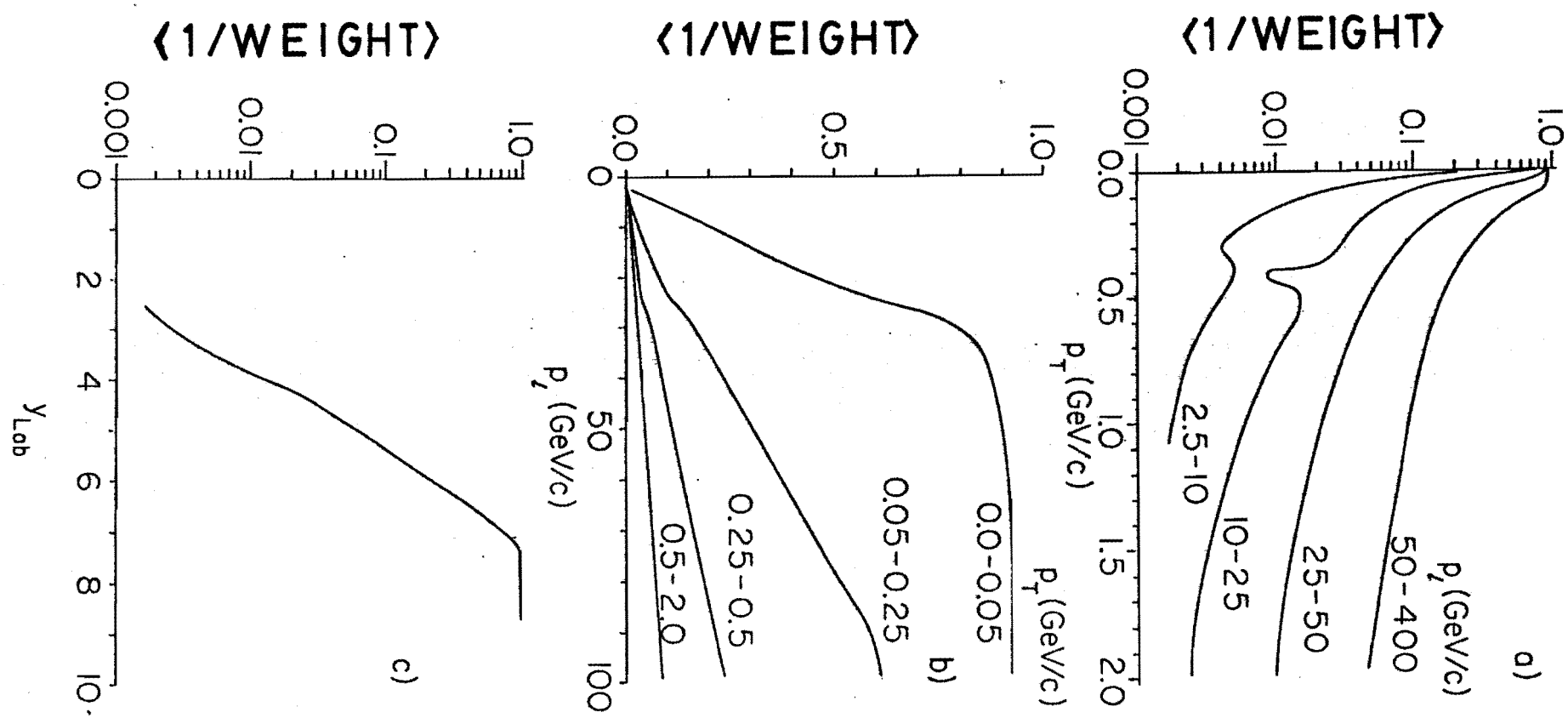

Figure III.12 - The efficiency of the spectrometer, deduced from the average of the inverse of the weights for all tracks observed, shown as a function of several variables of interest.

The only seriously localized inefficiency in a kinematic variable is, as suggested previously, in the p_T distribution near $p_T \sim 0.4$ GeV/c, for $p_\ell \leq 25$ GeV/c. In Fig. III.13 we plot, as a function of p_T, the fraction of tracks with $p_\ell \leq 25$ GeV/c eliminated because of the cut on the data involving the gap in the lead radiator; the total fraction of data eliminated by this cut was about 9%. Although the effect appears to be dramatic in Fig. III.12a, the only consequency of this inefficiency on our results is a 10% reduction in statistical accuracy of our data for that region of phase space; thus the error bars on quantities near $p_T = 0.4$ are somewhat larger than those at other values of p_T.

D. CONVERSION OF DATA TO CROSS SECTIONS

Cross sections are determined by counting the number of occurrences of some event per incident particle per scattering center, where an event can be an outcome of interest (e.g., all interactions, a charged particle in some particular region of phase space, or a certain exclusive channel, say $n\,A \rightarrow A\,\pi^-\pi^-\pi^+p$). The number of scattering sites per unit area of a target is:

$$d = \rho \ell N_o/A$$

Figure III.13 - Differential fraction of events which traversed the gap in the lead radiator plotted as a function of p_T.

where ρ is the density of the target, ℓ is its thickness, N_o is Avagadro's number, and A is the gram atomic weight. Using this definition of d, the cross section represented by the observation of any one specific type of event during a data run can be written as:

$$\sigma_{ev} = \frac{1}{Nd} \cdot f$$

where N is the number of calorimeter counts for the data run, and f is the ratio of calorimeter counts to neutrons on target. The value of f is the major normalization correction, and can be calculated from:

$$f = 1 - \frac{(1-e^{-\delta})\beta}{1-(1-\beta)(1-e^{-\delta})} \simeq .74$$

where δ is the number of absorption lengths of material in the beam between the beginning of the target and the calorimeter, and β is the (average) portion of the inelastic cross section which will not register in the calorimeter. [See Chapter III.A.2, and the Appendix.] The net number of events attributable to interactions with the nuclear target is the difference between the (normalized) target-in and target-out runs; and the cross section for such events is the cross section per observation multiplied by the net number of observations.

CHAPTER IV

RESULTS

In this chapter we present the results of our experiment in the form of multiplicity distributions. The multiplicity is defined as the observed cross section for the process under consideration divided by the total inelastic cross section (i.e., the average number of times per collision any particular end-state is produced). Specifically, we use the following approximate expression for the total inelastic cross section[17]:

$$\sigma^{A}_{INEL} = 46\ A^{0.69}\ \text{mb},$$

where A is the gram-atomic weight of the nuclear target (1 mb = 10^{-27} cm^2). We extracted the A-dependence for any region of phase space by fitting the five nuclear cross sections to a function of the form const$\cdot A^{\alpha}$. A value of α=0.69 would indicate that the multiplicity is independent of nuclear size; in other words, after the initial collision, the rest of the nucleus would be transparent to the produced state, something which which would not be expected for hadrons.

In the following sections we examine the dependence of the data on transverse momentum (p_T), radidity (y), pseudo-rapidity (η), longitudinal momentum, and combinations of these variables. Statistical errors are included in

the figures, and the non-statistical biases are discussed.

A. DEPENDENCE ON TRANSVERSE MOMENTUM

In Fig. IV.1 we show the produced-particle multiplicity integrated over $y>4$ as a function of p_T^2 for each of the target nuclei. The positive particles are examined in three ways: First, all the data are given without differentiation according to longitudinal momentum, and then the positives are separated into 'pions' and 'protons' using our division at p_ℓ = 80 GeV/c (tracks with longitudinal momenta above this value are interpreted as protons). The pion distributions are all steeply falling for $p_T^2 \leq 0.3$ (GeV/c)^2, with the approximate functional form of $\exp(-8\ p_T^2)$. The proton data can be represented by an exponential function of p_T^2 of the form $\exp(-1.5\ p_T^2)$ over the entire range $0 \lesssim p_T^2 \lesssim 2$. Although the p_T^2 distributions for all particles become less steep with increasing longitudinal momentum, the positive spectra exhibit a substantially weaker p_T^2 dependence than the negative-particle spectra. We attribute this difference partially to the presence of the proton component in the data. The difference is particularly pronounced at larger p_T^2 where the remnant proton component, even for $p_\ell \lesssim 80$ GeV/c, could be substantial.

The dependence of the p_T^2 distributions on nuclear size is shown in Fig. IV.2, where we plot α as a function

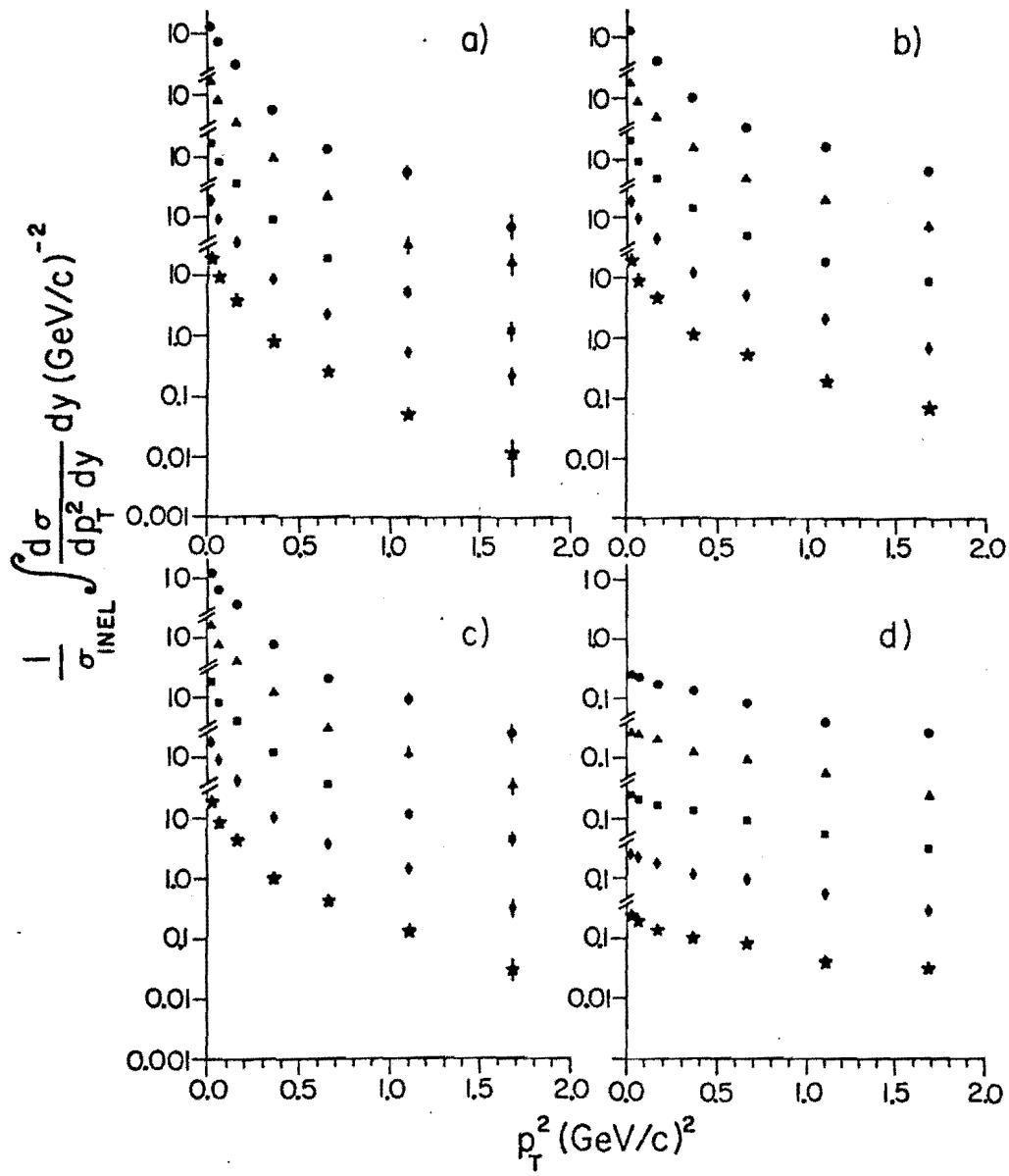

Figure IV.1 -

Multiplicity as a function of the square of the transverse momentum, for rapidities greater than 4.0. a) All negative particles; b) all positive particles; c) positive 'pions' (longitudinal momentum less than 80 GeV/c); d) 'protons' (p_ℓ>80 GeV/c). In each graph, the five types of nuclear targets are denoted by the following symbols: Be-●; Al-▲; Cu-■; Sn-♦; Pb-★.

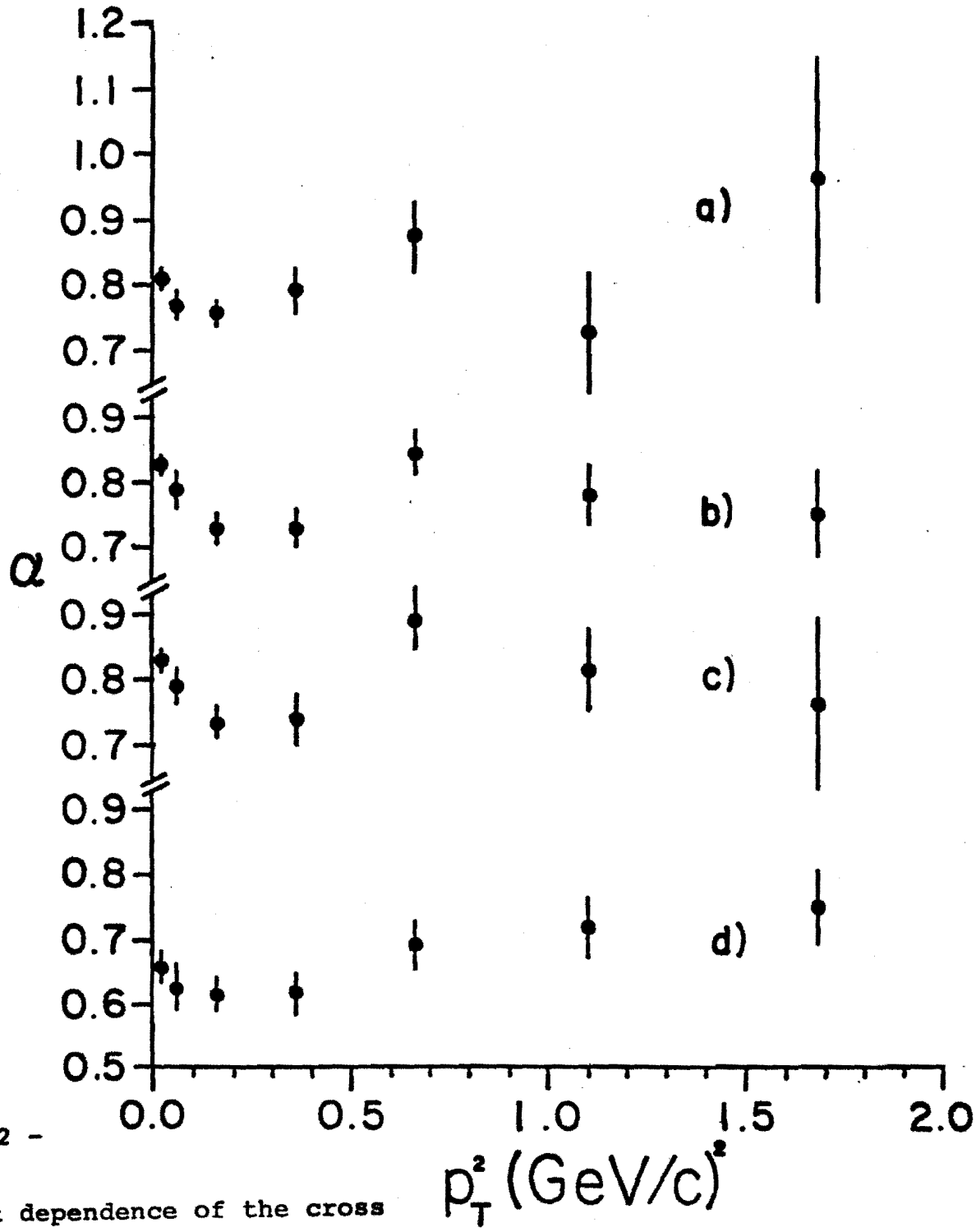

Figure IV.2 - Atomic-weight dependence of the cross sections as a function of the square of the transverse momentum for rapidities greater than 4.0. a) All negative particles; b) all positive particles; c) positive 'pions'; d) 'protons'.

of p_T^2 for the cross section data illustrated in the previous figure. The graph for negative particles shows a peak for α at small p_T^2, followed by a fall-off and a constant region at larger values of p_T^2. The graph for positive particles shows similar behavior; when we split this data into the 'pion' and 'proton' components, we see that the small-p_T^2 peak appears to be caused by the pions. The numerical values of the data points used in Figs. IV.1 and IV.2 are given in Table IV.1, located at the end of this chapter.

B. DEPENDENCE ON LONGITUDINAL MOMENTUM AND RAPIDITY

The atomic-weight dependence of the data on longitudinal momentum is displayed in Fig. IV. 3. The data have been integrated over p_T and the cross sections ($d\sigma/dp_\ell$) fitted to the form A^α. There appears to be a significant A-dependence in the data, particularly at small values of p_ℓ. The positive and negative spectra are very much the same; even where our momentum cut defines the positive particles as protons, the few negative particles exhibit an A-dependence which is only slightly different (statistically non-significant). The numerical values of α, and of the produced multiplicity for the individual nuclear targets, are given as functions of p_ℓ in Table IV.2.

In Fig. IV.4 we display the multiplicity, integrated over p_T^2, as a function of rapidity (y) for all the targets;

Figure IV.3 - Atomic-weight dependence of the cross section as a function of longitudinal momentum. a) All negative particles; b) all positive particles.

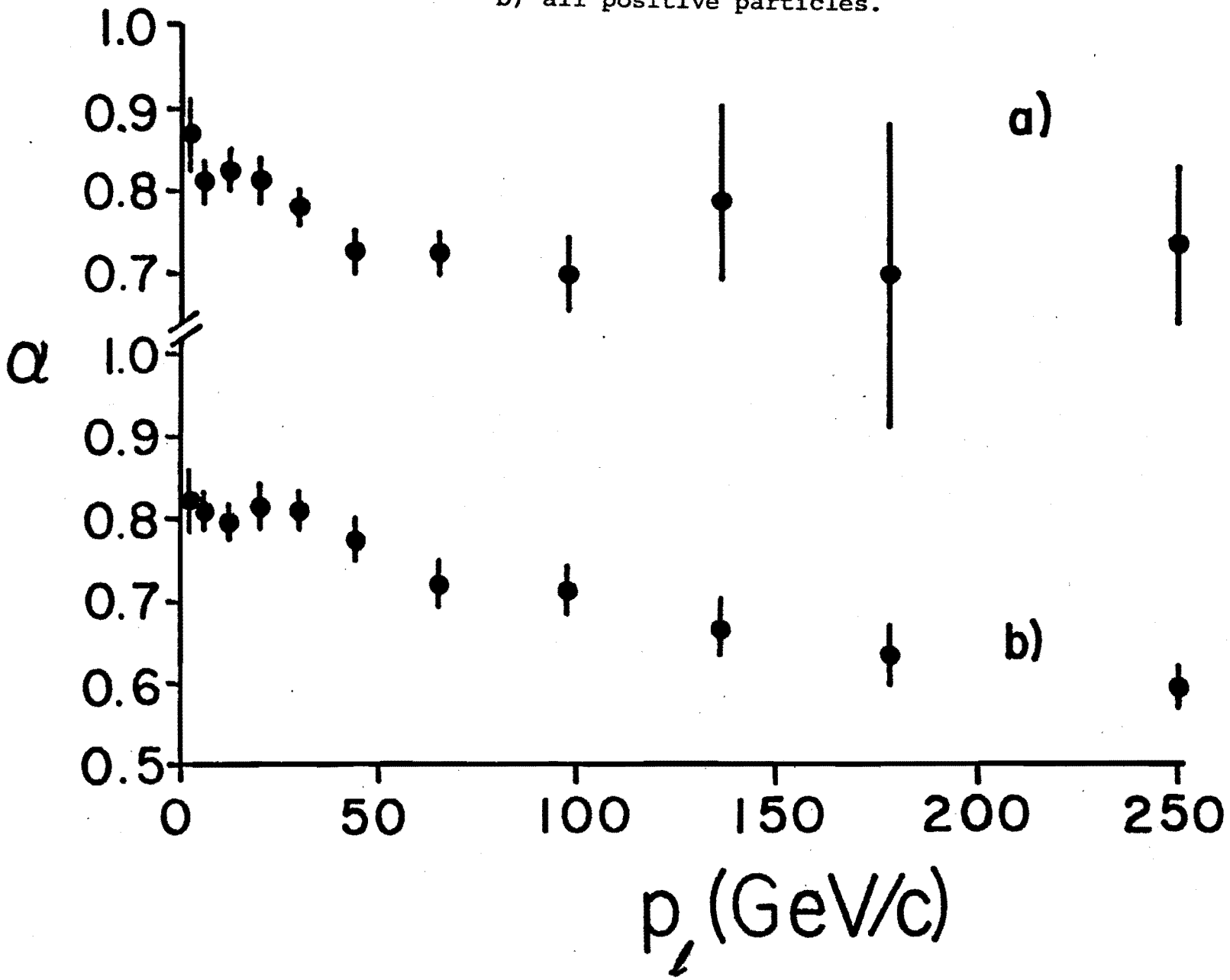

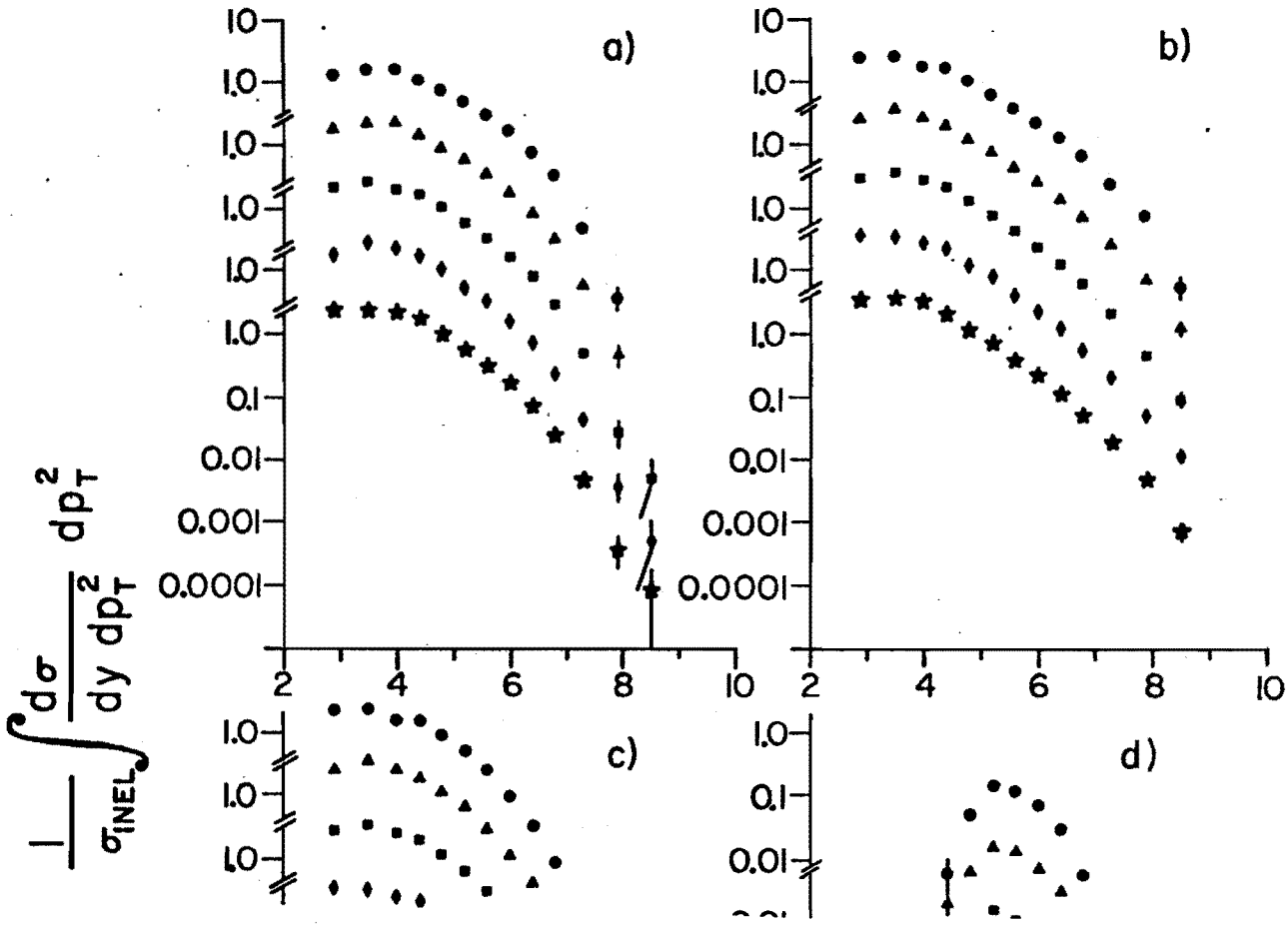
$\frac{1}{\sigma_{INEL}} \int \frac{d\sigma}{dy\, dp_T^2} dp_T^2$
a)
b)
c)
d)
10
1.0
0.1
0.01
0.001
0.0001
2
4
6
8
10

the positive spectra (shown in part b, with a pion mass assumed) are again divided into 'pion' and 'protons' in parts c) and d) respectively. Below $y \approx 4$ our acceptance deteriorates and, consequently, the absolute normalization is not reliable. (The error bars in the figure, as elsewhere in this chapter, are purely statistical in nature). The atomic-weight dependence of the distributions in Fig. IV.4 is shown in Fig. IV.5, where we plot α as a function of rapidity. Both positive and negative-pion spectra fall with increasing y, the value of α for negative pions decreasing below 0.69 for $y \gtrsim 7$, whereas the protons (the rapidity calculated with the proton mass) show a marked decrease to $\alpha = 0.5$ in the forward direction. The values depicted in Figs. IV. 4 and IV.5 are tabulated in Table IV.3 at the end of this chapter.

C. CORRELATIONS BETWEEN y AND p_T

We now proceed to a more detailed examination of the A-dependence of the data. In Fig. IV. 6 we show the p_T^2 dependence of the α-parameter for three different regions of rapidity (calculated using the <u>pion</u> mass): $4<y<5$; $5<y<6$; $6<y<8$. The variation of α with p_T^2 appears to depend on y. In particular, the negative particles show a peak in the α distribution at small p_T^2 only for the lowest region in rapidity. The positive spectrum, on the other

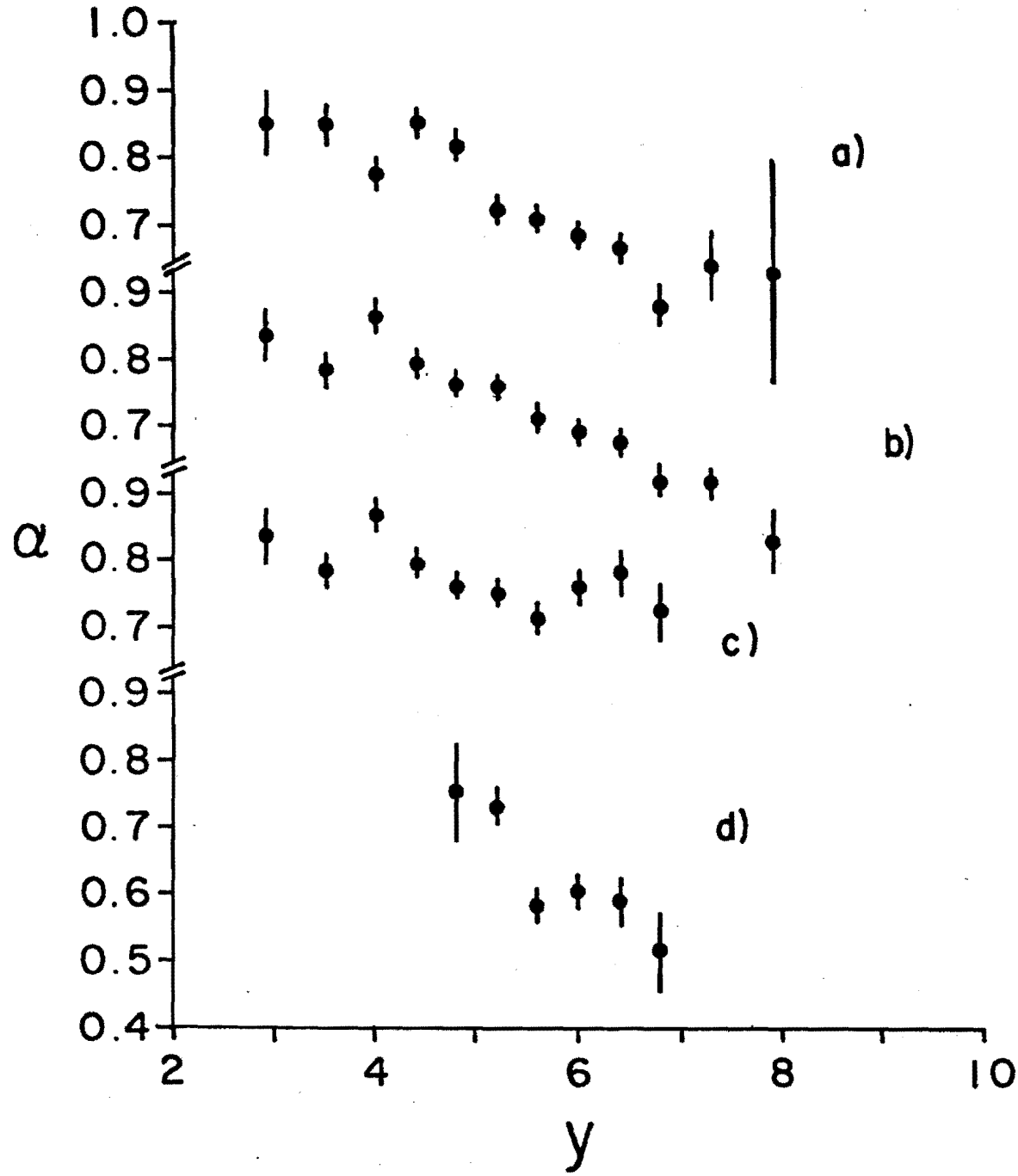

Figure IV.5 - Atomic-weight dependence of the cross section as a function of rapidity. a) All negative particles; b) all positive particles (pion mass assumed); c) positive 'pions'; d) 'protons'.

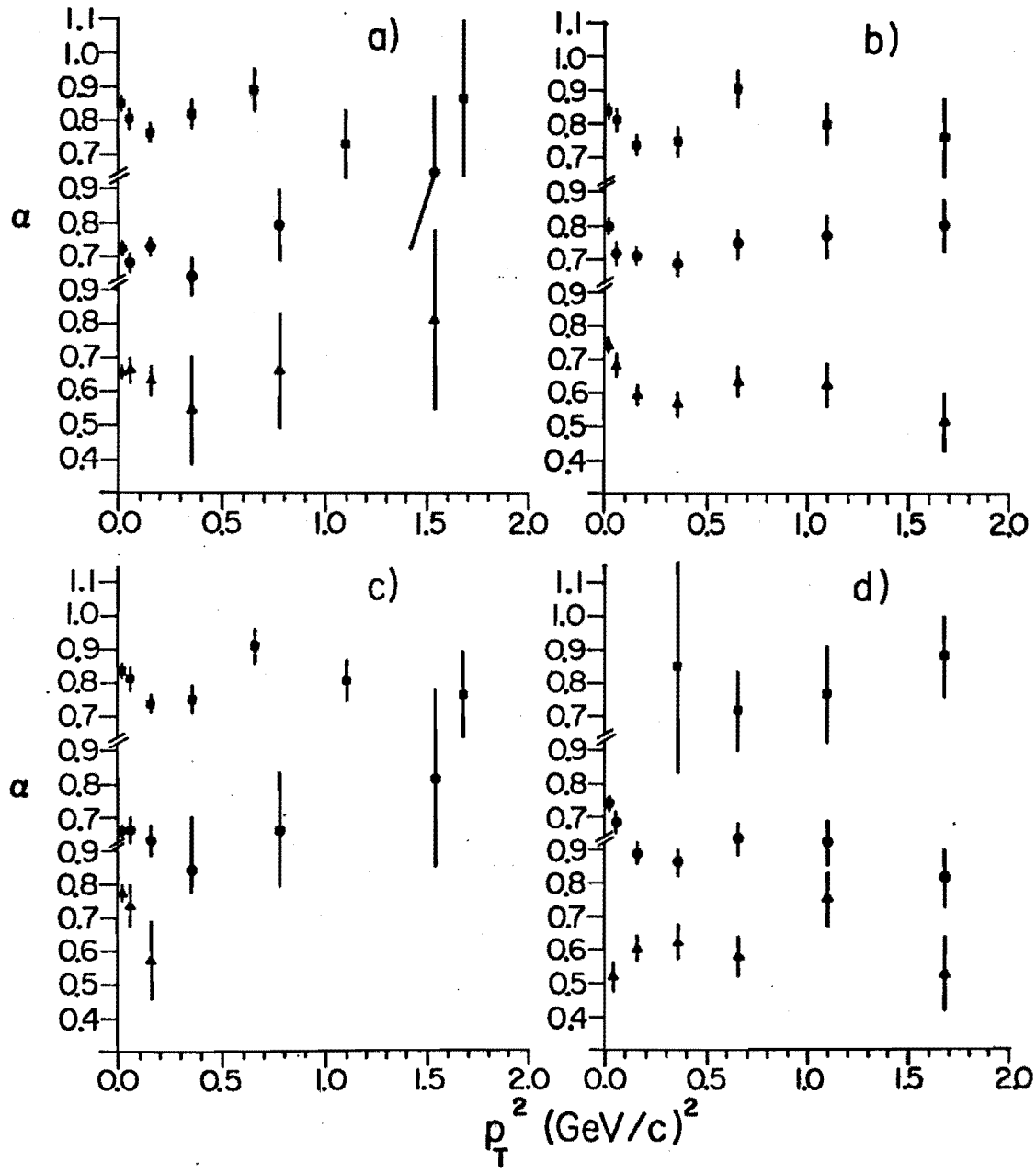

Figure IV.6 - Atomic-weight dependence of the cross section as functions of the square of the transverse momentum for different regions of rapidity. ■ 4 < y < 5; ● 5 < y < 6; ▲ 6 < y < 8. a) All negative particles; b) all positive particles (assuming pion mass); c) positive 'pions'; d) 'protons'.

hand, exhibits a similar peak for all y; even though this effect appears to be caused by 'pions', our crude pion-proton separation prevents us from reaching any definitive conclusions. Table IV.4 shows the values used in this figure, along with the associated values of the multiplicities from the different targets.

For completeness, we present in Table IV.5 the multiplicities and the fitted values of α as functions of p_T^2 (for $y>4$) separated into regions of longitudinal momentum.

D. COMPARISON OF DEPENDENCE ON RAPIDITY AND PSEUDO-RAPIDITY

The difference between rapidity (y) and pseudo-rapidity (η) is not large in most regions of phase space, and so the two are usually used interchangeably. At very small angles, however, the differences can be substantial.

The definition of rapidity, as measured in the laboratory frame-of-reference is:

$$y = -\frac{1}{2}\ln[(E-p_\ell)/(E+p_\ell)]$$

$$= -\ln[\tan(\psi/2)],$$

where E is the energy and p_ℓ is the longitudinal momentum of the particle in the laboratory; ψ is an 'angle' defined by $\tan\psi = p_\ell/E$. The definition of pseudo-rapidity is:

$$\eta = -\ln[\tan(\theta/2)],$$

where θ is the production angle of the particle in the laboratory frame (i.e., $\tan\theta = p_T/p_\ell$). The two angles ψ and θ in these definitions are approximately the same only at large p_T, that is, where the mass of the produced particle can be ignored relative to its transverse momentum.

In Fig. IV.7 we compare y and η distributions for negative tracks produced on a Beryllium target. The multiplicity for regions of large rapidity is smaller than that for the same numerical values of η. This effect can arise because different regions of phase space are examined for the same value of y and η. Figure IV.8 shows (assuming a pion mass) lines of constant rapidity and pseudo-rapidity in (p_T, p_ℓ) space; as might be expected, the difference between the two variables is quite pronounced at small p_T.

The atomic-weight dependence as a function of pseudo-rapidity is shown in Fig. IV.9, and should be compared to Fig. IV.5 (which shows the dependence on rapidity). The difference in the α-parameter is readily apparent at large values of the two variables; although the value of α falls off as both y and η increase, α is smaller using the y variable than using η. (Also, there is an absolute kinematic upper limit for y but not for η.) For $\eta \gtrsim 7$, the extracted values of α rise above the minimum value of $\alpha = 0.7$ reached for $\eta \approx 7$. To explore this effect further,

Figure IV.7 - Comparison between rapidity (o) and pseudo-rapidity (●). Multiplicity as a function of the two variables are plotted on the same axis for negative particles from a beryllium target.

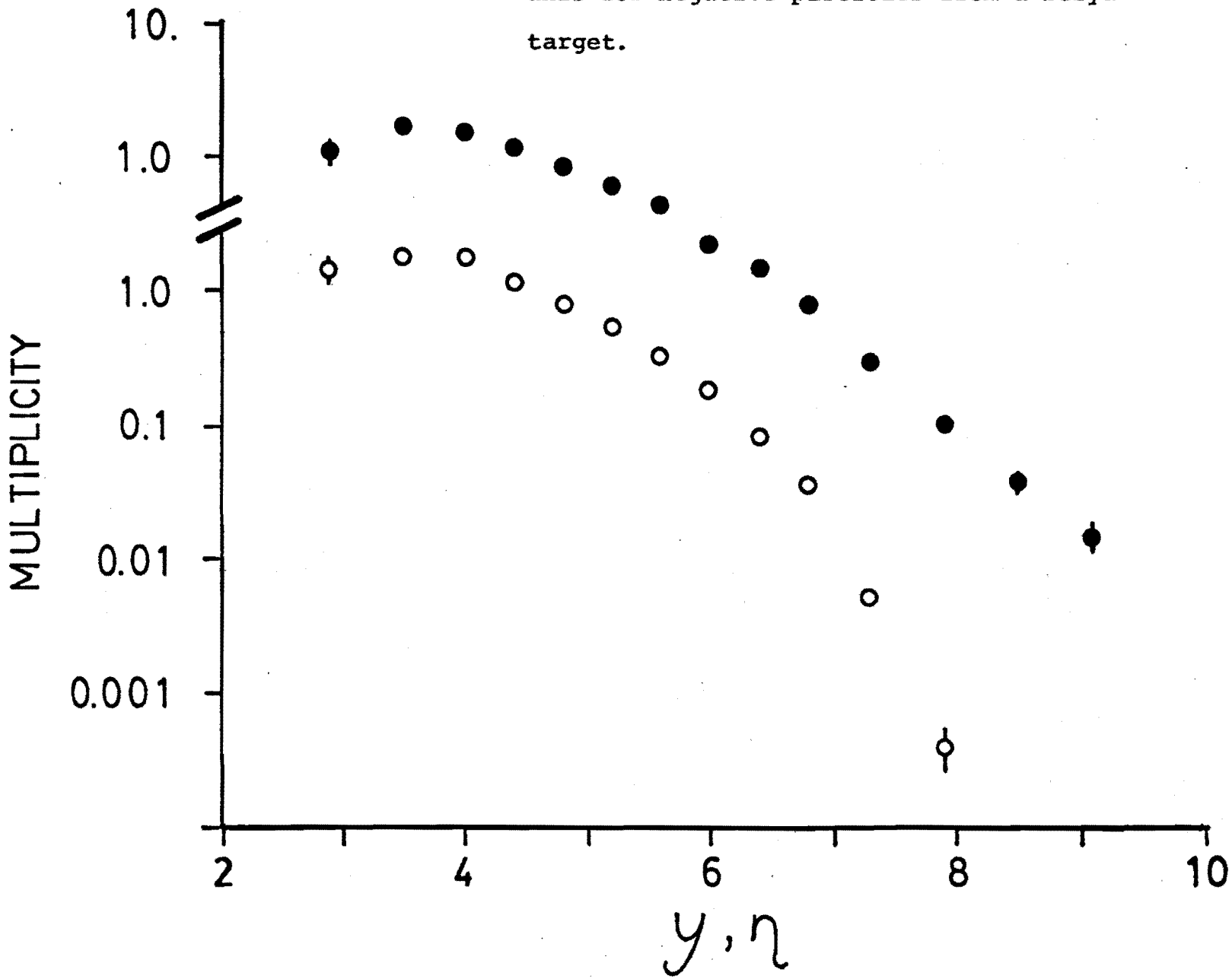

and pseudo-rapidity (solid) shown in momentum space.

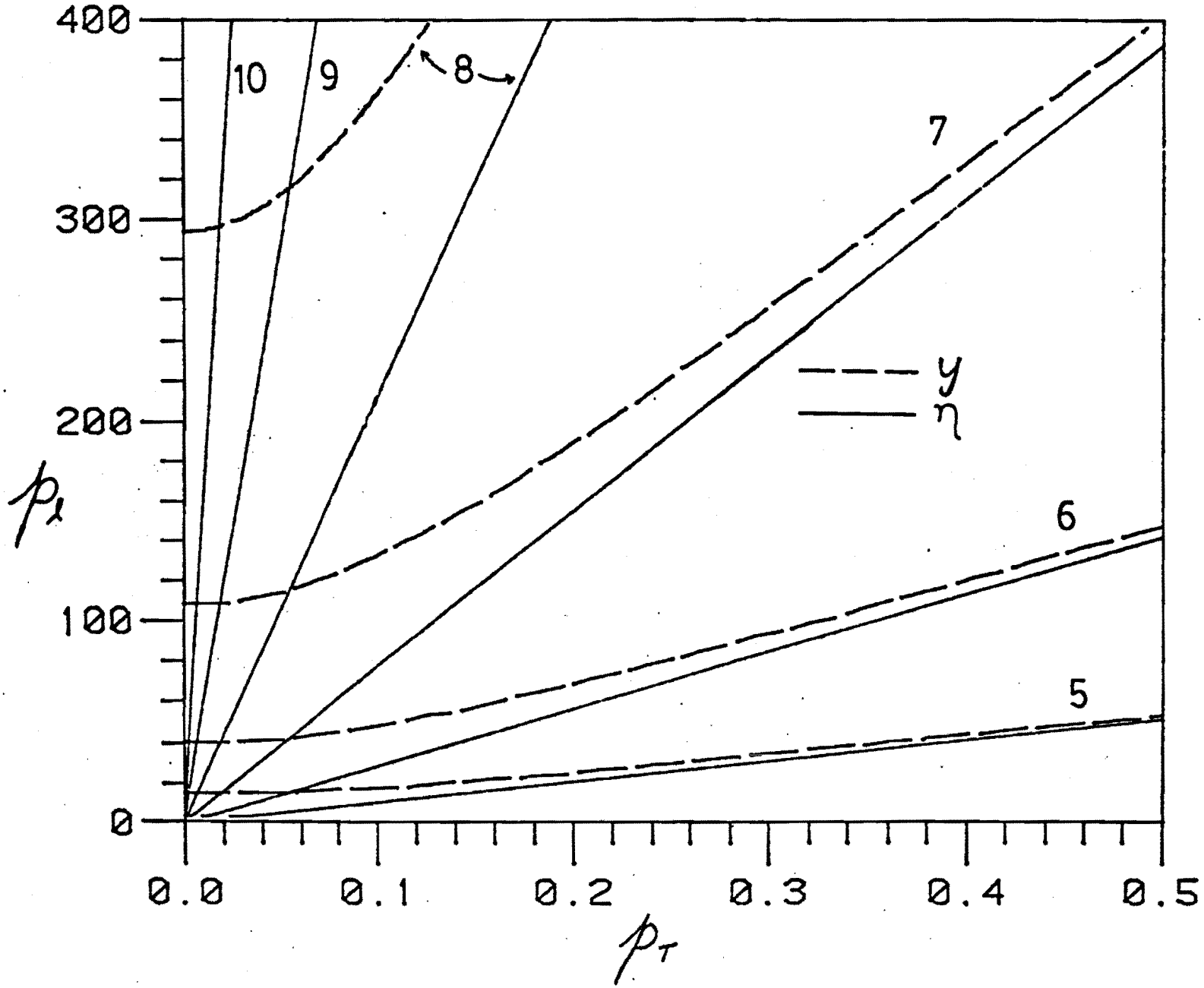

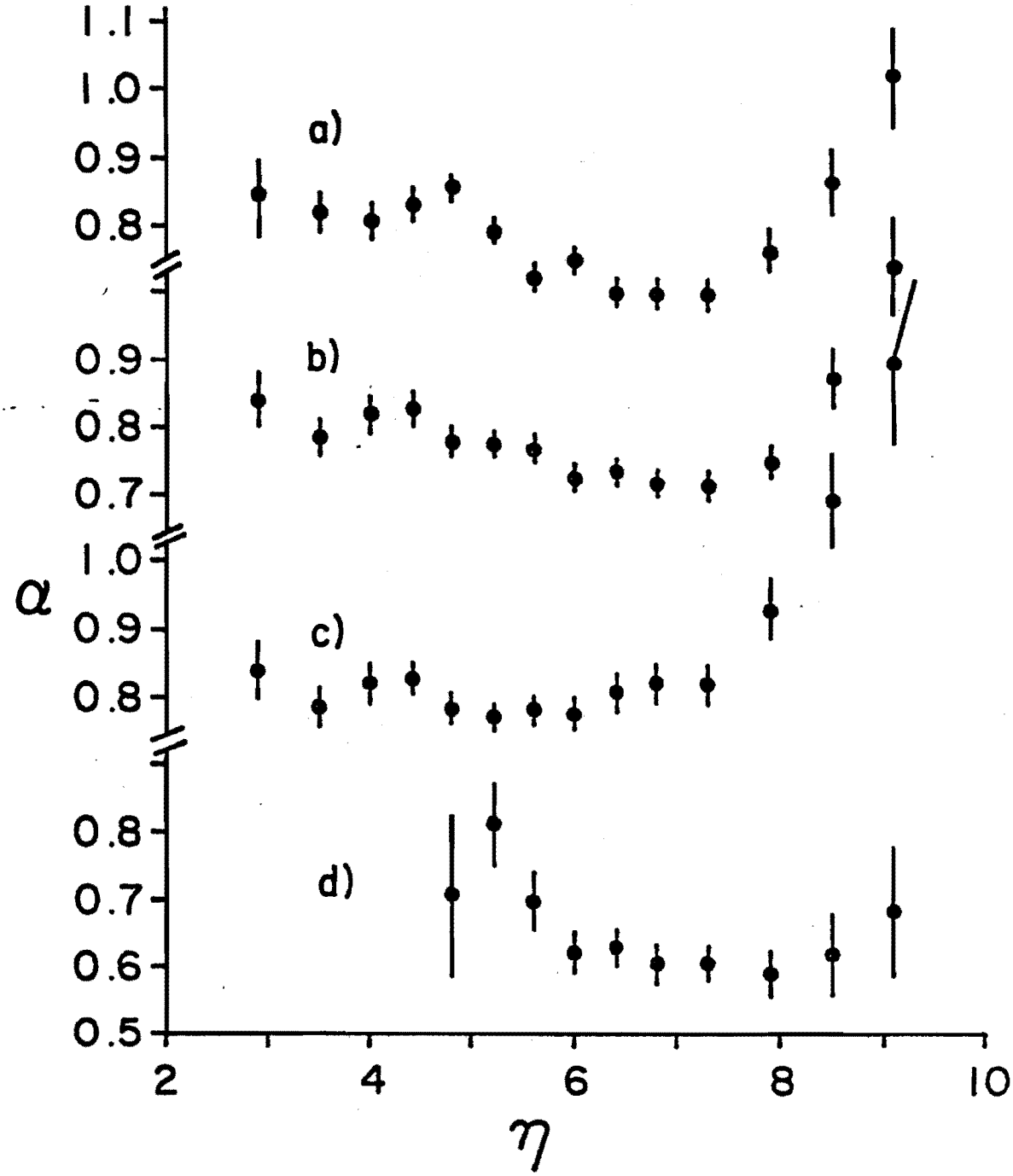

Figure IV.9 - Atomic-weight dependence as a function of pseudo-rapidity. a) All negative particles; b) all positive particles; c) positive 'pions'; d) 'protons'.

in Fig. IV.10 we show the α-parameter as a function of y and η, but with the data divided into different regions of p_ℓ. The rise in α at large η is observed for all p_ℓ; however, it is most pronounced for both positive and negative tracks in the $20 < p_\ell < 60$ GeV/c interval where we have the best statistics for large values of η (i.e., more events occur there, so the statistical errors are smaller). The data at large y have poor statistics, and we consequently cannot speak to a rise in α for large y. Tables IV.6 - IV.8 give the values of the multiplicities for the nuclear targets and the α-parameters for the above y-η comparison.

E. SYSTEMATIC ERRORS

Cross sections (or multiplicities) reported in this thesis have several sources of possible systematic uncertainty. The error bars shown in figures and in the tables thus far include only the statistical sources of error (arising from the limited number of events). Systematic biases stem from the uncertainty in the measurement of the neutron flux (see Chapter III), from variations in and thickness-measurement errors for the nuclear targets, from residual contamination of the data (by electrons, kaons, stray tracks, etc), from the idealized treatment of the apparatus in correcting for geometric losses, and from uncertainties in the determination of the efficiency of

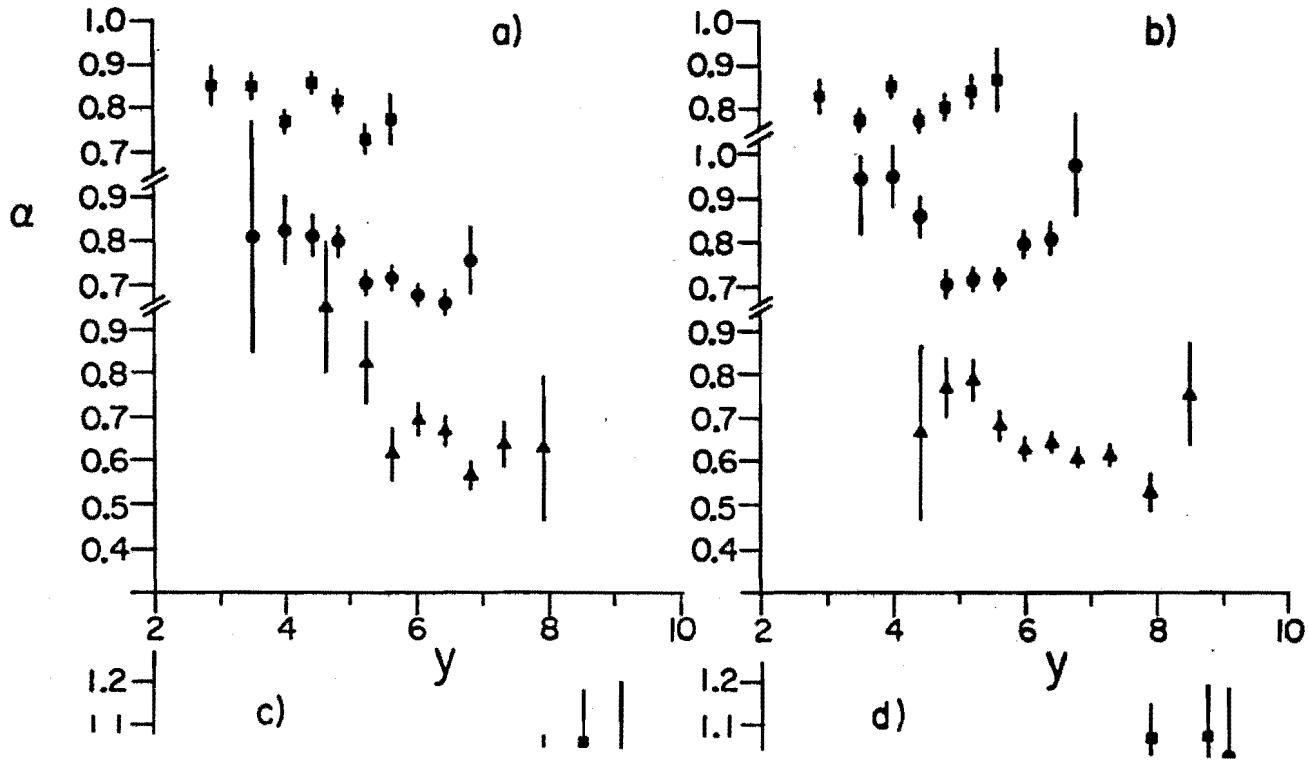
a)
b)
c)
d)
α
y
y
1.0
0.9
0.8
0.7
0.6
0.5
0.4
1.2
1.1
2
4
6
8
10

the spectrometer. We estimate that the systematic biases contribute to a ±15% overall uncertainty in the absolute cross sectional measurements. The neutron-flux normalization is the largest component of these biases, and crude cross checking leads us to believe that the error in the flux measurement is accurate to ∿10% (see Appendix A). (Comparisons with other data, cf Ref. 21, indicate that the multiplicities reported here are higher than previously observed.) The systematic uncertainty in the determination of the atomic-weight dependence of the data (i.e., the α-parameter) is about ±5%. In addition, possible electron contamination, which we expect to be localized to transverse momenta below $p_T^2 = 0.01(\mathrm{GeV/c})^2$, is such that in this region of phase space we estimate that the remnant contamination justifies doubling the statistical error bars both for the cross section and for the α-parameters.

F. CONCLUSIONS

There has recently been a renewal of interest in the study of particle production using nuclear targets. Experiments performed in the past few years have reported features which agree qualitatively with those observed in our data. However, our experiment, the first on neutron-nuclear collisions, provides the richest and most complete

information on single-particle production spectra in high-energy hadron-nucleus collisions. We have measured momenta and angles of final-state particles and examined the dependence of α on p_T^2. Although a rise in α was observed previously[18] at small p_T^2 for a fixed production angle, our data have provided the evidence needed to show that this effect was not just a kinematic consequence of the fixed angle in that experiment (as was suggested by Dar et al[19]), but a general phenomenon occurring over an extended region of phase space. The behavior of our data at large p_T^2 supports the small rise in α seen in previous proton-nucleus experiments.[20].

The atomic-weight dependence of the inclusive cross section as a function of pseudo-rapidity η has been investigated previously by others[21] and their results indicated that at small angles multiplicity becomes independent of A. Our data show a definite dependence on A, in that α falls well below a value of 0.69 at large rapidity. This observation excludes from consideration recently favored simple multiperipheral (single-Regge-pole exchange[3]) and energy-flux cascade[4] models, and suggests that multi-Regge pole exchanges or cut contributions are important in hadron-neucleus collisions. However, when our data are examined as a function of η, the results are consistent with those of Busza et al[21] (i.e., $\alpha \simeq 0.69$).

Consequently, it appears that theoretical predictions for $\alpha(y)$ cannot be assumed to hold without modification for $\alpha(\eta)$. While the decrease of α with increasing η (or y) can be explained by several diverse models[22], the Parton-Cascade model[23] has explicitly predicted a decrease in α followed by a small increase at largest values of η. We observe a very large increase in α for $\eta > 7$. This rise in our data, however, might be caused, at least partially, by the electromagnetic interaction of the neutron producing a low mass resonance (e.g. the $\Delta^\circ[1232]$) in the forward direction[24]; the atomic-weight dependence of such a reaction would be proportional to A^2, and the coherent production cross section is large enough so that the decay products ($\Delta^\circ \rightarrow p\pi^-$) could provide a non-negligible contribution at small angles. However, if this effect were due to electromagnetic processes alone, we would expect large increase in α for π^- and protons and not for π^+ data. Thus at present there is no clear understanding of our observed increase in α at small p_T, nor can the increase of α for large η be attributed entirely to coulombic processes. As for the rest of our findings, they appear to be in at least qualitative agreement with the predictions of a variety of models. Detailed calculations will be required to establish which of these models, if any, can provide an understanding of all of the production phenomena found in this work.

TABLE IV.1.A ALL -

PTSQ RANGE	BE		AL		CU		SN		PB		ALPHA		CHI
0.00 0.04	.134+2	.54+0	.164+2	.62+0	.170+2	.54+0	.191+2	.63+0	.193+2	.72+0	0.806	0.015	3.7
0.04 0.08	.749+1	.43+0	.804+1	.46+0	.837+1	.41+0	.939+1	.48+0	.936+1	.56+0	0.768	0.023	1.0
0.08 0.24	.318+1	.18+0	.353+1	.19+0	.371+1	.17+0	.379+1	.19+0	.391+1	.22+0	0.754	0.022	0.3
0.24 0.48	.578+0	.52-1	.934+0	.69-1	.927+0	.62-1	.918+0	.67-1	.827+0	.74-1	0.790	0.035	14.4
0.48 0.84	.135+0	.21-1	.210+0	.27-1	.213+0	.24-1	.245+0	.28-1	.258+0	.33-1	0.874	0.056	1.6
0.84 1.36	.560-1	.12-1	.342-1	.98-2	.607-1	.11-1	.579-1	.12-1	.540-1	.13-1	0.727	0.093	3.0
1.36 2.00	.684-2	.40-2	.170-1	.65-2	.139-1	.48-2	.241-1	.67-2	.124-1	.74-2	0.964	0.200	2.7

TABLE IV.1.B ALL +

PTSQ RANGE	BE		AL		CU		SN		PB		ALPHA		CHI
0.00 0.04	.123+2	.58+0	.162+2	.70+0	.187+2	.66+0	.182+2	.66+0	.194+2	.80+0	0.824	0.018	10.8
0.04 0.08	.676+1	.45+0	.801+1	.51+0	.834+1	.46+0	.928+1	.53+0	.887+1	.61+0	0.785	0.026	1.7
0.08 0.24	.388+1	.20+0	.433+1	.22+0	.422+1	.20+0	.427+1	.21+0	.450+1	.26+0	0.727	0.021	1.3
0.24 0.48	.951+0	.68-1	.134+1	.88-1	.135+1	.78-1	.113+1	.78-1	.110+1	.95-1	0.728	0.030	17.8
0.48 0.84	.306+0	.28-1	.408+0	.34-1	.458+0	.32-1	.473+0	.37-1	.512+0	.46-1	0.845	0.036	1.5
0.84 1.36	.140+0	.17-1	.174+0	.19-1	.174+0	.17-1	.199+0	.19-1	.182+0	.21-1	0.781	0.046	1.4
1.36 2.00	.541-1	.90-2	.599-1	.11-1	.779-1	.11-1	.610-1	.10-1	.652-1	.12-1	0.755	0.070	2.5

Differential multiplicity for each target and the value of Alpha with statistical errors only; CHI is the value of the chi-squared for the fit. All values are expressed in exponential notation: .134 + 2 = 13.4.

TABLE IV.1.C PI +

PTSQ	RANGE	BE		AL		CU		SN		PB		ALPHA		CHI
0.00	0.04	.121+2	.58+0	.159+2	.70+0	.184+2	.65+0	.179+2	.66+0	.192+2	.80+0	0.827	0.018	10.8
0.04	0.08	.652+1	.45+0	.774+1	.51+0	.814+1	.46+0	.906+1	.53+0	.867+1	.61+0	0.789	0.027	1.6
0.08	0.24	.369+1	.20+0	.411+1	.22+0	.405+1	.20+0	.409+1	.21+0	.436+1	.26+0	0.732	0.022	1.1
0.24	0.48	.809+0	.68-1	.121+1	.88-1	.121+1	.78-1	.101+1	.78-1	.988+0	.94-1	0.738	0.034	17.1
0.48	0.84	.217+0	.27-1	.307+0	.33-1	.361+0	.31-1	.374+0	.36-1	.425+0	.45-1	0.888	0.046	1.2
0.84	1.36	.963-1	.16-1	.112+0	.18-1	.115+0	.16-1	.141+0	.18-1	.137+0	.20-1	0.813	0.062	0.5
1.36	2.00	.255-1	.81-2	.336-1	.99-2	.440-1	.97-2	.309-1	.90-2	.308-1	.11-1	0.762	0.130	2.1

TABLE IV.1.D PROTONS

PTSQ	RANGE	BE		AL		CU		SN		PB		ALPHA		CHI
0.00	0.04	.265+0	.16-1	.283+0	.17-1	.257+0	.15-1	.257+0	.16-1	.240+0	.18-1	0.658	0.026	1.8
0.04	0.08	.241+0	.20-1	.270+0	.22-1	.209+0	.18-1	.226+0	.20-1	.200+0	.22-1	0.625	0.037	4.1
0.08	0.24	.183+0	.11-1	.218+0	.13-1	.171+0	.10-1	.177+0	.11-1	.137+0	.12-1	0.616	0.028	13.5
0.24	0.48	.142+0	.11-1	.134+0	.10-1	.139+0	.97-2	.119+0	.99-2	.107+0	.11-1	0.619	0.034	2.6
0.48	0.84	.897-1	.79-2	.101+0	.87-2	.970-1	.75-2	.991-1	.84-2	.875-1	.91-2	0.693	0.037	2.0
0.84	1.36	.439-1	.51-2	.620-1	.64-2	.588-1	.55-2	.576-1	.61-2	.441-1	.64-2	0.719	0.049	7.7
1.36	2.00	.286-1	.40-2	.263-1	.38-2	.339-1	.42-2	.301-1	.43-2	.344-1	.53-2	0.752	0.058	1.4

Differential multiplicity for each target and the value of Alpha with statistical errors only; CHI is the value of the chi-squared for the fit. All values are expressed in exponential notation: .134 + 2 = 13.4.

TABLE IV.2.A ALL -

PL	RANGE	BE		AL		CU		SN		PB		ALPHA		CHI
0.	4.	.188+0	.22-1	.218+0	.25-1	.292+0	.25-1	.277+0	.26-1	.334+0	.33-1	0.868	0.044	2.0
4.	8.	.300+0	.22-1	.447+0	.30-1	.445+0	.25-1	.455+0	.27-1	.464+0	.32-1	0.809	0.028	8.7
8.	16.	.117+0	.71-2	.145+0	.81-2	.165+0	.84-2	.183+0	.93-2	.166+0	.10-1	0.823	0.024	6.0
16.	24.	.456-1	.33-2	.577-1	.38-2	.617-1	.36-2	.661-1	.40-2	.676-1	.45-2	0.811	0.028	1.5
24.	36.	.212-1	.12-2	.272-1	.15-2	.266-1	.13-2	.286-1	.14-2	.286-1	.19-2	0.781	0.023	4.6
36.	52.	.898-2	.54-3	.109-1	.64-3	.110-1	.60-3	.103-1	.60-3	.102-1	.74-3	0.727	0.025	5.4
52.	80.	.322-2	.19-3	.365-2	.22-3	.389-2	.22-3	.373-2	.24-3	.335-2	.26-3	0.723	0.026	5.0
80.	116.	.739-3	.68-4	.805-3	.77-4	.833-3	.79-4	.735-3	.86-4	.764-3	.10-3	0.699	0.043	1.2
116.	156.	.151-3	.31-4	.126-3	.27-4	.175-3	.31-4	.157-3	.38-4	.208-3	.53-4	0.787	0.091	1.5
156.	200.	.428-4	.17-4	.260-4	.16-4	.487-4	.18-4	.377-4	.19-4	.408-4	.24-4	0.698	0.187	0.8
200.	400.	.915-3	.21-3	.103-2	.21-3	.118-2	.22-3	.933-3	.23-3	.111-2	.29-3	0.737	0.097	0.8

TABLE IV.2.B ALL +

PL	RANGE	BE		AL		CU		SN		PB		ALPHA		CHI
0.	4.	.305+0	.31-1	.366+0	.34-1	.425+0	.32-1	.481+0	.38-1	.423+0	.41-1	0.821	0.039	2.9
4.	8.	.392+0	.26-1	.515+0	.29-1	.518+0	.26-1	.513+0	.28-1	.635+0	.36-1	0.810	0.024	6.8
8.	16.	.138+0	.78-2	.178+0	.95-2	.184+0	.85-2	.183+0	.91-2	.203+0	.11-1	0.795	0.022	4.5
16.	24.	.526-1	.37-2	.687-1	.46-2	.753-1	.44-2	.778-1	.50-2	.767-1	.59-2	0.814	0.029	3.5
24.	36.	.232-1	.15-2	.319-1	.20-2	.328-1	.18-2	.345-1	.19-2	.340-1	.23-2	0.809	0.026	6.1
36.	52.	.114-1	.74-3	.125-1	.76-3	.147-1	.82-3	.133-1	.82-3	.153-1	.11-2	0.774	0.026	3.5
52.	80.	.441-2	.29-3	.544-2	.34-3	.534-2	.29-3	.505-2	.32-3	.496-2	.38-3	0.721	0.027	5.5
80.	116.	.185-2	.13-3	.220-2	.16-3	.223-2	.14-3	.228-2	.14-3	.174-2	.16-3	0.712	0.030	10.1
116.	156.	.916-3	.72-4	.118-2	.86-4	.991-3	.73-4	.869-3	.76-4	.955-3	.99-4	0.668	0.035	8.7
156.	200.	.585-3	.50-4	.643-3	.53-4	.621-3	.50-4	.578-3	.52-4	.430-3	.53-4	0.635	0.038	6.2
200.	400.	.123-1	.64-3	.119-1	.64-3	.111-1	.56-3	.892-2	.53-3	.989-2	.68-3	0.597	0.023	5.8

Differential multiplicity for each target and the value of Alpha with statistical errors only; CHI is the value of the chi-squared for the fit. All values are expressed in exponential notation: .134 + 2 = 13.4.

TABLE IV.3.A ALL -

Y RANGE		BE		AL		CU		SN		PB		ALPHA		CHI
2.60	3.20	.138+1	.17+0	.182+1	.20+0	.222+1	.19+0	.186+1	.20+0	.251+1	.26+0	0.849	0.046	4.6
3.20	3.80	.168+1	.14+0	.226+1	.16+0	.270+1	.15+0	.298+1	.17+0	.261+1	.19+0	0.850	0.030	9.0
3.80	4.20	.173+1	.11+0	.235+1	.13+0	.204+1	.11+0	.244+1	.13+0	.235+1	.14+0	0.774	0.025	10.4
4.20	4.60	.116+1	.64-1	.146+1	.72-1	.169+1	.70-1	.183+1	.76-1	.191+1	.91-1	0.851	0.020	1.6
4.60	5.00	.774+0	.40-1	.916+0	.44-1	.107+1	.42-1	.115+1	.47-1	.110+1	.55-1	0.817	0.020	4.8
5.00	5.40	.517+0	.24-1	.609+0	.26-1	.592+0	.23-1	.577+0	.25-1	.592+0	.29-1	0.721	0.019	5.2
5.40	5.80	.317+0	.14-1	.353+0	.16-1	.345+0	.14-1	.355+0	.15-1	.327+0	.17-1	0.707	0.019	4.1
5.80	6.20	.181+0	.84-2	.181+0	.86-2	.173+0	.73-2	.172+0	.79-2	.185+0	.97-2	0.684	0.019	1.9
6.20	6.60	.802-1	.42-2	.843-1	.45-2	.827-1	.39-2	.779-1	.41-2	.733-1	.48-2	0.666	0.023	2.3
6.60	7.00	.342-1	.21-2	.327-1	.21-2	.301-1	.18-2	.250-1	.18-2	.247-1	.21-2	0.580	0.028	2.3
7.00	7.60	.504-2	.58-3	.600-2	.65-3	.496-2	.52-3	.444-2	.55-3	.477-2	.68-3	0.639	0.050	2.8
7.60	8.20	.397-3	.15-3	.474-3	.17-3	.268-3	.12-3	.370-3	.15-3	.376-3	.18-3	0.630	0.167	0.9

TABLE IV.3.B ALL +

Y RANGE		BE		AL		CU		SN		PB		ALPHA		CHI
2.60	3.20	.234+1	.22+0	.253+1	.24+0	.290+1	.22+0	.346+1	.27+0	.351+1	.31+0	0.834	0.037	1.0
3.20	3.80	.243+1	.16+0	.352+1	.20+0	.351+1	.18+0	.324+1	.19+0	.363+1	.23+0	0.783	0.026	12.5
3.80	4.20	.164+1	.11+0	.251+1	.14+0	.258+1	.13+0	.261+1	.14+0	.325+1	.18+0	0.865	0.024	11.5
4.20	4.60	.154+1	.82-1	.181+1	.89-1	.202+1	.83-1	.214+1	.93-1	.208+1	.10+0	0.793	0.021	2.7
4.60	5.00	.941+0	.46-1	.111+1	.51-1	.122+1	.47-1	.117+1	.49-1	.117+1	.57-1	0.759	0.019	6.3
5.00	5.40	.565+0	.26-1	.698+0	.30-1	.713+0	.27-1	.731+0	.29-1	.698+0	.33-1	0.757	0.018	7.8
5.40	5.80	.346+0	.16-1	.389+0	.17-1	.408+0	.15-1	.373+0	.16-1	.367+0	.19-1	0.709	0.019	7.8
5.80	6.20	.201+0	.95-2	.229+0	.10-1	.214+0	.88-2	.207+0	.93-2	.209+0	.11-1	0.690	0.020	4.5
6.20	6.60	.115+0	.57-2	.122+0	.60-2	.117+0	.52-2	.118+0	.55-2	.105+0	.62-2	0.674	0.021	3.2
6.60	7.00	.604-1	.32-2	.642-1	.34-2	.577-1	.28-2	.517-1	.29-2	.482-1	.33-2	0.616	0.023	5.1
7.00	7.60	.210-1	.11-2	.231-1	.12-2	.190-1	.10-2	.185-1	.11-2	.168-1	.12-2	0.613	0.024	6.7
7.60	8.20	.658-2	.60-3	.628-2	.61-3	.410-2	.44-3	.445-2	.50-3	.439-2	.58-3	0.528	0.043	4.5
8.20	8.80	.489-3	.16-3	.110-2	.25-3	.797-3	.19-3	.993-3	.22-3	.663-3	.21-3	0.752	0.120	5.0

Differential multiplicity for each target and the value of Alpha with statistical errors only; CHI is the value of the chi-squared for the fit. All values are expressed in exponential notation: .134 + 2 = 13.4.

TABLE IV.3.C PI +

Y RANGE		BE		AL		CU		SN		PB		ALPHA		CHI
2.60	3.20	.234+1	.22+0	.253+1	.24+0	.290+1	.22+0	.346+1	.27+0	.351+1	.31+0	0.834	0.037	1.0
3.20	3.80	.243+1	.16+0	.352+1	.20+0	.351+1	.18+0	.324+1	.19+0	.363+1	.23+0	0.783	0.026	12.5
3.80	4.20	.164+1	.11+0	.251+1	.14+0	.258+1	.13+0	.261+1	.14+0	.325+1	.18+0	0.865	0.024	11.5
4.20	4.60	.154+1	.82-1	.181+1	.89-1	.201+1	.83-1	.213+1	.93-1	.208+1	.10+0	0.794	0.021	2.6
4.60	5.00	.920+0	.46-1	.108+1	.50-1	.120+1	.47-1	.115+1	.49-1	.114+1	.56-1	0.760	0.020	6.4
5.00	5.40	.514+0	.25-1	.637+0	.28-1	.635+0	.25-1	.644+0	.27-1	.638+0	.31-1	0.751	0.019	6.4
5.40	5.80	.259+0	.13-1	.283+0	.14-1	.299+0	.13-1	.277+0	.13-1	.278+0	.16-1	0.712	0.021	3.7
5.80	6.20	.964-1	.62-2	.109+0	.67-2	.113+0	.60-2	.119+0	.65-2	.119+0	.78-2	0.759	0.025	0.4
6.20	6.60	.320-1	.26-2	.391-1	.29-2	.385-1	.26-2	.447-1	.30-2	.424-1	.33-2	0.784	0.032	2.2
6.60	7.00	.835-2	.91-3	.829-2	.92-3	.846-2	.84-3	.806-2	.84-3	.983-2	.11-2	0.723	0.044	1.6
7.00	7.60	.161-3	.93-4	.111-3	.79-4	.432-4	.43-4	.472-4	.47-4	.832-4	.83-4	0.334	0.308	0.7

TABLE IV.3.D PROTONS

Y RANGE		BE		AL		CU		SN		PB		ALPHA		CHI
3.80	4.20	.000+0	.48+6	.000+0	.22+6	.000+0	.12+6	.000+0	.81+5	.000+0	.55+5	0.000	0.000	0.0
4.20	4.60	.634-2	.40-2	.206-1	.71-2	.111-1	.49-2	.715-2	.41-2	.264-2	.30-2	0.452	0.270	5.3
4.60	5.00	.525-1	.88-2	.673-1	.97-2	.782-1	.94-2	.729-1	.98-2	.518-1	.11-1	0.753	0.069	4.7
5.00	5.40	.149+0	.99-2	.166+0	.11-1	.173+0	.98-2	.179+0	.11-1	.160+0	.12-1	0.729	0.027	2.9
5.40	5.80	.125+0	.72-2	.141+0	.78-2	.120+0	.65-2	.975-1	.64-2	.904-1	.75-2	0.582	0.026	13.3
5.80	6.20	.735-1	.46-2	.739-1	.47-2	.627-1	.38-2	.585-1	.40-2	.589-1	.47-2	0.603	0.027	1.9
6.20	6.60	.329-1	.24-2	.320-1	.23-2	.293-1	.20-2	.258-1	.20-2	.238-1	.24-2	0.589	0.032	1.4
6.60	7.00	.591-2	.71-3	.547-2	.71-3	.446-2	.56-3	.397-2	.58-3	.326-2	.64-3	0.515	0.057	0.7
7.00	7.60	.000+0	.48+6	.000+0	.22+6	.000+0	.12+6	.000+0	.81+5	.000+0	.55+5	0.000	0.000	0.0

Differential multiplicity for each target and the value of Alpha with statistical errors only; CHI is the value of the chi-squared for the fit. All values are expressed in exponential notation: .134 + 2 = 13.4.

TABLE IV.4.A ALL - 4.0 < Y < 5.0

PTSQ RANGE		BE		AL		CU		SN		PB		ALPHA		CHI
0.00	0.04	.864+1	.51+0	.111+2	.59+0	.119+2	.52+0	.140+2	.61+0	.142+2	.69+0	0.849	0.022	2.4
0.04	0.08	.510+1	.41+0	.540+1	.43+0	.580+1	.39+0	.692+1	.45+0	.707+1	.54+0	0.805	0.031	1.6
0.08	0.24	.240+1	.17+0	.271+1	.18+0	.289+1	.16+0	.297+1	.18+0	.301+1	.21+0	0.763	0.028	0.5
0.24	0.48	.447+0	.50-1	.763+0	.67-1	.783+0	.60-1	.797+0	.66-1	.708+0	.72-1	0.818	0.041	11.6
0.48	0.84	.115+0	.20-1	.180+0	.27-1	.182+0	.24-1	.216+0	.27-1	.231+0	.32-1	0.890	0.063	1.2
0.84	1.36	.509-1	.12-1	.307-1	.96-2	.560-1	.11-1	.551-1	.12-1	.481-1	.13-1	0.733	0.100	2.8
1.36	2.00	.569-2	.39-2	.150-1	.63-2	.903-2	.45-2	.165-1	.63-2	.115-1	.72-2	0.870	0.233	1.9
						5.0 < Y < 6.0								
0.00	0.04	.174+1	.78-1	.203+1	.88-1	.194+1	.75-1	.200+1	.82-1	.195+1	.95-1	0.723	0.018	4.6
0.04	0.08	.100+1	.67-1	.111+1	.73-1	.109+1	.64-1	.105+1	.68-1	.945+0	.77-1	0.681	0.028	3.3
0.08	0.24	.351+0	.21-1	.383+0	.22-1	.377+0	.19-1	.387+0	.21-1	.414+0	.26-1	0.731	0.024	0.8
0.24	0.48	.626-1	.71-2	.815-1	.85-2	.695-1	.69-2	.601-1	.71-2	.566-1	.85-2	0.644	0.049	5.3
0.48	1.08	.615-2	.16-2	.912-2	.19-2	.995-2	.18-2	.935-2	.20-2	.869-2	.24-2	0.797	0.101	1.3
1.08	2.00	.106-2	.57-3	.714-3	.56-3	.156-2	.59-3	.238-2	.80-3	.823-3	.75-3	0.956	0.227	2.2
						6.0 < Y < 8.0								
0.00	0.04	.125+1	.49-1	.128+1	.51-1	.122+1	.44-1	.115+1	.46-1	.115+1	.55-1	0.655	0.017	1.8
0.04	0.08	.385+0	.35-1	.411+0	.37-1	.385+0	.31-1	.383+0	.34-1	.343+0	.39-1	0.662	0.039	1.1
0.08	0.24	.791-1	.84-2	.580-1	.74-2	.584-1	.64-2	.492-1	.67-2	.760-1	.94-2	0.631	0.047	9.5
0.24	0.48	.563-2	.17-2	.817-2	.22-2	.437-2	.14-2	.816-3	.11-2	.455-2	.21-2	0.543	0.159	3.9
0.48	1.08	.155-2	.56-3	.151-2	.58-3	.143-2	.56-3	.370-3	.36-3	.173-2	.75-3	0.662	0.170	2.2
1.08	2.00	.466-3	.29-3	.713-3	.34-3	.995-3	.35-3	.762-3	.32-3	.152-3	.23-3	0.815	0.263	2.1

Differential multiplicity for each target and the value of Alpha with statistical errors only; CHI is the value of the chi-squared for the fit. All values are expressed in exponential notation: .134 + 2 = 13.4.

TABLE IV.4.B ALL + 4.0 < Y < 5.0

PTSQ RANGE		BE		AL		CU		SN		PB		ALPHA		CHI
0.00	0.04	.892+1	.56+0	.122+2	.68+0	.144+2	.64+0	.136+2	.63+0	.149+2	.77+0	0.836	0.023	9.7
0.04	0.08	.478+1	.43+0	.598+1	.50+0	.622+1	.45+0	.716+1	.51+0	.683+1	.59+0	0.811	0.035	1.7
0.08	0.24	.298+1	.19+0	.331+1	.22+0	.331+1	.20+0	.334+1	.21+0	.355+1	.26+0	0.736	0.027	0.6
0.24	0.48	.630+0	.65-1	.967+0	.85-1	.964+0	.75-1	.821+0	.75-1	.811+0	.92-1	0.748	0.041	11.5
0.48	0.84	.184+0	.26-1	.247+0	.31-1	.311+0	.30-1	.318+0	.35-1	.379+0	.44-1	0.908	0.052	0.7
0.84	1.36	.967-1	.16-1	.106+0	.18-1	.112+0	.15-1	.140+0	.18-1	.128+0	.20-1	0.803	0.063	0.9
1.36	2.00	.310-1	.84-2	.343-1	.99-2	.480-1	.98-2	.369-1	.93-2	.354-1	.11-1	0.761	0.114	1.7
						5.0 < Y < 6.0								
0.00	0.04	.128+1	.73-1	.154+1	.82-1	.172+1	.77-1	.181+1	.83-1	.176+1	.97-1	0.798	0.022	3.1
0.04	0.08	.796+0	.65-1	.784+0	.63-1	.869+0	.60-1	.860+0	.64-1	.822+0	.73-1	0.715	0.033	0.9
0.08	0.24	.359+0	.21-1	.406+0	.23-1	.373+0	.20-1	.383+0	.22-1	.402+0	.25-1	0.711	0.024	2.3
0.24	0.48	.120+0	.10-1	.151+0	.12-1	.159+0	.11-1	.127+0	.10-1	.116+0	.12-1	0.687	0.036	12.2
0.48	0.84	.453-1	.50-2	.627-1	.61-2	.566-1	.51-2	.641-1	.58-2	.524-1	.61-2	0.747	0.043	5.9
0.84	1.36	.152-1	.24-2	.280-1	.33-2	.233-1	.27-2	.251-1	.30-2	.212-1	.35-2	0.769	0.060	8.9
1.36	2.00	.793-2	.15-2	.975-2	.17-2	.131-1	.18-2	.100-1	.18-2	.116-1	.22-2	0.803	0.075	2.9
						6.0 < Y < 8.0								
0.00	0.04	.814+0	.38-1	.881+0	.40-1	.878+0	.36-1	.984+0	.41-1	.929+0	.46-1	0.741	0.019	2.7
0.04	0.08	.387+0	.30-1	.459+0	.35-1	.383+0	.29-1	.398+0	.32-1	.400+0	.38-1	0.681	0.033	3.6
0.08	0.24	.182+0	.11-1	.206+0	.12-1	.165+0	.97-2	.162+0	.10-1	.124+0	.11-1	0.589	0.028	11.7
0.24	0.48	.801-1	.65-2	.743-1	.63-2	.699-1	.55-2	.588-1	.55-2	.519-1	.64-2	0.566	0.038	1.5
0.48	0.84	.318-1	.34-2	.356-1	.38-2	.335-1	.32-2	.264-1	.31-2	.286-1	.38-2	0.635	0.046	3.2
0.84	1.36	.131-1	.19-2	.124-1	.20-2	.153-1	.19-2	.851-2	.16-2	.110-1	.21-2	0.625	0.066	6.5
1.36	2.00	.725-2	.13-2	.611-2	.13-2	.372-2	.89-3	.400-2	.10-2	.528-2	.14-2	0.517	0.086	2.9

Differential multiplicity for each target and the value of Alpha with statistical errors only; CHI is the value of the chi-squared for the fit. All values are expressed in exponential notation: .134 + 2 = 13.4.

TABLE IV.4.C PI + 4.0 < Y < 5.0

PTSQ RANGE	BE		AL		CU		SN		PB		ALPHA		CHI
0.00 0.04	.892+1	.56+0	.122+2	.68+0	.144+2	.64+0	.136+2	.63+0	.149+2	.77+0	0.836	0.023	9.7
0.04 0.08	.478+1	.43+0	.598+1	.50+0	.622+1	.45+0	.716+1	.51+0	.683+1	.59+0	0.811	0.035	1.7
0.08 0.24	.298+1	.19+0	.331+1	.22+0	.331+1	.20+0	.334+1	.21+0	.355+1	.26+0	0.736	0.027	0.6
0.24 0.48	.630+0	.65-1	.967+0	.85-1	.964+0	.75-1	.821+0	.75-1	.811+0	.92-1	0.748	0.041	11.5
0.48 0.84	.184+0	.26-1	.247+0	.31-1	.311+0	.30-1	.318+0	.35-1	.379+0	.44-1	0.908	0.052	0.7
0.84 1.36	.969-1	.16-1	.104+0	.17-1	.112+0	.15-1	.140+0	.18-1	.128+0	.20-1	0.804	0.063	0.9
1.36 2.00	.255-1	.81-2	.336-1	.99-2	.440-1	.97-2	.309-1	.90-2	.308-1	.11-1	0.762	0.130	2.1
					5.0 < Y < 6.0								
0.00 0.04	.256+1	.15+0	.308+1	.16+0	.344+1	.15+0	.361+1	.17+0	.352+1	.19+0	0.798	0.022	3.1
0.04 0.08	.159+1	.13+0	.157+1	.13+0	.174+1	.12+0	.172+1	.13+0	.164+1	.15+0	0.715	0.033	0.9
0.08 0.24	.702+0	.42-1	.786+0	.46-1	.726+0	.39-1	.741+0	.43-1	.779+0	.50-1	0.708	0.025	2.0
0.24 0.48	.178+0	.19-1	.243+0	.22-1	.249+0	.20-1	.194+0	.19-1	.177+0	.23-1	0.689	0.044	11.7
0.48 0.84	.326-1	.69-2	.594-1	.93-2	.498-1	.75-2	.555-1	.84-2	.460-1	.91-2	0.769	0.078	5.0
0.84 1.36	.000+0	.00+0	.820-2	.30-2	.300-2	.17-2	.871-3	.15-2	.956-2	.37-2	0.761	0.259	4.3
1.36 2.00	.000+0	.00+0	.000+0	.00+0	.000+0	.00+0	.000+0	.00+0	.000+0	.00+0	0.000	0.000	0.0
					6.0 < Y < 8.0								
0.00 0.04	.284+0	.17-1	.316+0	.18-1	.322+0	.16-1	.375+0	.19-1	.358+0	.21-1	0.775	0.024	2.4
0.04 0.08	.742-1	.12-1	.962-1	.13-1	.893-1	.11-1	.866-1	.12-1	.930-1	.15-1	0.735	0.062	1.2
0.08 0.24	.771-2	.20-2	.688-2	.19-2	.697-2	.17-2	.432-2	.15-2	.602-2	.21-2	0.574	0.118	1.0
0.24 0.48	.000+0	.00+0	.000+0	.00+0	.000+0	.00+0	.000+0	.00+0	.000+0	.00+0	0.000	0.000	0.0

Differential multiplicity for each target and the value of Alpha with statistical errors only; CHI is the value of the chi-squared for the fit. All values are expressed in exponential notation: .134 + 2 = 13.4.

TABLE IV.4.D PROTONS 4.0 < Y < 5.0

PTSQ RANGE	BE		AL		CU		SN		PB		ALPHA		CHI
0.08 0.24	.000+0	.00+0	.000+0	.00+0	.000+0	.00+0	.000+0	.00+0	.000+0	.00+0	0.000	0.000	0.0
0.24 0.48	.413-2	.26-2	.157-2	.20-2	.598-2	.28-2	.525-2	.30-2	.000+0	.00+0	0.847	0.315	0.9
0.48 0.84	.149-1	.41-2	.202-1	.48-2	.197-1	.42-2	.223-1	.48-2	.926-2	.38-2	0.717	0.116	4.3
0.84 1.36	.816-2	.29-2	.171-1	.42-2	.125-1	.32-2	.166-1	.40-2	.699-2	.38-2	0.767	0.142	4.9
1.36 2.00	.925-2	.29-2	.577-2	.23-2	.133-1	.32-2	.132-1	.33-2	.146-1	.40-2	0.882	0.122	2.3
5.0 < Y < 6.0													
0.00 0.04	.206+0	.14-1	.218+0	.15-1	.215+0	.14-1	.210+0	.15-1	.184+0	.16-1	0.669	0.030	2.3
0.04 0.08	.181+0	.19-1	.212+0	.21-1	.180+0	.17-1	.185+0	.19-1	.162+0	.21-1	0.655	0.044	2.6
0.08 0.24	.150+0	.11-1	.187+0	.13-1	.140+0	.99-2	.146+0	.11-1	.117+0	.12-1	0.616	0.033	12.4
0.24 0.48	.117+0	.99-2	.107+0	.99-2	.114+0	.90-2	.938-1	.91-2	.893-1	.11-1	0.616	0.039	2.3
0.48 0.84	.590-1	.64-2	.676-1	.69-2	.629-1	.60-2	.657-1	.67-2	.644-1	.78-2	0.711	0.045	0.7
0.84 1.36	.298-1	.40-2	.392-1	.47-2	.393-1	.43-2	.348-1	.45-2	.295-1	.49-2	0.702	0.056	4.5
1.36 2.00	.155-1	.26-2	.180-1	.29-2	.189-1	.27-2	.149-1	.26-2	.161-1	.32-2	0.689	0.072	1.6
6.0 < Y < 8.0													
0.00 0.08	.243-1	.22-2	.215-1	.22-2	.111-1	.15-2	.159-1	.19-2	.165-1	.22-2	0.520	0.044	13.1
0.08 0.24	.169-1	.15-2	.156-1	.14-2	.154-1	.13-2	.158-1	.14-2	.985-2	.14-2	0.604	0.040	7.1
0.24 0.48	.105-1	.12-2	.127-1	.14-2	.944-2	.10-2	.100-1	.12-2	.888-2	.14-2	0.623	0.051	3.6
0.48 0.84	.789-2	.10-2	.686-2	.98-3	.715-2	.88-3	.555-2	.84-3	.552-2	.10-2	0.580	0.059	1.1
0.84 1.36	.296-2	.58-3	.279-2	.58-3	.351-2	.58-3	.308-2	.59-3	.367-2	.76-3	0.754	0.081	0.7
1.36 2.00	.195-2	.45-3	.130-2	.39-3	.850-3	.27-3	.101-2	.33-3	.147-2	.46-3	0.527	0.108	3.3

Differential multiplicity for each target and the value of Alpha with statistical errors only; CHI is the value of the chi-squared for the fit. All values are expressed in exponential notation: .134 + 2 = 13.4.

TABLE IV.5.A ALL - 2.5 < PL < 20.

PTSQ RANGE	BE		AL		CU		SN		PB		ALPHA		CHI
0.00 0.04	.583+0	.30-1	.747+0	.35-1	.792+0	.30-1	.902+0	.35-1	.921+0	.40-1	0.833	0.019	2.9
0.04 0.08	.287+0	.23-1	.302+0	.24-1	.324+0	.22-1	.385+0	.26-1	.397+0	.31-1	0.802	0.032	1.6
0.08 0.24	.991-1	.90-2	.115+0	.97-2	.119+0	.85-2	.123+0	.95-2	.126+0	.11-1	0.761	0.035	0.4
0.24 0.48	.732-2	.18-2	.146-1	.26-2	.140-1	.23-2	.147-1	.26-2	.118-1	.26-2	0.812	0.089	4.8
20. < PL < 60.													
0.00 0.04	.676-1	.28-2	.713-1	.30-2	.673-1	.25-2	.735-1	.29-2	.697-1	.33-2	0.703	0.017	2.9
0.04 0.08	.540-1	.35-2	.602-1	.38-2	.593-1	.34-2	.584-1	.37-2	.514-1	.41-2	0.689	0.027	3.7
0.08 0.24	.322-1	.20-2	.337-1	.21-2	.371-1	.20-2	.375-1	.21-2	.381-1	.26-2	0.749	0.026	0.4
0.24 0.48	.954-2	.10-2	.148-1	.13-2	.153-1	.11-2	.152-1	.12-2	.142-1	.15-2	0.802	0.040	8.1
0.48 0.84	.298-2	.51-3	.463-2	.67-3	.463-2	.59-3	.548-2	.69-3	.596-2	.81-3	0.887	0.061	1.2
0.84 1.36	.119-2	.30-3	.652-3	.23-3	.111-2	.25-3	.120-2	.29-3	.961-3	.31-3	0.688	0.110	2.5
1.36 2.00	.626-4	.82-4	.337-3	.15-3	.189-3	.11-3	.356-3	.15-3	.120-3	.15-3	0.814	0.336	2.6
60. < PL < 400.													
0.00 0.04	.129-2	.73-4	.133-2	.77-4	.125-2	.68-4	.107-2	.68-4	.963-3	.79-4	0.606	0.026	5.3
0.04 0.08	.834-3	.84-4	.976-3	.93-4	.896-3	.77-4	.908-3	.86-4	.793-3	.95-4	0.682	0.042	2.3
0.08 0.24	.436-3	.38-4	.450-3	.41-4	.377-3	.32-4	.410-3	.38-4	.479-3	.47-4	0.690	0.037	4.1
0.24 0.48	.191-3	.25-4	.241-3	.29-4	.189-3	.23-4	.150-3	.24-4	.124-3	.26-4	0.563	0.062	5.9
0.48 0.84	.439-4	.12-4	.693-4	.16-4	.762-4	.15-4	.709-4	.17-4	.558-4	.18-4	0.792	0.113	2.2
0.84 1.36	.231-4	.81-5	.226-4	.88-5	.458-4	.11-4	.273-4	.98-5	.426-4	.14-4	0.881	0.139	2.9
1.36 2.00	.121-4	.65-5	.965-5	.62-5	.176-4	.61-5	.273-4	.82-5	.127-4	.94-5	0.970	0.215	1.9

Differential multiplicity for each target and the value of Alpha with statistical errors only; CHI is the value of the chi-squared for the fit. All values are expressed in exponential notation: .134 + 2 = 13.4.

TABLE IV.5.B ALL + 2.5 < PL < 20.

PTSQ RANGE	BE		AL		CU		SN		PB		ALPHA		CHI
0.00 0.04	.576+0	.33-1	.791+0	.40-1	.920+0	.37-1	.885+0	.37-1	.967+0	.45-1	0.837	0.021	10.6
0.04 0.08	.265+0	.24-1	.336+0	.28-1	.354+0	.26-1	.405+0	.29-1	.387+0	.34-1	0.817	0.035	1.7
0.08 0.24	.128+0	.10-1	.144+0	.12-1	.142+0	.11-1	.139+0	.11-1	.157+0	.14-1	0.735	0.033	1.2
0.24 0.48	.931-2	.22-2	.184-1	.32-2	.162-1	.28-2	.110-1	.26-2	.123-1	.31-2	0.705	0.093	7.7
				20. < PL < 60.									
0.00 0.04	.451-1	.25-2	.477-1	.26-2	.549-1	.25-2	.567-1	.26-2	.512-1	.30-2	0.755	0.022	5.2
0.04 0.08	.440-1	.35-2	.427-1	.34-2	.452-1	.31-2	.464-1	.34-2	.434-1	.38-2	0.700	0.033	0.6
0.08 0.24	.335-1	.22-2	.373-1	.24-2	.363-1	.22-2	.394-1	.25-2	.380-1	.27-2	0.732	0.027	1.0
0.24 0.48	.145-1	.14-2	.196-1	.17-2	.208-1	.15-2	.190-1	.16-2	.180-1	.19-2	0.758	0.038	6.8
0.48 0.84	.445-2	.65-3	.626-2	.79-3	.781-2	.74-3	.792-2	.85-3	.934-2	.11-2	0.910	0.052	1.1
0.84 1.36	.207-2	.38-3	.239-2	.43-3	.236-2	.37-3	.294-2	.44-3	.239-2	.47-3	0.770	0.073	1.3
1.36 2.00	.296-3	.17-3	.738-3	.24-3	.853-3	.22-3	.517-3	.20-3	.620-3	.27-3	0.783	0.186	3.3
				60. < PL < 400.									
0.00 0.04	.121-2	.64-4	.120-2	.64-4	.114-2	.57-4	.123-2	.66-4	.116-2	.73-4	0.682	0.023	1.2
0.04 0.08	.101-2	.80-4	.117-2	.89-4	.965-3	.74-4	.959-3	.79-4	.101-2	.97-4	0.663	0.034	3.5
0.08 0.24	.805-3	.47-4	.904-3	.51-4	.776-3	.43-4	.747-3	.45-4	.633-3	.52-4	0.624	0.026	7.6
0.24 0.48	.576-3	.41-4	.653-3	.46-4	.655-3	.41-4	.503-3	.38-4	.442-3	.45-4	0.626	0.032	13.3
0.48 0.84	.356-3	.31-4	.439-3	.35-4	.405-3	.30-4	.414-3	.33-4	.359-3	.36-4	0.699	0.036	4.4
0.84 1.36	.159-3	.19-4	.218-3	.22-4	.221-3	.20-4	.225-3	.23-4	.239-3	.28-4	0.799	0.046	1.9
1.36 2.00	.117-3	.17-4	.845-4	.13-4	.122-3	.15-4	.112-3	.16-4	.112-3	.18-4	0.708	0.060	3.8

Differential multiplicity for each target and the value of Alpha with statistical errors only; CHI is the value of the chi-squared for the fit. All values are expressed in exponential notation: .134 + 2 = 13.4.

TABLE IV.6.A ALL -

ETA RANGE	BE		AL		CU		SN		PB		ALPHA		CHI
2.60 3.20	.110+1	.16+0	.161+1	.20+0	.179+1	.18+0	.150+1	.18+0	.208+1	.25+0	0.844	0.053	4.5
3.20 3.80	.173+1	.14+0	.220+1	.16+0	.266+1	.16+0	.272+1	.17+0	.243+1	.19+0	0.819	0.032	7.2
3.80 4.20	.153+1	.12+0	.200+1	.14+0	.201+1	.12+0	.238+1	.14+0	.214+1	.16+0	0.807	0.029	5.3
4.20 4.60	.120+1	.77-1	.166+1	.95-1	.166+1	.83-1	.182+1	.95-1	.197+1	.12+0	0.830	0.024	4.6
4.60 5.00	.871+0	.51-1	.107+1	.57-1	.122+1	.54-1	.137+1	.61-1	.146+1	.74-1	0.856	0.022	0.3
5.00 5.40	.623+0	.31-1	.755+0	.35-1	.809+0	.33-1	.875+0	.37-1	.832+0	.42-1	0.790	0.020	4.3
5.40 5.80	.447+0	.21-1	.490+0	.22-1	.505+0	.20-1	.499+0	.21-1	.490+0	.25-1	0.722	0.019	1.9
5.80 6.20	.224+0	.11-1	.272+0	.13-1	.248+0	.11-1	.272+0	.13-1	.281+0	.15-1	0.747	0.021	5.4
6.20 6.60	.152+0	.77-2	.146+0	.77-2	.165+0	.74-2	.160+0	.78-2	.148+0	.87-2	0.701	0.021	4.1
6.60 7.00	.811-1	.44-2	.757-1	.44-2	.864-1	.42-2	.782-1	.43-2	.830-1	.52-2	0.699	0.023	3.5
7.00 7.60	.306-1	.16-2	.364-1	.18-2	.369-1	.16-2	.324-1	.17-2	.316-1	.20-2	0.698	0.022	11.5
7.60 8.20	.102-1	.82-3	.121-1	.91-3	.116-1	.81-3	.124-1	.90-3	.135-1	.11-2	0.763	0.032	1.3
8.20 8.80	.389-2	.50-3	.426-2	.56-3	.439-2	.49-3	.527-2	.59-3	.700-2	.75-3	0.865	0.048	3.5
8.80 9.40	.151-2	.31-3	.153-2	.33-3	.238-2	.36-3	.306-2	.42-3	.379-2	.51-3	1.016	0.071	1.5

TABLE IV.6.B ALL +

2.60 3.20	.193+1	.21+0	.209+1	.22+0	.241+1	.21+0	.291+1	.25+0	.292+1	.28+0	0.839	0.041	1.0
3.20 3.80	.243+1	.17+0	.328+1	.21+0	.328+1	.18+0	.325+1	.20+0	.349+1	.24+0	0.783	0.028	5.3
3.80 4.20	.178+1	.14+0	.260+1	.17+0	.259+1	.15+0	.243+1	.15+0	.309+1	.20+0	0.818	0.028	10.7
4.20 4.60	.145+1	.88-1	.199+1	.11+0	.220+1	.10+0	.215+1	.11+0	.235+1	.14+0	0.826	0.023	6.9
4.60 5.00	.110+1	.59-1	.129+1	.66-1	.144+1	.61-1	.146+1	.68-1	.142+1	.77-1	0.779	0.021	3.8
5.00 5.40	.737+0	.37-1	.894+0	.40-1	.990+0	.38-1	.971+0	.40-1	.946+0	.47-1	0.773	0.019	7.8
5.40 5.80	.451+0	.22-1	.543+0	.25-1	.570+0	.23-1	.571+0	.25-1	.581+0	.29-1	0.766	0.019	3.7
5.80 6.20	.282+0	.13-1	.327+0	.15-1	.336+0	.13-1	.314+0	.14-1	.323+0	.17-1	0.725	0.019	5.4
6.20 6.60	.161+0	.80-2	.183+0	.91-2	.182+0	.79-2	.190+0	.87-2	.181+0	.10-1	0.733	0.021	2.5
6.60 7.00	.875-1	.45-2	.103+0	.52-2	.973-1	.45-2	.100+0	.49-2	.946-1	.58-2	0.715	0.022	4.3
7.00 7.60	.374-1	.18-2	.462-1	.20-2	.441-1	.19-2	.436-1	.20-2	.400-1	.22-2	0.712	0.020	11.9
7.60 8.20	.153-1	.10-2	.152-1	.10-2	.132-1	.87-3	.169-1	.11-2	.193-1	.13-2	0.749	0.027	12.4
8.20 8.80	.450-2	.55-3	.621-2	.67-3	.534-2	.56-3	.711-2	.68-3	.864-2	.88-3	0.871	0.045	5.1
8.80 9.40	.145-2	.31-3	.235-2	.40-3	.243-2	.37-3	.344-2	.49-3	.453-2	.61-3	1.036	0.070	1.7

Differential multiplicity for each target and the value of Alpha with statistical errors only; CHI is the value of the chi-squared for the fit. All values are expressed in exponential notation: .134 + 2 = 13.4.

TABLE IV.6.C PI +

ETA RANGE		BE		AL		CU		SN		PB		ALPHA		CHI
2.60	3.20	.193+1	.21+0	.209+1	.22+0	.241+1	.21+0	.291+1	.25+0	.292+1	.28+0	0.839	0.041	1.0
3.20	3.80	.243+1	.17+0	.328+1	.21+0	.328+1	.18+0	.325+1	.20+0	.349+1	.24+0	0.783	0.028	5.3
3.80	4.20	.178+1	.14+0	.260+1	.17+0	.259+1	.15+0	.243+1	.15+0	.309+1	.20+0	0.818	0.028	10.7
4.20	4.60	.145+1	.88-1	.198+1	.11+0	.219+1	.10+0	.214+1	.11+0	.235+1	.14+0	0.827	0.023	6.8
4.60	5.00	.108+1	.58-1	.126+1	.66-1	.142+1	.61-1	.144+1	.68-1	.139+1	.77-1	0.780	0.021	4.0
5.00	5.40	.686+0	.36-1	.833+0	.39-1	.913+0	.37-1	.889+0	.39-1	.887+0	.46-1	0.770	0.020	6.3
5.40	5.80	.368+0	.21-1	.441+0	.23-1	.467+0	.21-1	.476+0	.23-1	.503+0	.27-1	0.781	0.022	1.5
5.80	6.20	.176+0	.11-1	.208+0	.13-1	.235+0	.12-1	.227+0	.12-1	.228+0	.15-1	0.775	0.025	3.7
6.20	6.60	.827-1	.62-2	.103+0	.74-2	.106+0	.65-2	.118+0	.72-2	.120+0	.89-2	0.806	0.029	1.3
6.60	7.00	.386-1	.33-2	.510-1	.40-2	.511-1	.35-2	.582-1	.40-2	.587-1	.47-2	0.818	0.033	2.1
7.00	7.60	.157-1	.13-2	.205-1	.15-2	.233-1	.15-2	.242-1	.16-2	.232-1	.18-2	0.818	0.031	3.9
7.60	8.20	.552-2	.68-3	.711-2	.78-3	.619-2	.66-3	.945-2	.87-3	.120-1	.11-2	0.928	0.044	8.9
8.20	8.80	.173-2	.39-3	.284-2	.50-3	.278-2	.43-3	.479-2	.58-3	.606-2	.76-3	1.093	0.070	3.4
8.80	9.40	.523-3	.21-3	.950-3	.28-3	.125-2	.29-3	.227-2	.42-3	.312-2	.52-3	1.288	0.114	0.8

TABLE IV.6.D PROTONS

2.60	3.20	.000+0	.48+7	.000+0	.22+7	.000+0	.12+7	.000+0	.81+6	.000+0	.55+6	0.000	0.000	0.0
3.20	3.80	.000+0	.48+7	.000+0	.22+7	.000+0	.12+7	.000+0	.81+6	.000+0	.55+6	0.000	0.000	0.0
3.80	4.20	.000+0	.48+7	.000+0	.22+7	.000+0	.12+7	.000+0	.81+6	.000+0	.55+6	0.000	0.000	0.0
4.20	4.60	.469-2	.37-2	.659-2	.41-2	.676-2	.42-2	.383-2	.33-2	.000+0	.55+6	0.683	0.405	0.4
4.60	5.00	.206-1	.62-2	.283-1	.77-2	.225-1	.59-2	.168-1	.54-2	.286-1	.85-2	0.707	0.120	2.2
5.00	5.40	.507-1	.78-2	.608-1	.89-2	.764-1	.87-2	.826-1	.97-2	.594-1	.10-1	0.811	0.061	4.7
5.40	5.80	.824-1	.80-2	.102+0	.92-2	.103+0	.82-2	.949-1	.86-2	.781-1	.95-2	0.697	0.041	6.3
5.80	6.20	.106+0	.73-2	.118+0	.79-2	.101+0	.65-2	.867-1	.67-2	.938-1	.81-2	0.621	0.030	5.6
6.20	6.60	.783-1	.50-2	.798-1	.52-2	.757-1	.45-2	.721-1	.48-2	.601-1	.53-2	0.629	0.028	3.4
6.60	7.00	.489-1	.31-2	.516-1	.33-2	.463-1	.28-2	.420-1	.29-2	.359-1	.33-2	0.605	0.029	4.5
7.00	7.60	.217-1	.12-2	.257-1	.14-2	.208-1	.11-2	.194-1	.12-2	.167-1	.13-2	0.606	0.025	13.9
7.60	8.20	.975-2	.73-3	.808-2	.69-3	.705-2	.57-3	.745-2	.63-3	.723-2	.74-3	0.588	0.034	2.1
8.20	8.80	.277-2	.40-3	.338-2	.45-3	.256-2	.35-3	.232-2	.36-3	.257-2	.44-3	0.621	0.061	2.8
8.80	9.40	.925-3	.23-3	.140-2	.28-3	.118-2	.23-3	.117-2	.24-3	.892-3	.26-3	0.684	0.099	2.5

Differential multiplicity for each target and the value of Alpha with statistical errors only; CHI is the value of the chi-squared for the fit. All values are expressed in exponential notation: .134 + 2 = 13.4.

TABLE IV.7.A ALL - 2.5 < PL < 20.

Y RANGE		BE		AL		CU		SN		PB		ALPHA		CHI
2.60	3.20	.792-1	.96-2	.104+0	.12-1	.127+0	.11-1	.107+0	.11-1	.144+0	.15-1	0.849	0.045	4.6
3.20	3.80	.953-1	.76-2	.127+0	.90-2	.152+0	.87-2	.170+0	.98-2	.145+0	.11-1	0.850	0.030	9.8
3.80	4.20	.916-1	.62-2	.123+0	.73-2	.106+0	.58-2	.127+0	.69-2	.123+0	.78-2	0.769	0.026	9.8
4.20	4.60	.516-1	.32-2	.640-1	.37-2	.755-1	.35-2	.824-1	.39-2	.873-1	.47-2	0.859	0.023	0.8
4.60	5.00	.253-1	.16-2	.293-1	.18-2	.339-1	.17-2	.379-1	.19-2	.359-1	.22-2	0.820	0.025	2.9
5.00	5.40	.830-2	.66-3	.106-1	.77-3	.107-1	.67-3	.958-2	.69-3	.102-1	.82-3	0.734	0.032	5.7
5.40	5.80	.957-3	.14-3	.120-2	.17-3	.102-2	.13-3	.128-2	.16-3	.132-2	.20-3	0.778	0.059	1.7
5.80	6.20	.000+0	.00+0	.000+0	.00+0	.000+0	.00+0	.000+0	.00+0	.000+0	.00+0	0.000	0.000	0.0
						20. < PL < 60.								
2.60	3.20	.000+0	.00+0	.000+0	.00+0	.000+0	.00+0	.000+0	.00+0	.000+0	.00+0	0.000	0.000	0.0
3.20	3.80	.427-3	.51-3	.106-2	.43-3	.109-2	.51-3	.264-3	.30-3	.130-2	.58-3	0.810	0.264	2.1
3.80	4.20	.326-2	.68-3	.482-2	.84-3	.483-2	.74-3	.541-2	.84-3	.515-2	.10-2	0.826	0.078	1.1
4.20	4.60	.624-2	.74-3	.802-2	.82-3	.894-2	.77-3	.941-2	.84-3	.910-2	.10-2	0.813	0.044	1.4
4.60	5.00	.809-2	.69-3	.995-2	.76-3	.112-1	.75-3	.116-1	.80-3	.112-1	.96-3	0.801	0.033	2.1
5.00	5.40	.868-2	.49-3	.980-2	.54-3	.920-2	.46-3	.916-2	.50-3	.958-2	.61-3	0.707	0.024	2.1
5.40	5.80	.631-2	.32-3	.681-2	.34-3	.698-2	.31-3	.722-2	.33-3	.665-2	.38-3	0.719	0.021	2.4
5.80	6.20	.309-2	.17-3	.316-2	.17-3	.312-2	.15-3	.305-2	.16-3	.300-2	.18-3	0.681	0.022	0.3
6.20	6.60	.961-3	.65-4	.865-3	.62-4	.865-3	.54-4	.897-3	.61-4	.862-3	.69-4	0.663	0.029	1.0
6.60	7.00	.598-4	.11-4	.625-4	.12-4	.481-4	.93-5	.679-4	.12-4	.787-4	.14-4	0.760	0.075	2.8
7.00	7.60	.000+0	.00+0	.000+0	.00+0	.000+0	.00+0	.000+0	.00+0	.000+0	.00+0	0.000	0.000	0.0
						60. < PL < 400.								
4.20	5.00	.211-4	.96-5	.308-4	.12-4	.570-4	.12-4	.504-4	.14-4	.586-4	.17-4	0.994	0.152	1.6
5.00	5.40	.736-4	.17-4	.912-4	.19-4	.110-3	.18-4	.126-3	.21-4	.843-4	.23-4	0.824	0.092	2.5
5.40	5.80	.140-3	.18-4	.176-3	.20-4	.142-3	.16-4	.127-3	.18-4	.110-3	.21-4	0.614	0.058	4.1
5.80	6.20	.169-3	.15-4	.161-3	.15-4	.141-3	.13-4	.146-3	.14-4	.191-3	.18-4	0.694	0.037	6.5
6.20	6.60	.123-3	.99-5	.146-3	.11-4	.141-3	.96-5	.124-3	.99-5	.113-3	.11-4	0.667	0.034	6.2
6.60	7.00	.935-4	.60-5	.887-4	.60-5	.829-4	.53-5	.656-4	.50-5	.634-4	.60-5	0.565	0.030	3.6
7.00	7.60	.148-4	.17-5	.176-4	.19-5	.146-4	.15-5	.131-4	.16-5	.140-4	.20-5	0.639	0.050	2.8
7.60	8.20	.117-5	.45-6	.139-5	.51-6	.789-6	.35-6	.109-5	.44-6	.111-5	.53-6	0.630	0.167	0.9
8.20	8.80	.000+0	.00+0	.000+0	.00+0	.000+0	.00+0	.000+0	.00+0	.000+0	.00+0	0.000	0.000	0.0

Differential multiplicity for each target and the value of Alpha with statistical errors only; CHI is the value of the chi-squared for the fit. All values are expressed in exponential notation: .134 + 2 = 13.4.

TABLE IV.7.B ALL + 2.5 < PL < 20.

Y RANGE		BE		AL		CU		SN		PB		ALPHA		CHI
2.60	3.20	.134+0	.13-1	.145+0	.14-1	.166+0	.13-1	.198+0	.15-1	.201+0	.18-1	0.834	0.037	1.0
3.20	3.80	.137+0	.93-2	.195+0	.12-1	.192+0	.10-1	.176+0	.11-1	.201+0	.13-1	0.777	0.026	11.9
3.80	4.20	.848-1	.59-2	.127+0	.76-2	.133+0	.70-2	.129+0	.73-2	.163+0	.96-2	0.855	0.026	10.5
4.20	4.60	.687-1	.41-2	.753-1	.43-2	.840-1	.40-2	.893-1	.45-2	.875-1	.49-2	0.777	0.023	1.1
4.60	5.00	.228-1	.17-2	.317-1	.20-2	.347-1	.18-2	.340-1	.20-2	.344-1	.23-2	0.807	0.028	7.5
5.00	5.40	.632-2	.65-3	.891-2	.75-3	.945-2	.70-3	.102-1	.76-3	.108-1	.91-3	0.842	0.037	2.0
5.40	5.80	.688-3	.13-3	.602-3	.12-3	.853-3	.13-3	.909-3	.15-3	.115-2	.19-3	0.868	0.071	1.9
5.80	6.20	.000+0	.00+0	.000+0	.00+0	.000+0	.00+0	.000+0	.00+0	.000+0	.00+0	0.000	0.000	0.0
						20. < PL < 60.								
2.60	3.20	.000+0	.00+0	.000+0	.00+0	.000+0	.00+0	.000+0	.00+0	.000+0	.00+0	0.000	0.000	0.0
3.20	3.80	.112-2	.44-3	.259-2	.68-3	.375-2	.75-3	.389-2	.97-3	.280-2	.74-3	0.944	0.127	5.0
3.80	4.20	.383-2	.80-3	.703-2	.11-2	.640-2	.92-3	.860-2	.11-2	.988-2	.14-2	0.946	0.069	2.7
4.20	4.60	.795-2	.94-3	.114-1	.12-2	.132-1	.11-2	.136-1	.12-2	.137-1	.14-2	0.856	0.044	2.9
4.60	5.00	.120-1	.84-3	.126-1	.89-3	.138-1	.82-3	.128-1	.84-3	.121-1	.96-3	0.705	0.029	2.7
5.00	5.40	.912-2	.53-3	.101-1	.57-3	.996-2	.51-3	.104-1	.55-3	.967-2	.62-3	0.715	0.024	2.0
5.40	5.80	.505-2	.29-3	.531-2	.31-3	.577-2	.28-3	.534-2	.29-3	.554-2	.35-3	0.718	0.024	2.1
5.80	6.20	.170-2	.12-3	.195-2	.14-3	.217-2	.13-3	.237-2	.14-3	.225-2	.16-3	0.795	0.029	1.6
6.20	6.60	.414-3	.44-4	.622-3	.54-4	.569-3	.45-4	.657-3	.52-4	.644-3	.58-4	0.808	0.038	5.2
6.60	7.00	.157-4	.58-5	.359-4	.89-5	.192-4	.58-5	.422-4	.89-5	.482-4	.11-4	0.974	0.115	5.4
7.00	7.60	.000+0	.00+0	.000+0	.00+0	.000+0	.00+0	.000+0	.00+0	.000+0	.00+0	0.000	0.000	0.0
						60. < PL < 400.								
4.20	4.60	.693-4	.29-4	.114-3	.35-4	.477-4	.21-4	.873-4	.30-4	.000+0	.16+4	0.666	0.198	2.8
4.60	5.00	.185-3	.32-4	.154-3	.31-4	.181-3	.29-4	.180-3	.30-4	.247-3	.41-4	0.767	0.069	2.5
5.00	5.40	.263-3	.31-4	.402-3	.39-4	.438-3	.36-4	.401-3	.37-4	.357-3	.43-4	0.786	0.045	9.4
5.40	5.80	.387-3	.30-4	.489-3	.34-4	.476-3	.30-4	.422-3	.31-4	.356-3	.34-4	0.678	0.032	11.5
5.80	6.20	.393-3	.24-4	.444-3	.26-4	.375-3	.21-4	.331-3	.22-4	.349-3	.26-4	0.625	0.026	7.1
6.20	6.60	.289-3	.16-4	.285-3	.16-4	.276-3	.14-4	.270-3	.15-4	.234-3	.17-4	0.641	0.024	2.1
6.60	7.00	.176-3	.93-5	.185-3	.99-5	.167-3	.83-5	.147-3	.84-5	.136-3	.96-5	0.608	0.023	5.5
7.00	7.60	.618-4	.33-5	.681-4	.36-5	.559-4	.29-5	.543-4	.31-5	.495-4	.35-5	0.613	0.024	6.7
7.60	8.20	.193-4	.18-5	.185-4	.18-5	.121-4	.13-5	.131-4	.15-5	.129-4	.17-5	0.528	0.043	4.5
8.20	8.80	.144-5	.48-6	.324-5	.73-6	.234-5	.55-6	.292-5	.64-6	.195-5	.62-6	0.752	0.120	5.0

Differential multiplicity for each target and the value of Alpha with statistical errors only; CHI is the value of the chi-squared for the fit. All values are expressed in exponential notation: .134 + 2 = 13.4.

TABLE IV.8.A ALL - 2.5 < PL < 20.

ETA RANGE	BE		AL		CU		SN		PB		ALPHA		CHI
2.60 3.20	.633-1	.89-2	.921-1	.11-1	.103+0	.10-1	.861-1	.10-1	.119+0	.14-1	0.845	0.052	4.5
3.20 3.80	.979-1	.82-2	.123+0	.94-2	.150+0	.91-2	.155+0	.99-2	.135+0	.11-1	0.818	0.032	7.7
3.80 4.20	.801-1	.65-2	.103+0	.75-2	.104+0	.67-2	.125+0	.79-2	.111+0	.87-2	0.807	0.031	4.7
4.20 4.60	.562-1	.41-2	.772-1	.51-2	.750-1	.44-2	.831-1	.50-2	.913-1	.62-2	0.823	0.028	3.8
4.60 5.00	.313-1	.24-2	.399-1	.27-2	.450-1	.26-2	.529-1	.30-2	.584-1	.36-2	0.887	0.028	0.4
5.00 5.40	.175-1	.13-2	.213-1	.15-2	.244-1	.15-2	.285-1	.17-2	.256-1	.19-2	0.836	0.029	4.3
5.40 5.80	.859-2	.77-3	.103-1	.87-3	.115-1	.80-3	.106-1	.83-3	.120-1	.10-2	0.782	0.035	2.2
5.80 6.20	.256-2	.35-3	.430-2	.45-3	.441-2	.42-3	.497-2	.46-3	.531-2	.57-3	0.888	0.047	3.4
6.20 6.60	.207-2	.25-3	.205-2	.26-3	.295-2	.28-3	.277-2	.28-3	.253-2	.30-3	0.788	0.048	4.7
6.60 7.00	.106-2	.14-3	.960-3	.14-3	.128-2	.14-3	.123-2	.15-3	.174-2	.19-3	0.843	0.050	4.5
7.00 7.60	.268-3	.42-4	.379-3	.55-4	.575-3	.55-4	.516-3	.55-4	.549-3	.67-4	0.911	0.056	6.1
7.60 8.20	.101-3	.23-4	.117-3	.26-4	.177-3	.28-4	.200-3	.31-4	.258-3	.40-4	1.003	0.080	0.6
8.20 8.80	.257-4	.11-4	.717-4	.20-4	.647-4	.16-4	.102-3	.22-4	.106-3	.25-4	1.056	0.128	2.2
8.80 9.40	.106-4	.75-5	.166-4	.97-5	.328-4	.12-4	.315-4	.12-4	.225-4	.11-4	0.964	0.238	1.6
				20. < PL < 60.									
2.60 3.20	.000+0	.00+0	.000+0	.00+0	.000+0	.00+0	.000+0	.00+0	.000+0	.00+0	0.000	0.000	0.0
3.20 3.80	.427-3	.51-3	.106-2	.43-3	.101-2	.51-3	.264-3	.30-3	.130-2	.58-3	0.810	0.264	2.1
3.80 4.20	.315-2	.67-3	.469-2	.83-3	.466-2	.73-3	.490-2	.81-3	.476-2	.96-3	0.804	0.081	1.2
4.20 4.60	.517-2	.67-3	.733-2	.78-3	.859-2	.76-3	.895-2	.83-3	.891-2	.10-2	0.859	0.047	2.2
4.60 5.00	.786-2	.73-3	.920-2	.76-3	.102-1	.74-3	.105-1	.79-3	.101-1	.94-3	0.780	0.036	1.2
5.00 5.40	.738-2	.49-3	.889-2	.56-3	.865-2	.48-3	.856-2	.53-3	.886-2	.62-3	0.735	0.027	2.6
5.40 5.80	.627-2	.36-3	.632-2	.37-3	.637-2	.33-3	.665-2	.36-3	.616-2	.41-3	0.696	0.024	0.9
5.80 6.20	.332-2	.21-3	.366-2	.23-3	.329-2	.19-3	.366-2	.22-3	.335-2	.25-3	0.697	0.026	3.1
6.20 6.60	.193-2	.13-3	.166-2	.12-3	.185-2	.12-3	.178-2	.12-3	.159-2	.14-3	0.653	0.029	2.8
6.60 7.00	.885-3	.69-4	.868-3	.71-4	.869-3	.63-4	.884-3	.69-4	.792-3	.78-4	0.671	0.034	0.7
7.00 7.60	.321-3	.25-4	.376-3	.28-4	.379-3	.25-4	.343-3	.26-4	.331-3	.30-4	0.698	0.032	4.1
7.60 8.20	.942-4	.12-4	.117-3	.14-4	.113-3	.12-4	.127-3	.13-4	.132-3	.16-4	0.787	0.049	0.7
8.20 8.80	.392-4	.78-5	.408-4	.80-5	.507-4	.79-5	.639-4	.93-5	.866-4	.12-4	0.956	0.070	2.1
8.80 9.40	.169-4	.50-5	.153-4	.48-5	.273-4	.56-5	.247-4	.56-5	.504-4	.89-5	1.058	0.101	4.5

Differential multiplicity for each target and the value of Alpha with statistical errors only; CHI is the value of the chi-squared for the fit. All values are expressed in exponential notation: .134 + 2 = 13.4.

TABLE IV.8.A ALL - 60. < PL < 400. continued

ETA RANGE	BE		AL		CU		SN		PB		ALPHA		CHI
3.80 4.20	.000+0	.00+0	.000+0	.00+0	.000+0	.00+0	.000+0	.00+0	.000+0	.00+0	0.000	0.000	0.0
4.20 4.60	.182-4	.14-4	.460-4	.22-4	.229-4	.14-4	.385-4	.19-4	.355-4	.22-4	0.778	0.260	1.5
4.60 5.00	.253-4	.13-4	.170-4	.12-4	.896-4	.20-4	.645-4	.20-4	.814-4	.26-4	1.043	0.178	5.2
5.00 5.40	.660-4	.16-4	.781-4	.18-4	.104-3	.18-4	.110-3	.21-4	.824-4	.23-4	0.834	0.099	1.8
5.40 5.80	.135-3	.18-4	.168-3	.20-4	.142-3	.17-4	.133-3	.18-4	.101-3	.21-4	0.631	0.059	4.0
5.80 6.20	.137-3	.14-4	.148-3	.15-4	.115-3	.12-4	.114-3	.13-4	.157-3	.18-4	0.679	0.043	7.1
6.20 6.60	.113-3	.11-4	.127-3	.11-4	.115-3	.95-5	.118-3	.10-4	.118-3	.12-4	0.693	0.039	1.0
6.60 7.00	.807-4	.70-5	.716-4	.69-5	.866-4	.66-5	.628-4	.62-5	.606-4	.73-5	0.621	0.039	7.7
7.00 7.60	.388-4	.29-5	.430-4	.32-5	.342-4	.26-5	.291-4	.26-5	.255-4	.31-5	0.557	0.036	6.8
7.60 8.20	.139-4	.16-5	.157-4	.17-5	.120-4	.13-5	.107-4	.14-5	.104-4	.16-5	0.574	0.050	3.0
8.20 9.40	.358-5	.56-6	.267-5	.50-6	.229-5	.42-6	.288-5	.50-6	.326-5	.61-6	0.641	0.068	3.6

TABLE IV.8.B ALL + 2.5 < PL < 20.

2.60 3.20	.111+0	.12-1	.120+0	.13-1	.138+0	.12-1	.167+0	.14-1	.167+0	.16-1	0.840	0.041	1.0
3.20 3.80	.136+0	.99-2	.182+0	.12-1	.179+0	.10-1	.177+0	.11-1	.193+0	.14-1	0.777	0.028	4.8
3.80 4.20	.932-1	.76-2	.134+0	.92-2	.135+0	.84-2	.120+0	.83-2	.155+0	.11-1	0.802	0.030	10.8
4.20 4.60	.647-1	.46-2	.870-1	.57-2	.944-1	.54-2	.923-1	.56-2	.105+0	.70-2	0.824	0.027	4.1
4.60 5.00	.352-1	.27-2	.430-1	.31-2	.492-1	.29-2	.514-1	.32-2	.503-1	.36-2	0.810	0.029	2.3
5.00 5.40	.164-1	.15-2	.207-1	.17-2	.264-1	.17-2	.259-1	.18-2	.256-1	.21-2	0.839	0.035	5.1
5.40 5.80	.735-2	.85-3	.102-1	.95-3	.116-1	.95-3	.126-1	.10-2	.133-1	.12-2	0.867	0.041	1.2
5.80 6.20	.321-2	.43-3	.473-2	.53-3	.526-2	.49-3	.552-2	.52-3	.592-2	.63-3	0.865	0.048	1.6
6.20 6.60	.144-2	.24-3	.226-2	.31-3	.242-2	.27-3	.257-2	.30-3	.326-2	.40-3	0.911	0.058	1.6
6.60 7.00	.641-3	.12-3	.110-2	.16-3	.106-2	.14-3	.135-2	.17-3	.159-2	.20-3	0.934	0.064	1.9
7.00 7.60	.317-3	.52-4	.467-3	.63-4	.596-3	.67-4	.629-3	.7[illegible]-4	.575-3	.76-4	0.885	0.059	3.3
7.60 8.20	.120-3	.28-4	.137-3	.31-4	.155-3	.28-4	.250-3	.39-4	.362-3	.52-4	1.072	0.079	3.9
8.20 9.40	.262-4	.94-5	.406-4	.12-4	.399-4	.10-4	.589-4	.14-4	.895-4	.19-4	1.070	0.116	1.5

Differential multiplicity for each target and the value of Alpha with statistical errors only; CHI is the value of the chi-squared for the fit. All values are expressed in exponential notation: .134 + 2 = 13.4.

TABLE IV.8.B ALL + 20. < PL < 60. continued

ETA RANGE	BE		AL		CU		SN		PB		ALPHA		CHI
3.20 3.80	.113-2	.44-3	.260-2	.68-3	.352-2	.74-3	.380-2	.96-3	.285-2	.74-3	0.940	0.126	4.0
3.80 4.20	.369-2	.79-3	.634-2	.10-2	.585-2	.90-3	.838-2	.11-2	.951-2	.14-2	0.962	0.072	2.2
4.20 4.60	.742-2	.92-3	.108-1	.11-2	.132-1	.11-2	.125-1	.12-2	.126-1	.14-2	0.850	0.046	5.2
4.60 5.00	.106-1	.83-3	.121-1	.93-3	.130-1	.83-3	.125-1	.91-3	.116-1	.10-2	0.731	0.032	2.9
5.00 5.40	.920-2	.56-3	.993-2	.59-3	.964-2	.52-3	.966-2	.56-3	.933-2	.64-3	0.694	0.025	1.0
5.40 5.80	.485-2	.32-3	.517-2	.35-3	.516-2	.30-3	.531-2	.33-3	.582-2	.40-3	0.737	0.027	0.8
5.80 6.20	.230-2	.18-3	.240-2	.19-3	.296-2	.19-3	.265-2	.19-3	.239-2	.21-3	0.730	0.033	7.0
6.20 6.60	.108-2	.10-3	.120-2	.11-3	.126-2	.99-4	.148-2	.11-3	.113-2	.12-3	0.752	0.038	5.7
6.60 7.00	.509-3	.55-4	.637-3	.63-4	.624-3	.55-4	.623-3	.59-4	.597-3	.68-4	0.736	0.043	1.9
7.00 7.60	.152-3	.18-4	.220-3	.22-4	.237-3	.20-4	.259-3	.22-4	.262-3	.26-4	0.852	0.043	2.1
7.60 8.20	.528-4	.93-5	.992-4	.13-4	.675-4	.96-5	.112-3	.13-4	.113-3	.15-4	0.887	0.060	9.5
8.20 8.80	.180-4	.56-5	.343-4	.76-5	.317-4	.66-5	.713-4	.10-4	.695-4	.11-4	1.142	0.092	5.1
8.80 9.40	.513-5	.29-5	.115-4	.44-5	.207-4	.51-5	.336-4	.69-5	.391-4	.82-5	1.323	0.148	0.5
				60. < PL < 400.									
3.80 4.20	.000+0	.00+0	.000+0	.00+0	.000+0	.00+0	.000+0	.00+0	.000+0	.00+0	0.000	0.000	0.0
4.20 4.60	.693-4	.29-4	.114-3	.35-4	.415-4	.20-4	.873-4	.30-4	.000+0	.16+4	0.663	0.199	3.3
4.60 5.00	.187-3	.32-4	.152-3	.30-4	.186-3	.29-4	.176-3	.30-4	.235-3	.40-4	0.751	0.069	2.3
5.00 5.40	.242-3	.30-4	.395-3	.39-4	.416-3	.35-4	.386-3	.37-4	.368-3	.43-4	0.801	0.046	8.8
5.40 5.80	.378-3	.30-4	.464-3	.34-4	.472-3	.30-4	.408-3	.31-4	.313-3	.33-4	0.670	0.034	14.5
5.80 6.20	.391-3	.24-4	.436-3	.26-4	.368-3	.21-4	.326-3	.22-4	.357-3	.27-4	0.630	0.027	6.5
6.20 6.60	.272-3	.16-4	.282-3	.17-4	.262-3	.14-4	.253-3	.15-4	.226-3	.17-4	0.640	0.026	2.2
6.60 7.00	.165-3	.10-4	.171-3	.10-4	.158-3	.89-5	.153-3	.95-5	.130-3	.11-4	0.631	0.027	3.3
7.00 7.60	.755-4	.40-5	.853-4	.43-5	.713-4	.35-5	.646-4	.36-5	.567-4	.40-5	0.599	0.023	11.9
7.60 8.20	.326-4	.23-5	.265-4	.21-5	.231-4	.18-5	.247-4	.20-5	.246-4	.23-5	0.591	0.032	3.4
8.20 8.80	.906-5	.12-5	.114-4	.14-5	.911-5	.11-5	.771-5	.11-5	.940-5	.14-5	0.648	0.057	3.8
8.80 9.40	.242-5	.63-6	.315-5	.73-6	.312-5	.64-6	.344-5	.72-6	.418-5	.91-6	0.839	0.096	0.3

Differential multiplicity for each target and the value of Alpha with statistical errors only; CHI is the value of the chi-squared for the fit. All values are expressed in exponential notation: .134 + 2 = 13.4.

REFERENCES

1. A. Gurtu, et al., Proc. of Vth Int'l. Symp. on Many-Particle Hadrodynamics, pp. 493-512, (Eisenach and Leipzig, GDR, 1974) G. Ranft and J. Ranft, eds.
2. W. Busza, et al., Phys. Rev. Lett. 34, 836 (1975).
3. J. Koplik and A. H. Mueller, Phys. Rev. D12, 3638 (1975) and A. Capella and A. Krzywicki, Phys. Lett. 67B, 84 (1977).
4. K. Gottfried, Phys. Rev. Lett. 32, 957 (1974).
5. S. J. Brodsky, et al., Phys. Rev. Lett. 39, 1120 (1977)
6. G. Berlad, A. Dar, and G. Eilam, Phys. Rev. D13, 161 (1976), and A. Dar, invited talk at Topical Meeting on Multiparticle Production at Very High Energy, ICTP (Trieste, 1976).
7. The data were taken as part of the background studies for an experiment searching for charmed particles at Fermilab (E397). For details see D. Spelbring et al., Phys. Rev. Lett. 40, 605 (1978), and R. Lipton et al., Phys. Rev. Lett. 40, 608 (1978).
8. M. J. Longo et al., University of Michigan Report UM HE74-18 (unpublished).

9. Results from the University of Michigan group (private communication from H. R. Gustafson). We estimate that the γ and K_L^o components of the M-3 beam for 400 GeV incident protons are similar to those for 300 GeV.

10. L. W. Jones et al., Nuc. Inst. and Meth. 118, 431 (1974).

11. J. Cooper, et al., Nuc. Phys. B80, 239 (1974).

12. C. Halliwell, et al., Phys. Rev. Lett. 39, 1499 (1977).

13. H. R. Blieden, et al., Phys. Rev. D11, 14 (1975).

14. R. Schindler, et al., Phys. Rev. Lett. 33, 862 (1974).

15. See, for example, the discussion of factorization in H. Bøggild and T. Ferbel, Annl. Rev. Nuc. Sci. 24, 451 (1974).

16. The main spectrometer is described in D. Spelbring et al, loc. cit.

17. W. Busza, invited paper at VII International Colloquium on Multiparticle Reactions (Tutzing, 1976).

18. D. Garbutt et al., Phys. Lett. 67B, 355 (1977).

19. Private communication from T. Ferbel.

20. J. W. Cronin et al., Phys. Rev. D11, 3105 (1975) and also Ref. 17.

21. W. Busza et al., paper submitted to the XVII International Conference on High Energy Physics (Tbilisi, 1976).

22. The predictions of the coherent tube model are in good agreement with our data (provate communication from A. Dar et al). See also References 3-6.

23. N. N. Nikolaev predictions in S. A. Azimov, et al., paper submitted to the VII International Conference on High Energy Physics and Nuclear Structure (Zurich, 1977).

24. A. Dar, et al., private communication.

APPENDIX

CHECKS OF THE NORMALIZATION

The largest systematic bias in this experiment was the absolute normalization. This bias stemmed from the uncertainty in the amount of material in the beam-line, downstream of our equipment and in front of the University of Michigan's calorimeter, and, in general, from our reliance on that calorimeter. Two independent checks of the neutron flux were available to us, and these indicate that our absolute normalization should be reliable to $\lesssim$15%.

During the period of time we were taking data, we used a beam-monitoring telescope (DM) which consisted of three thin scintillation counters and a 1/2-inch thick piece of lucite, all aligned along the beam. The most upstream counter was about 3-inches square, and situated 6 inches in front of the lucite piece; the second counter was flush with the back of the lucite, measured 1/8-inch thick, and was circular with a diameter of 1 inch; the most downstream counter was a 2-inch square situated about 6 inches downstream of the second one. The first counter was used in anti-coincidence with the second and third counters; the two downstream counters in coincidence provided a measure of the number of neutrons which interacted in the lucite (and in the second counter). This DM telescope was insensitive to three types of events:

1) the kind where a charged particle was produced backwards in the laboratory and vetoed the event by hitting the first counter; 2) the kind which had an all-neutral final state; 3) the kind which had charged particles produced only at large laboratory angles. We estimate that DM was sensitive to 85 ± 10% of the total inelastic cross section.

The second check was performed using the nuclear targets in situ and inserting a 4 inch square scintillation counter (S') ∿9 inches downstream of S (see Fig. II.4). We used as a trigger the logic requirement $\bar{A}\cdot S\cdot S'$ to count most of the neutron interactions in each target (along with those in S). Similar to DM, this telescope was sensitive to ∿85% of the interactions.

These two methods of measuring the neutron flux were used in conjunction with the U.M. calorimeter to check the value of f, the ratio of calorimeter counts to neutrons on target, which was used in calculating our cross sections. The value of f which we used was 0.74 ± 0.08, as calculated in Chapter III.D. Using DM we obtain a value of 0.69 ± 0.11 for f; and using the nuclear-target "inelastic trigger" provides a value of 0.68 ± 0.09. [Note: the lucite absorption length used was 65 cm; the cross sections of the nuclear targets were $46A^{0.69}$mb, as per Ref. 17.] Thus the checks on the value of f are consistent with our calculated value to within experimental error.